

Embedded Micro-Mirrors for Compact Routing of Multimode Polymer Waveguides

Tobias Lamprecht

Graduation Committee:

Chairman and Secretary:

Prof. Dr. Ir. A.J. Mouthaan University of Twente

Promoters:

Prof. Dr. M. Pollnau University of Twente

Prof. em. Dr. A. Driessen University of Twente

Members:

Prof. Dr. sc. techn. D. Erni University of Duisburg-Essen

Prof. Dr. Ir. W.G. van der Wiel University of Twente

Dr. Ir. A.J. Annema University of Twente

Dr. F. Ay University of Twente

Dr. Ir. F. Horst IBM Reaserch GmbH, Zurich

The research described in this thesis was carried out at the Photonics Group, Science and Technology Department, IBM Research GmbH, Zurich Research Laboratory, Säumerstrasse 4, CH-8803 Rüschlikon, Switzerland; and at the Integrated Optical Microsystems (IOMS) Group, Faculty of Electrical Engineering, Mathematics and Computer Science, University of Twente P.O. Box 217, 7500AE Enschede, The Netherlands.

ISBN: 978-90-365-3206-8

Copyright © 2011 by Tobias Lamprecht, Berneck, Switzerland

EMBEDDED MICRO-MIRRORS FOR COMPACT ROUTING OF MULTIMODE POLYMER WAVEGUIDES

DISSERTATION

to obtain
the degree of doctor at the University of Twente,
on the authority of the rector magnificus,
prof. dr. H. Brinksma,
on account of the decision of the graduation committee,
to be publicly defended
on Thursday the 23rd of June 2011 at 12:45

by

Tobias Peter Lamprecht
born on the 14th of November 1976
in Flawil, St. Gallen, Switzerland

This dissertation is approved by:

the promoter: Prof. Dr. M. Pollnau

the promoter: Prof. em. Dr. A. Driessen

Contents

Summary	xi
Kurzfassung	xiii
Samenvatting	xv
1 Introduction	1
1.1 Rationale for optical interconnects	2
1.2 Motivation and problem statement	6
1.3 Aim and structure of this thesis	7
2 Optical interconnects	9
2.1 Introduction to optical interconnects	10
2.2 State of the art optical interconnects	10
2.3 Deployed polymer waveguide technology	11
2.3.1 Substrate material	12
2.3.2 Polymer material	12
2.3.3 Polymer deposition	13
2.3.4 Waveguide core patterning	14
3 Theory of multimode optical waveguides	15
3.1 Introduction	16
3.2 Dielectric slab waveguides	16
3.3 Rectangular dielectric waveguides	22
3.4 Weakly-guided step-index fiber	26
4 Micrometer-accurate passive-alignment of components in PCBs	31
4.1 Introduction	32
4.2 Combining optical waveguides and mechanical alignment structures on PCBs	32
4.2.1 Optical PCB fabrication procedure	32
4.2.2 Passive alignment adapters	34
4.2.3 Passive alignment accuracy	34
4.3 Measurements	35
4.3.1 Measurement system	35
4.3.2 Position accuracy of the copper markers	36
4.3.3 Mechanical alignment slot size	36
4.3.4 Alignment accuracy of silicon adapters to the alignment slots	37
4.3.5 Alignment accuracy between an optical module and waveguides	37
4.4 Conclusions	38
4.4.1 Outlook and continuing work	38
5 Concept of embedded micro-mirrors	41
5.1 Introduction	42

Contents

5.2	State-of-the-art mirrors	42
5.2.1	Discretely fabricated optical routing elements	42
5.2.2	Optical routing elements fabricated by subtractive process	43
5.2.3	Waveguide endfacet as routing element	44
5.3	Requirements for mirrors in polymer waveguide applications	44
5.4	Embedded micro-mirrors	45
5.5	Design	45
5.5.1	Layout density considerations	47
5.6	Reflectivity of metal layers	48
5.7	Summary	48
6	Reflective metal layer by selective chemical plating	49
6.1	Introduction	50
6.2	Approach	50
6.3	Process Description	51
6.3.1	Polymer cladding material	52
6.3.2	Photosensitive acryl-monomer resin	52
6.3.3	Selective surface functionalization by aminolysis	53
6.3.4	Selective catalyst deposition	54
6.3.5	Electroless nickel deposition	55
6.3.6	Immersion gold process	56
6.4	Characterization	57
6.4.1	Benchmark mirrors as characterization specimen	57
6.4.2	Optical characerization equipment	57
6.4.3	Benchmark mirror measurements	58
6.5	Summary	59
7	Fabrication and characterization of embedded micro-mirrors	63
7.1	Fabrication of the optical layer stack	64
7.1.1	Substrate	64
7.1.2	Lower cladding	64
7.1.3	Acrylic monomer based micro-structures	65
7.1.4	Selective deposition of reflective layer	70
7.1.5	Waveguide fabrication	72
7.1.6	Upper cladding	74
7.2	Fabrication process for the characterization samples	74
7.3	Fabrication process for the reference samples	74
7.4	Realized micro-mirrors	75
7.4.1	Embedded in-plane micro-mirrors	75
7.4.2	Embedded out-of-plane micro-mirrors	77
7.5	Mirror reflectivity	79
7.5.1	Micro-mirror reflectivity	79
7.6	Micro-Mirror insertion loss	81
7.6.1	Characterization method	81
7.6.2	Results	81
7.7	Micro-mirrors in an electro-optical flex board	83
7.7.1	Design	84
7.7.2	Fabrication	89
7.7.3	Experimental results	89
7.8	Summary	89

8 Experiments on modal power coupling in waveguides	93
8.1 Introduction	94
8.2 Model for mode propagation in waveguides	95
8.2.1 Amplitude coupling	95
8.2.2 Power coupling	95
8.2.3 Origin of modal power coupling	96
8.2.4 Mode designation in waveguides	97
8.3 Generic optical link	98
8.4 Experimental approach	100
8.4.1 Method to determine the modal power coupling matrix \mathbf{K}	100
8.4.2 Selective mode launch	101
8.4.3 Mode analysis approach	101
8.4.4 Optical setup	104
8.5 Experimental results	106
8.5.1 Selective mode launch in a step-index fiber	106
8.5.2 Variable mode launch in a polymer waveguide	106
8.5.3 Limitations of the experimental setup	109
8.6 Potential applications	110
8.6.1 Loss prediction of an optical link	110
8.6.2 Signal-level dependent propagation losses	110
8.7 Summary	111
9 Conclusions and outlook	113
Bibliography	119

Summary

Summary

Performance scaling of computing devices leads to higher bandwidth requirements for the processor package. The limited scalability of high-speed electrical interconnects [79] drives research on optical interconnects and optical printed circuit board (PCB) technologies [2, 14, 22, 52, 80].

The **first part** of this thesis is concerned with simplifying polymer waveguide routing and compact integration schemes for optical printed circuit boards. The discussed subjects are: Embedded micro-mirrors for in-plane and out-of-plane redirection of the light path (a), and mechanical alignment fiducials for the assembly of optical components (b). Both are then eventually integrated in a compact electro-optical flex board (c).

The developed embedded micro-mirrors (a) are an integral part of the waveguide layer. The micro-structures that make up their bodies are fabricated directly onto the lower cladding by UV-laser patterning of a photosensitive resin. Vertical and 45° tilted micro-structures are eventually used as in-plane and out-of-plane micro-mirrors, respectively. A wet-chemical deposition process is developed to apply the reflective metal layer selectively on the micro-structures. In-plane micro-mirrors with a surface roughness of $R_a = 20$ nm and reflectivity of $R = 0.5$ are realized. The fabrication processes are compatible to polymer waveguide and PCB manufacturing equipment.

The presented mechanical fiducial marker approach (b) enables a precise and adjustment-free mounting of external components to an optical printed circuit board. The achieved positioning accuracy of inserted mechanical adapters is $\sigma_{axis} < 5$ μ m with respect to the waveguide axis. This yields an acceptable misalignment induced coupling loss of less than 0.5 dB.

An electro-optical flex board (c), which integrates the mechanical fiducial markers (b) and the out-of-plane micro-mirrors (a), is fabricated as basis for a compact electro-optical module. The optoelectronic element, which can be a VCSEL- (vertical cavity surface emitting laser) or PD- (photodiode) array, will be vertically coupled to the underlying array of twelve polymer waveguides by the embedded out-of-plane micro-mirrors.

The **second part** of this work is concerned with the analysis of light propagation in waveguide links. Herein proposed is an experimental approach to characterize the modal power coupling in simple waveguide elements. The used modal power coupling matrix relates the input and output modal power distribution of the waveguide elements. A generic optical waveguide link can then be represented as a concatenation of pre-characterized simple waveguide elements.

To measure the modal power coupling matrix, the launch of specific modes at the input facet is required. Therefore, an intensity- and a phase- controlling spatial light modulator (SLM), are used to generate the specific modal field profiles. Therewith, lower order modes are successfully launched in a circular step-index fiber. In order to analyze the modal power distribution at the endfacet of the waveguide, an approach based on optical Fourier transformation is tested herein. Experiments with a variable mode launch qualitatively demonstrate the correlation between the order of the excited modes and the detected intensity distribution in the k -space after the optical Fourier transformation.

Kurzfassung

Die Leistungssteigerung von Rechnern erhöht die Anforderung an die Datenbandbreite zum Prozessor. Die physikalisch limitierte Skalierung von elektrischen hochfrequenz Verbindungen [79], fördert die Forschung im Bereich der optischen Verbindungstechnik und optischen Leiterplatten [2, 14, 22, 52, 80].

Der **erste Teil** dieser Arbeit befasst sich mit Mikrospiegeln in Polymerwellenleitern und mit kompakten Integrationsverfahren für optische Leiterplatten. Dabei werden (a) eingebettete Mikrospiegel für die Lichtumlenkung innerhalb und vertikal zur Ebene, (b) sowie mechanische Alinierstrukturen für das präzise Einbauen von optischen Elementen entwickelt. (c) Anschliessend werden diese beiden Funktionsbausteine in einem flexiblen optischen Substrat vereint. Die entwickelten Mikrospiegel (a) sind als integraler Bestandteil der optischen Polymerwellenleiter ausgelegt. Die Mikrostrukturen werden direkt auf der unteren optischen Mantelschicht durch Laserstrukturieren eines photosensitiven Polymers erzeugt. Die vertikalen und die um 45° geneigten Mikrostrukturen dienen der Lichtumlenkung innerhalb, beziehungsweise vertikal zur Wellenleiterebene. Ein chemisches Auftragsverfahren ist entwickelt worden um die reflektierende Metallschicht selektiv auf die Mikrostrukturen aufzutragen. Die resultierenden Mikrospiegel für die Lichtumlenkung innerhalb der Ebene weisen eine Oberflächenrauheit von $R_a = 20$ nm, sowie ein Reflexionsvermögen von $R = 0.5$ auf. Die benötigten Prozesse sind kompatibel zur Fabrikation von optischen Leiterplatten.

Die realisierten mechanischen Alinierstrukturen (b) erlauben ein präzises und justagefreies Montieren von Komponenten auf eine optische Leiterplatte. Es konnte eine Positionsgenauigkeit von $\sigma_{axis} < 5$ μm für das Einsetzen von Adaptern gezeigt werden. Die aus dieser Positionstoleranz resultierenden zusätzlichen optischen Kopplungsverluste belaufen sich auf weniger als 0.5 dB.

Die flexible optische Leiterplatte (c) dient als Basis für ein elektro-optisches Modul. Diese vereint dabei die mechanischen Alinierstrukturen (a) und die Mikrospiegel (b). Im Modul wird dabei das optoelektronische Element - ein vertikal abstrahlender Laserarray (VCSEL: vertical cavity emitting laser) oder ein Photodiodenarray – mittels eines um 45° geneigten Mikrospiegels vertikal zu den darunterliegenden zwölf Polymerwellenleitern gekoppelt.

Der **zweite Teil** dieser Arbeit betrachtet die Analyse der Lichtpropagation in den auf Polymerwellenleiter basierten optischen Verbindungen. Ein experimenteller Ansatz zur Charakterisierung der modalen Leistungskopplung in Wellenleiterstrukturen ist dafür entwickelt worden. Die dabei verwendete modale Leistungskopplungs-Matrize beschreibt die Beziehung zwischen der modalen Leistungsverteilung am Eingang und Ausgang des Wellenleiters. Ein optischer Link kann anschliessend durch aneinandergesetzte Wellenleiterelemente beschrieben werden. Die Messung der modalen Leistungskopplungs-Matrize erfordert das Erzeugen von spezifischen Moden am Eingang des Wellenleiters. Das gewünschte Modenfeld wird dabei mittels zweier räumlicher Lichtmodulatoren (SLM: spatial light modulator) - je einer für die Intensität und einer für die Phase - erzeugt. Mit dem entsprechenden optischen Aufbau sind optische Moden tiefer Ordnung in zirkularen Stufenindex-Fasern erzeugt worden. Ein Ansatz welcher auf der optischen Fouriertransformation beruht ist zur Analyse der Leistungsverteilung in den Moden am Wellenleiterausgang untersucht worden. Experimente, welche auf variablen Modenfelder am Wellenleitereingang basieren, zeigen die Korrelation zwischen der Ordnung der angeregten Moden und der gemessenen Intensitätsverteilung im k-Raum nach der optischen Fouriertransformation.

Samenvatting

De toename van de prestaties van computercomponenten leidt tot een hogere vereiste bandbreedte voor de processor module. De beperkte schaalbaarheid van hoge-snelheid elektrische verbindingen [79] versterkt het onderzoek naar optische verbindingen en optische printplaat technologieën [2, 14, 22, 52, 80].

Het **eerste deel** van dit proefschrift betreft het vereenvoudigen van de layout van polymeer golfgeleiders en compacte integratiemethoden for optische printplaten. De behandelde onderwerpen zijn: Ingebedde microspiegels voor het in-het-vlak en uit-het-vlak afbuigen van het licht (a) en mechanische uitrichtstructuren voor de assemblage van optische componenten (b). Deze methoden worden daarna samen toegepast in een compacte flexibele elektro-optische printplaat (c).

De ontwikkelde microspiegels (a) zijn een integraal onderdeel van de golfgeleiderlaag. De microstructuren die hun basis vormen worden direkt op de ondercladding gefabriceerd door het structureren van een lichtgevoelige hars met een UV-laser. Vertikale en 45° gekantelde microstructuren worden uiteindelijk gebruikt voor respectievelijk in-het-vlak en uit-het-vlak spiegel-tjes. Een nat-chemisch proces is ontwikkeld om de spiegelende metaallagen selectief op de microstructuren aan te brengen. In-het-vlak microspiegels met een oppervlakte ruwheid van $R_a = 20$ nm en reflectiviteit van $R = 0.5$ zijn gemaakt. Het productieproces is compatibel met polymeergolfgeleider- en printplaat-productieapparatuur.

De gepresenteerde benadering voor mechanische uitlijnstructuren laat een preciese montage zonder fijn-positionering toe van externe componenten in een optische printplaat. De bereikte precisie van geplaatste mechanische adapters is $\sigma_{axis} < 5 \mu\text{m}$ relatief tot de as van de golfgeleider. Dit resulteert in een acceptabel verlies door uitlijnfouten van minder dan 0.5 dB.

Een flexibele elektro-optische printplaat (c), welke de mechanische uitlijnstructuren (b) en de uit-het-vlak microspiegels (a) combineert, werd gefabriceert als basis voor een compacte electro-optische module. Het optoelectronische element, dat een VCSEL- (vertical cavity surface emitting laser) of PD- (photodiode) array kan zijn, wordt vertikaal gekoppeld aan het onderliggende array van twaalf polymeer golfgeleiders door de ingebedde uit-het-vlak microspiegels.

Het **tweede deel** van dit proefschrift betreft de analyse van lichtgeleiding in golfgeleiderverbindingen. Hier wordt een experimentele aanpak voorgesteld om de modale vermogenskoppeling in eenvoudige golfgeleider-elementen te bepalen. De gebruikte vermogenskoppelmatrix relateert de modale ingangs- en uitgangsvermogensverdeling van de golfgeleider-elementen aan elkaar. Een algemene optische golfgeleiderverbinding kan dan gezien worden als een aaneenschakeling van, vooraf doorgemeten, eenvoudige golfgeleider-elementen.

Om de modale vermogenskoppelmatrix te meten is het vereist dat een specifieke mode aan het ingangsvlak gelanceerd kan worden. Een intensiteits- en een fasemodulerende "spatial light modulator" (SLM) worden gebruikt om de specifieke modale veldverdelingen te genereren. Hiermee werden lagere orde modes met succes gelanceerd in een ronde "step-index" glasvezel. Om de modale vermogensverdeling aan de uitgang van de golfgeleider te meten wordt hier een aanpak gebaseerd op een optische Fouriertransformatie getest. Experimenten met een variable modelancering demonstreren kwalitatief de correlatie tussen de orde van de aangeslagen modes en de gemeten intensiteitsverdeling in k-ruimte na de optische Fouriertransformatie.

1 Introduction

This thesis is concerned with the routing and propagation of light in multimode polymer waveguides used in optical interconnect applications. This introductory chapter discusses the motivation to perform research on optical interconnects. And in particular, the need for compact optical routing schemes is elaborated. The aim and structure of this thesis are explained in the last section of this chapter.

1.1 Rationale for optical interconnects

For decades, a steady performance growth of computer systems has been in progress. This trend is apparent for all kind of computing systems, ranging from video game consoles over personal computers to large supercomputers. The performance development of the latter is available online on [103], semi annually provided by the TOP500 organization, see Figure 1.1. Currently, a performance increase by a factor of one thousand every eleven years takes place in the supercomputer regime. This reflects the performance increase, caused by the continuing denser integration predicted by MOORE [83], more than 40 years ago.

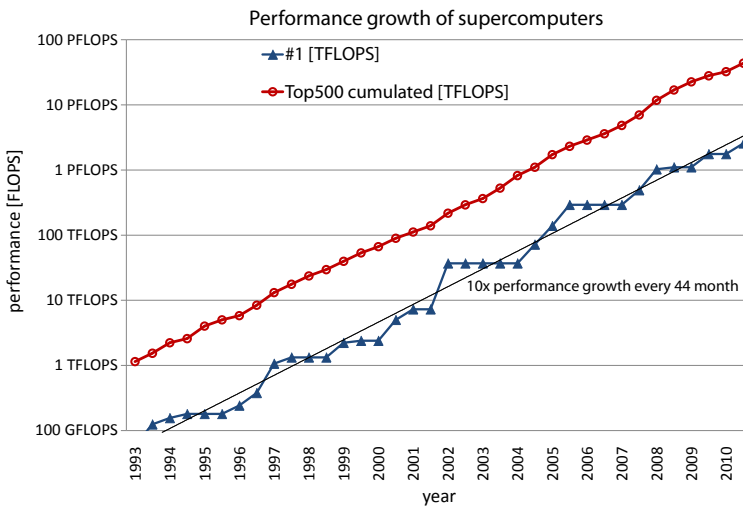


Figure 1.1: Supercomputer performance development over the last decades from TOP500 [103] in FLOPS (floating point operations per second).

Paradigm change from scaling to system integration

In the past, simple down-scaling of the feature size on a microprocessor led to the desired increase in computing power. In recent years, major scaling challenges occurred. Firstly, simple down-scaling does not lead to a performance increase of the chip anymore [10]. Higher capacitance, higher resistance, and reduced stress in the transistor lead to a relative performance loss after down-scaling. Additional performance-enhancing elements, such as channel scaling, gate height reduction, and advanced dielectric materials, are required to end up with a net performance increase for the chip [10]. Secondly, the clock frequencies are stagnating at around 3 GHz due to the transistor interconnection bottleneck [110].

To further maintain the system-performance growth-rate, additional measures have to be applied. Advanced system integration plays an important role nowadays. This can be seen as a paradigm shift from pure down-scaling to a more general

system integration approach. In particular a savvy and dense integration of microprocessors and memory chips on the processor package level are very effective. This leads to high-performance multi-chip modules (MCM) used in current high-performance computing systems (HPCS). This progressing system-integration on the processor package level leads to higher bandwidth requirements for the data flow to and from the processor package.

Limitations of electrical interconnects

Electrical signaling on printed circuit boards (PCBs) is limited by high-frequency propagation loss, inter-channel crosstalk, and bandwidth limitations, which eventually limit the scalability of electrical interconnects. MILLER approximated the limitations of an electrical link in [79] as follows,

$$B \sim B_0 \cdot A/l^2 \quad (1.1)$$

with B being the bandwidth [b/s], B_0 a link-type specific bandwidth constant, A the cross-sectional dimension [m²] and l representing the link length [m]. This limitation is scale-invariant due to the ratio of cross-sectional dimension and squared link-length. High performance strip-lines in a PCB show a bandwidth constant $B_0 \approx 10^{15}$ b/s [79]. From these aspects we can conclude, that the aggregate bandwidth per cross-section area is limited, which eventually leads to a bottleneck in the data transfer. Three properties are mainly responsible for the limitation of the bandwidth constant. a) Electrical lines are critical to shield and neighboring channels are susceptible to crosstalk . b) It requires precisely manufactured transmission lines to provide good impedance match. Narrow line pitches required to cope with the desired bandwidth density require very narrow fabrication tolerances of a few microns. c) Standard PCB materials exhibit, in particular in the high-frequency signal regime, high propagation loss values. This is mainly due to the water absorbed in the matrix material, e.g., epoxy. Recently commercialized novel materials such as liquid crystal polymer (LCP) from ROGERS achieve excellent values. Unfortunately, the processing is very difficult restricting the material from being widely used. Electronically equalized transmission lines are one measure to overcome this limitation. However, signal treatment efforts, additional chip area and possible latency issues are potential drawbacks.

Power limitations

Let us take a closer look at the expected properties of the next chip generations as stated by the INTERNATIONAL TECHNOLOGY ROADMAP FOR SEMICONDUCTORS (ITRS) in [45]. As has been the case for decades, the computing performance, the number of signal channels, the signal frequency and other chip properties are expected to increase. More of a concern is the observation that the total power dissipation per chip nowadays reaches 200 W and is expected to remain at this value. Furthermore, transistor scaling leads to an increase in the dissipated passive power, mainly caused by the increasing gate leakage in the off-state of a transistor [9]. De-

spite the increasing computing power and thus increasing aggregate bandwidth, the total available power for interconnects remains rather constant. A power-efficient, high data-throughput optical interconnect system, based on a silicon-carrier approach, is presented in [95]. This state-of-the-art system demonstrates a power consumption of 5 mW/Gbps at a bandwidth of 10 Gb/s per channel. Predictions expect that this power consumption, which is equal to 5 pJ/b , will need to undergo a thirty-fold reduction towards 170 fJ/b by 2022 [81].

Density limitations

Another finding from the ITRS roadmap [45] is that the chip area will remain constant and therefore limit the available space per I/O-pin (input/output). However, several chips might be assembled together on one package to form a MCM. This leads to the sheer amount of tens of thousands of high-speed interconnects routed on or off the package. Most likely, these packages will use liquid cooling interfacing to the backside of the chips on the package to remove the dissipated power. Thus, only very limited space on the package, e.g., the bottom side and the circumference of the package, can be used to handle the interconnect channels. Therefore, we can conclude that interconnects with a very high bandwidth density are indispensable.

Fundamental advantages of optical interconnects

We can summarize that the bandwidth density and power limitations are major limitations for interconnects in order to provide the expected aggregate bandwidth for future data processing systems. An alternative to electron based signals is optical communication. Optical waveguides feature small cross-sectional dimensions, ranging from $50 \mu\text{m}$ down to $9 \mu\text{m}$, for multimode and single-mode applications, respectively. Hence, small pitches between waveguide cores are yielded, which enables a high channel-count per cross-sectional area, see Figures 1.2 and 1.3. Furthermore optical signals can be transmitted at a very high bandwidth, e.g., 40 Gb/s over relatively long distances. A metric therefore is the so called bandwidth \times length product.

A high channel-count per cross-sectional area in combination with a high bandwidth per channel leads to a high bandwidth per cross-section efficiency. Thus, a higher aggregate bandwidth per given cross-sectional area is provided. By exploiting the channel density using two dimensional arrays of channels, optics outperforms electrical interconnects already nowadays by one order of magnitude, see Figure 1.2. Electrical interconnects are mainly limited by the required cross-section to meet the impedance requirements and ensure appropriate shielding of the channel, see Figures 1.2 and 1.3.

New paradigms can be explored such as tapping the I/O signals directly from the top-side of the carrier and leading them in a flexible sheet towards the destination, e.g., the card edge or another chip-module [3]. The signal density is much higher on the top-side of the carrier than on the bottom-side. The former directly connects to the processor chip with a very narrow solder ball pitch of $200 \mu\text{m}$ and below. In contrast, the latter contacts to the PCB through a BGA (ball grid array) connector

1.1 Rationale for optical interconnects

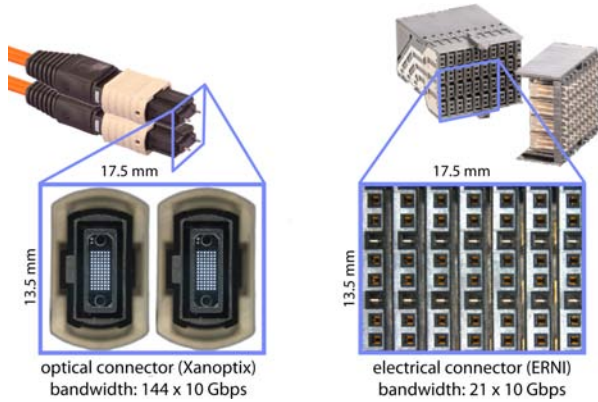


Figure 1.2: Channel density comparison (both detail views at same scale) between electrical connector (*left*) and multimode optical connector (*right*).

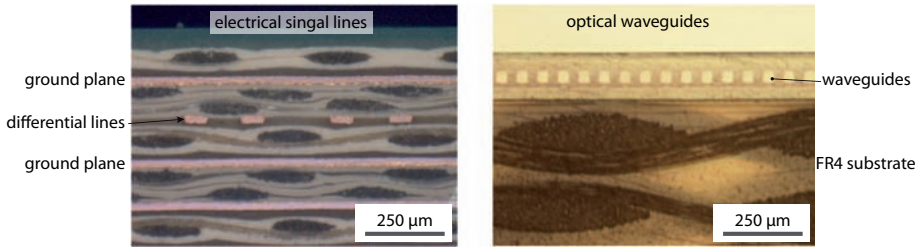


Figure 1.3: Channel density comparison (both images at same scale) between electrical embedded-coplanar lines (*left*) and multimode optical polymer waveguides (*right*) on PCB substrates.

with a pitch in the range of 0.8 to 1 mm, which is a factor 25 lower areal-density [3]. Thus, the signals can be collected directly with high-density, on the top-side of the chip. This can reduce the amount of signal channels passing the BGA connector, which is a major bottleneck. Therefore, the aggregate off-package bandwidth can be increased by adding high-speed optical channels to the signal channels of the BGA connector. This is in particular of interest because half of the BGA connector pins are already used for power and ground [45].

Optical signal transmission has the potential to be more power-efficient than the electron based transmission. At what point optics exceeds the efficiency of electrical signal depends on: (i) power requirements, (ii) bandwidth, (iii) transmission distance, and (iv) density. There are already cases where optical interconnects are certainly in favor. For the future, and therefore for increasing signal frequencies, the advantages shift more towards optics. This, also because optical losses are independent of the signal frequency. In contrast, the losses of the electrical signals strongly depend on their frequency. First, the material specific energy dissipation (loss tangent) rises with increased frequency, and second, the skin effect leads to increased losses for

higher frequencies.

The advantage that the transmission lines of optical interconnects are insensitive to increases in the signal frequency is based on the fact that the carrier frequency of light (10^{15} Hz) is by orders of magnitude higher than the electrical signal frequency (10^{10} Hz). Once, faster optoelectronic senders and receivers are available, they can be simply implemented into the existing waveguide technology.

The different physical behavior of photons, compared to electrons, provides another crucial advantage. The signals are unsusceptible to electromagnetic interference (EMI). This eliminates space-consuming signal shielding, as is necessary for electrical signals.

All of these factors are drivers for the ongoing research on optical printed circuit board (PCB) technologies for intra-system interconnects. Major challenges for commercial success of optical interconnects are reliability and efficient fabrication processes as well as ease of integration of optical elements and the connection to the electronic domain. Eventually, the optical approach should provide a clear performance-to-cost advantage over electrical solutions to overcome the entry barrier for fundamentally new technologies in computing systems.

1.2 Motivation and problem statement

Taking in consideration the computing performance forecast, the high-performance computing-system roadmap, the aforementioned bottlenecks, and the above quoted performance advantages of optics, one can conclude that optical interconnects will find their way, in one form or another, into future computing systems. Research and development groups around the globe [4, 5, 8, 12, 13, 26, 32, 36, 52, 53, 56, 58, 73, 81, 82, 84, 85, 87, 92, 95, 105, 106, 108, 112, 116] have deployed various essential methods and processes to fabricate optical interconnects. However, there are still several major hurdles to overcome the gap from research to commercialization. Among them are (a) advanced routing capabilities for polymer optical waveguide interconnects, and (b) the detailed understanding of the optical behavior of multimode waveguide based optical interconnects. These two subjects are the main topics of the work presented herein.

Regarding the first subject (a): Nowadays, the most promising optical interconnect approaches rely on layer based waveguide fabrication methods. This yields in-plane routed waveguides, which consist of straights, bends and crossings. Although multi-layer waveguide stacks have already been demonstrated [14, 51], interlayer routing of the optical path is not yet state of the art. Efforts are made by several groups towards an optical via as vertical coupling element and vertical layer connection [34], equivalent to the indispensable electrical via in PCBs. Eventually, this will yield more advanced waveguide routing capabilities and thus enhance the performance and versatility of optical interconnect approaches.

With regard to the second subject (b): Experience shows that the accurate pre-

diction of the insertion loss in an optical interconnect system is error-prone. The insertion loss of a waveguide generally depends on the actual mode launch condition in the waveguide, which is related to the angular and lateral light distribution at the input facet of the waveguide. While the propagation of optical modes is well-understood for graded-index optical fibers, it is still a research topic for highly multimodal step-index waveguides [69]. Various parameters increase the complexity of such an optical link. Among them are the high number of optical modes, the fabrication induced roughness of the core-cladding boundary, deviations from the ideal rectangular cross-section geometry, curved waveguides, and the alignment tolerances of optical connections. Until now, large margins are usually included in the designing of optical multimode waveguide links. Understanding and mastering the optical behavior of multimode waveguides will be crucial to pushing the envelope of optical interconnect systems and for a successful commercialization of the technology.

1.3 Aim and structure of this thesis

The aim of this thesis is to advance the functionality of optical polymer waveguides for data transmission in optical interconnect systems. Main aspects are: optical connectors for polymer waveguides in printed circuit boards (Chapter 4), advanced waveguide routing capabilities and vertical light coupling (Chapter 5 - 7), and improved understanding of multimode propagation in optical multimode links (Chapter 8).

Chapter 2 provides an introduction to the field of optical interconnects and summarizes state-of-the-art optical interconnect approaches. Furthermore, the polymer waveguide technology deployed by our research group, which is the base technology for this work, is explained in detail.

Chapter 3 exploits methods to calculate the characteristic electromagnetic field distributions, known as optical modes, in different kind of multimodal dielectric waveguides. An analytical solution is examined for a simple dielectric slab waveguide. Within this work, planar waveguides with a rectangular-like cross-section are of particular interest. An analytical and a numerical approach to obtain the modes for this kind of waveguides are described.

Chapter 4 explains the deployed assembly technique for micrometer-accurate integration of individual parts into optical printed circuit boards. The goal is to utilize passive-alignment to eventually simplify the alignment critical assembly of mechanical or opto-mechanical elements. An adapter, which provides an MT-standard compliant opto-mechanical interface, is passively inserted into an optical printed circuit board.

Chapter 5 introduces the concept of micro-mirrors embedded in the polymer waveguide layer. Light can be redirected by these mirrors within the waveguide plane - in-plane - and vertical to the waveguide plane - out-off-plane - by means

of such micro-mirrors. Light reflection is achieved by depositing a gold layer onto the respective micro-structures. The goal is to provide embedded micro-mirrors as an advanced functionality of our polymer waveguide technology. These can be in-plane corners, vertical inter-layer connection (optical via), and vertical light coupling to external optical elements.

Chapter 6 deals with the selective wet-chemical metal deposition process developed in order to deposit a reflective metal-layer on polymer micro-structures to realize the aforementioned micro-mirrors. A customized photosensitive acrylic monomer blend serves as base material for the micro-structure. The surface of this acrylic structure can then be selectively activated by a chemical process. Thereon deposited is an autocatalytic electroless nickel-phosphor layer. A final electroless immersion gold layer is applied to increase the optical reflectivity in the near infrared spectral range. The acrylic material and the processes are developed on large-size planar substrates, the benchmark mirrors.

Chapter 7 focuses on the fabrication of the previously introduced micro-mirrors embedded in polymer waveguides. UV-laser direct-writing is used to fabricate the vertical (in-plane) and tilted (out-of-plane) micro-structures by photoinduced curing of the aforementioned acrylic resin. The thereon deposited metal layer, applied according to the process developed in the previous chapter, yields the reflective layer of the micro-mirrors. Waveguide core and top cladding are completing the optical layer stack with embedded micro-mirrors. The reflectivity is characterized for bare micro-mirrors, while the insertion loss is investigated for optical waveguides with embedded micro-mirrors. Finally, an electro-optical flex-board is fabricated which serves as basis for a compact high-bandwidth parallel optical module. This waveguide flex-board explores the applicability of the various technologies demonstrated in Chapters 4 to 7.

Chapter 8 is concerned with an experimental method to investigate the light propagation in a multimode waveguide by means of a modal power coupling matrix approach. This matrix describes the relation between the input and output modal power distributions of the waveguide. The selective mode launch at the input facet of a circular waveguide is realized with spatial light modulators as means of controlling the input modal power distribution. Besides the intensity measurements at the output facet to identify individual modes, also an optical Fourier-transformation approach is tested to analyze the modal power distribution at the output facet of the waveguide.

2 Optical interconnects

The first two sections in this chapter provide an introduction to the field of optical interconnects and the main applications related to computing systems. They describe the state-of-the-art approaches and current research topics within optical interconnects. The final section describes the waveguide technology developed and successfully deployed by our research group. The focus is on the polymer waveguide fabrication processes, which will be used in the following chapters as baseline technology.

2.1 Introduction to optical interconnects

Figure 2.1 shows the historic trend of optical communication. First, optics has been applied for intercontinental optical backbones as an ultra-long distance application, employing few fiber channels. Efficient Er-doped (erbium) optical amplifiers and laser sources in the optical C-band were the key to the success for this application.

The trend, which was boosted by the increased demand for data communication, goes towards hundreds of cost-efficient optical waveguides and sources, implemented in metropolitan-, wide-, and local-area networks (WAN, MAN, LAN). Exemplary is the optical data communication required to interconnect an enterprise data center. There, the cost-efficient multimode fiber technology replaced the expensive singlemode solution for shorter distances below 300 m.

Following the trend, numbers of lines are increased towards shorter link distances. The realm of polymer waveguide based optical interconnects is mainly the intra-rack and on-board optical communication. Hundreds or even thousands of optical channels, most likely multimode fibers or optical polymer waveguides, are used to cope with the bandwidth and power requirements.

Research in exploratory photonics is progressing towards on-package or even on-chip optical data transfer. The waveguide technologies of interest therefore are ranging from polymer waveguides over integrated silicon-oxynitride (SiON) to highly integrated silicon photonics.

2.2 State of the art optical interconnects

As previously examined in Section 1.1, the roadmaps exhibit the demand for a power efficient and a bandwidth per cross-section efficient off-chip communication. Due to the intrinsic advantages of photonic based signal transmission, optical communication is a viable solution to overcome expected data bottlenecks.








Type	Internet wide area network	Local area network	Rack-to-rack	Card-to-card	On-card	On-MCM	On-chip
Illustration							
Distance	>> 1km	< 2km	< 30m	< 1m	< 0.3m	< 100mm	< 10mm
Channel count	1	1-10	<100	100-1'000	~1'000	~10'000	~100'000
Status of optics	mature	mature	deployed	early adopters	development	research	exploratory
Time line	1980		2010		future		

Figure 2.1: Historical development of optical communication.

Polymer material

Indispensable for the success of polymer waveguide based optical interconnect applications is the availability of a low-loss optical polymer material, which surpasses the demanding reliability requirements. In addition, ease of manufacturing shall enable future cost-efficient production lines. Various specialty chemical companies, among them DOW CHEMICAL [1], WACKER, ASAHI GLASS, and EXXELIS; as well as research institutes, such as the FRAUNHOFER-GESELLSCHAFT, are developing materials for optical waveguides. Extensive essays regarding the material classes currently under investigation are provided by ELDADA [25] and others [73, 107].

Waveguide fabrication

Various methods to structure the waveguide core are in use. Besides the widely spread photolithographic UV-exposure, also UV-laser direct writing [15], molding [11, 92], photobleaching [104], two-photon-absorption [66, 86], ion-diffusion [68], and laser-ablation [109, 35] are commonly used. The core fabrication methods are related to the material and the application. A major challenge for the structuring methods is the maximum substrate size which can be processed therewith. In order to be compatible with existing PCB manufacturing and, thus, to be cost-efficient, the intended optical interconnect applications depend on large-area substrate fabrication tools. One method which can handle large substrates is vector-based UV-laser direct writing [15].

Transmitter and receiver

The requested high data rates and the targeted cost-efficiency of optical interconnects can be satisfied by using VCSEL- (vertical cavity surface emitting laser) and PD- (photodiode) arrays which provide 10 Gb/s data rates and beyond. The VCSELs are used in current-driven, non-return-to-zero (NRZ) intensity-modulation regime. Thereby, the off-current I_{off} is kept above the lasing threshold. In this regime, VCSEL in general provide the shortest time constants and thus the highest dynamics. Turning on a VCSEL from below the laser threshold leads to a significant turn-on delay [91, 112].

The distribution of emitted light is multimodal and changes with the current in the laser cavity. Therefore, while the signal rises from the low level to the high level, the modal light distribution coupled into the waveguide changes considerably [112]. Since the propagation losses in the waveguide might depend on the modal intensity distribution, a power depending loss may occur. This mode dependent loss is considered in Chapter 8.

2.3 Deployed polymer waveguide technology

The herein described polymer waveguide technology has been developed over the past years by our research group, partially in collaboration with internal and external partners [1, 15, 16]. The work presented in the following chapters is based upon the

baseline processes described in this section.

2.3.1 Substrate material

The basic idea of optical interconnects is to integrate polymer waveguides into printed circuit boards. This suggests the fabrication of the polymer waveguides onto substrates which are common in PCB manufacturing. These are mainly large-area substrates, with sizes above $300\text{ mm} \times 450\text{ mm}$, made out of the following base materials.

- FR4 (flame retardant), which is made of woven fiberglass cloth with an epoxy resin matrix, is the most widely used material in PCB manufacturing. The main drawbacks for the waveguide fabrication are the weaviness of the surface and the lack of good dimensional stability.
- Polyimide (PI) is mainly used as thin layer in the range of 25 - 100 μm thickness. It provides good chemical stability and an even surface.
- LCP (liquid crystal polymer) based sheets are used because of their excellent dielectric properties in the high-frequency range above 5 GHz. The drawback of the LCP material is the high price and the difficult lamination process.

The polymer waveguide technology described herein is in particular compatible with, but not limited to, FR4 and PI substrates.

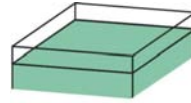
2.3.2 Polymer material

In order to enable a successful polymer waveguide technology, we set the following requirements for the polymer material as imperative,

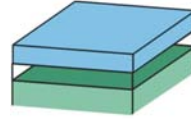
- compatibility to established PCB fabrication processes in order to enable cost-efficient manufacturing and lower the entry-barrier for manufacturers;
- material deposition and waveguide core patterning provide scalability to large-area substrate manufacturing;
- very low intrinsic light absorption ($\leq 0.05\text{ dB/cm}$) in the $\lambda = 850\text{ nm}$ wavelength range to enable low-loss waveguides;
- high reliability and long term stability.

Among the materials we have evaluated so far, polysilsesquioxanes PSSQ, a family of highly crosslinked silicon-based polymers [16], are the most promising candidates. A commercial version of the material is available as LIGHT LINK from DOW CHEMICAL. This solvent based, negative-tone polymer requires UV and thermal cure procedures to eventually reach full strength. The superior long term stability

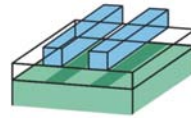
1) Lower cladding deposition on the substrate and subsequent UV flood exposure



2) Core layer deposition with the desired thickness



3) UV exposure to transfer the waveguide pattern into the core material



4) Deposition of upper cladding to embed the waveguide core

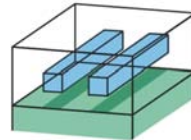


Figure 2.2: Basic steps required for the fabrication of a single polymer waveguide layer.

has been demonstrated by waveguides which have been exposed to $85^{\circ}\text{C} / 85\% \text{rH}$ for more than 5000 h [16].

In addition we use a polyurethane PU based material for certain functionality tests. This material does not withstand the reliability tests. On the other hand, the processing is less demanding and therefore sometimes more adequate for test vehicles.

The basic processes for both materials are similar. In general, we fabricate the waveguides in a layer based process. The final waveguide stack will eventually be embedded in, attached to, or placed onto a PCB.

2.3.3 Polymer deposition

We start with the deposition of the lower cladding material. We employ doctor blading, spray coating, spin coating and ink-jet printing to deposit the liquid polymer, see Figure 2.2. Ink-jet printing is the most advanced method and will eventually be the choice for production, in particular also because of the provided layer thickness controllability which is required in particular for the connectorization. However, for small-scale experimental samples, as used in this work, spin-coating and doctor-blading are favorable. Spin coating is herein used to fabricate layers between

2 Optical interconnects

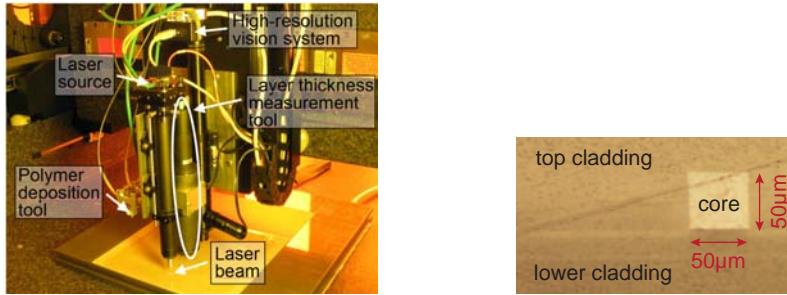


Figure 2.3: Laser-beam shaping unit and auxiliary tools mounted on the movable stage of the laser direct writing tool (left) and waveguide cross-section of rectangular polymer waveguide (right).

5 μm and 20 μm thick. Doctor blading uses a blade or bar moved over the substrate maintaining a constant gap to the substrate. Thereby, the liquid material is squeezed over the substrate. This results in a smooth layer slightly thinner than the set gap between blade and substrate.

The UV flood exposure of the cladding material is performed with the collimated HgXe (mercury-xenon) light source LOT ORIEL, which provides an intensity peak in the 365 nm wavelength range. The PSSQ material requires an additional post-exposure bake PEB and hard bake step.

2.3.4 Waveguide core patterning

The UV sensitive core material can be patterned by using mask-photolithography or by laser direct writing. The focus of our group is on laser direct writing for large scale substrates. The advantages are the adaptability of the core pattern to the unavoidable substrate distortions and the flexibility to implement design changes. Furthermore, large scale mask patterning is critical regarding the gap between mask and liquid polymer during the proximity exposure.

The laser writing system is based on a high-precision three-axis linear robot system, the so called gantry-system, see Figure 2.3. A diode-laser head ($\lambda = 372 \text{ nm}$) with variable spot size (35 - 50 μm), a high-resolution camera and an optical confocal distance sensor are mounted on the moving platform. These tools are used for the UV-exposure, substrate mapping and layer thickness control, respectively.

3 Theory of multimode optical waveguides

Polymer optical waveguides are used within optical interconnect applications to transmit the optical signals. This chapter deals with the propagation of light waves in light-guiding dielectric structures. An analytical solution can be found for the electro-magnetic field-distribution in a one-dimensional structure. Such a slab waveguide is described in Figure 3.1 and represents the simplest configuration of dielectric media in order to yield light-guiding. Using some simple approximations, we can find analytical solutions also for the field distribution in more complex waveguides. As examples of these, we will present the solutions for ideal-rectangular (Figure 3.5) and ideal-circular dielectric waveguides (Figure 3.10), which are based on the MARCATILI method and the weakly-guiding approximation, respectively. The optical modes, which represent the possible electro-magnetic field distributions for the presented waveguide type, are then described as interference pattern of plane waves propagating in the waveguide.

3.1 Introduction

Dielectric optical waveguides guide the light waves in a specific direction. The basic configuration of such a waveguide consists of two different dielectric materials, whereby a layer of the first dielectricum is embedded in the other material. They feature different refractive indices n_1 and n_2 , respectively. Light impinging on the boundary between the two dielectric media is refracted according to SNELL'S law [33]. An effect known as total internal reflection (TIR) occurs for light propagating from a region of higher refractive index to a lower one [33]. In this case, electromagnetic waves with an incident angle larger than the complementary critical angle θ_c are completely reflected [94], see Figure 3.1. Thus, light guiding is obtained for light with a propagation angle below the critical angle θ_c in dielectric structures, according to Figure 3.1, where $n_1 > n_2$ applies. Herein, the critical angle is measured with respect to the propagation axis, while the complementary critical angle is related to the surface normal of the dielectrica boundary.

3.2 Dielectric slab waveguides

A dielectric slab waveguide consists of a three-layer stack of dielectric media. It represents one of the simplest waveguide structures and provides the advantage of an analytical solution for the electromagnetic field distribution therein. Herein described is the analytical solution according to [43]. In Figure 3.1, the symmetric slab waveguide configuration is depicted in detail. The core material with a refractive index n_1 and a thickness of $2d$ is embedded between two cladding layers with n_2 , whereby $n_1 > n_2$ to provide total internal reflection and thus light-guiding along the z -axis. The cladding layer is considered to be infinite compared to the waveguide structure.

The wave optics approach to describe the electromagnetic field distribution in the slab waveguide starts from MAXWELL'S equations [94]. The light wave propagates in z -direction with a propagation constant β along this axis, described as electric and magnetic field as follows

$$\mathbf{E} = \mathbf{E}_0(x, y)e^{j(\omega t - \beta z)} \quad (3.1)$$

$$\mathbf{H} = \mathbf{H}_0(x, y)e^{j(\omega t - \beta z)} \quad . \quad (3.2)$$

Two assumptions are applied in order to simplify the problem-solving. (i) First assumption: all components of the field are constant in y -direction, thus, yielding the corresponding partial derivative to be set equal to zero, e.g. $\frac{\partial}{\partial y} H = \frac{\partial}{\partial y} E = 0$. (ii) Second assumption: there is no magnetic field component in the propagation direction for transverse magnetic (TM) waves, i.e. $H_z^{TM} = 0$, and no electric field component in the propagation direction for transverse electric (TE) waves, i.e., $E_z^{TE} = 0$.

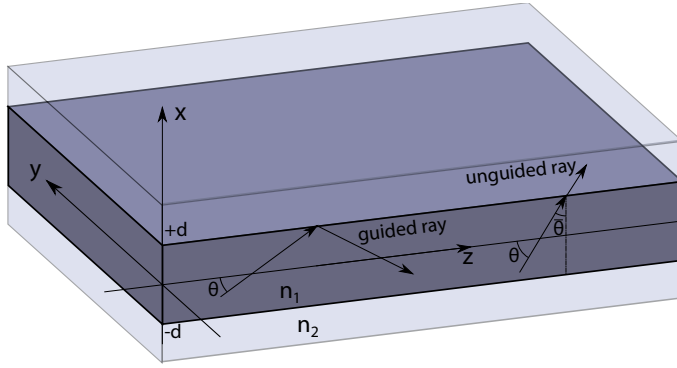


Figure 3.1: Slab waveguide structure, whereby the core region, consisting of the dielectric material with refractive index n_1 , is embedded within in the cladding, a dielectric material with refractive index n_2 , while $n_1 > n_2$ to yield light guiding for rays with a propagation angle θ smaller than the critical propagation angle θ_c .

The electro-magnetic field in a slab waveguide can be described as TM and TE modes. Therefore, the TE modes include the non-zero H_z -components, and the TM modes include the non-zero E_z -components. For the understanding of the electromagnetic field distribution in a waveguide, it is sufficient to discuss one kind of modes [43]. Herein, the solutions for the TM modes are considered only. The solutions for the TE modes can be derived in a similar way [43].

To obtain H_y , Equation 3.2 and the aforementioned assumptions are inserted into the wave equation [43]

$$\nabla^2 \mathbf{H} + (n_i k)^2 \mathbf{H} = 0 \quad i = 1, 2 \quad (3.3)$$

which leads to

$$\frac{\partial^2 H_y}{\partial x^2} + (n_i^2 k^2 - \beta^2) H_y = 0 \quad i = 1, 2 \quad (3.4)$$

where n_i represents the refractive index of the cladding n_1 or the core n_2 , respectively.

The solution of Equation 3.4 is either trigonometric, for $(n_i^2 k^2 - \beta^2) > 0$, or exponential, for $(n_i^2 k^2 - \beta^2) < 0$. To fit the boundary conditions of guided waves, the trigonometric solutions are applied for the core region, and the exponential solutions for the cladding region. Thus, the core region is described by $\cos(Kx)$ and $\sin(Kx)$ with

$$n_1^2 k^2 - \beta^2 = K^2 \quad |x| < d \quad (3.5)$$

and the cladding region with $e^{\gamma x}$ or $e^{-\gamma x}$ with

$$n_2^2 k^2 - \beta^2 = -\gamma^2 \quad |x| > d \quad (3.6)$$

The range of values for the propagation constant β which satisfy Equations 3.5

3 Theory of multimode optical waveguides

and 3.6 are limited to

$$n_1 k > \beta > n_2 k \quad . \quad (3.7)$$

The magnetic field component can now be calculated for the core region

$$H_y = A \cos(Kx) + B \sin(Kx) \quad (3.8)$$

and in the cladding

$$H_y = C e^{-\gamma x} + D e^{\gamma x} \quad . \quad (3.9)$$

The requirement for continuity of the tangential magnetic field at $x = d$, a boundary condition which applies for dielectric interfaces, gives

$$A \cos(Kd) = C e^{-\gamma d} \quad , \quad (3.10)$$

for the even TM modes, and for the odd ones

$$B \sin(Kd) = C e^{-\gamma d} \quad . \quad (3.11)$$

From Equations 3.8 and 3.9, as well as 3.10, one can derive the following expressions for the even TM modes

$$H_y = \begin{cases} A \cos(Kd) e^{-\gamma(x-d)} & \text{upper cladding} \\ A \cos(Kx) & \text{core} \\ A \cos(Kd) e^{\gamma(x+d)} & \text{lower cladding} \end{cases} \quad (3.12)$$

and the odd TM modes one can find

$$H_y = \begin{cases} B \sin(Kd) e^{-\gamma(x-d)} & \text{upper cladding} \\ B \sin(Kx) & \text{core} \\ -B \sin(Kd) e^{\gamma(x+d)} & \text{lower cladding} \end{cases} \quad . \quad (3.13)$$

Thereby, d and $-d$ are representing the x -coordinates of the boundaries, while A , B , K , and γ are constants.

Propagating modes

By using MAXWELL'S equations $\nabla \times \mathbf{E} = -\frac{\partial \mathbf{B}}{\partial t}$ and $\nabla \times \mathbf{H} = \frac{\partial \mathbf{D}}{\partial t}$, as well as $\epsilon_r = n_i^2$, for $i = 1, 2$, all components of the electromagnetic field relevant for TM modes can be obtained as follows

$$\begin{aligned}
E_x &= \frac{\beta}{\omega\epsilon_r\epsilon_0} H_y \\
E_y &= 0 \\
E_z &= \frac{j}{\omega\epsilon_r\epsilon_0} \frac{\partial H_y}{\partial x} \\
H_x &= 0
\end{aligned} \tag{3.14}$$

$$H_y = A \cos(Kx) + B \sin(Kx) \begin{cases} B = 0 & \text{even TM mode} \\ A = 0 & \text{odd TM mode} \end{cases}$$

$$H_z = 0 \quad .$$

Solutions for K and γ determine the propagating modes in a slab waveguide. Continuity of the tangential electric field component E_z is applied as boundary condition for even TM modes at $x = d$, and thus $n^2 Ak \sin(Kd) = \gamma C e^{-\gamma d}$. Dividing this by Equation 3.10 gives the characteristic equation for even TM modes

$$n^2 K d \tan(Kd) = \gamma d \quad , \tag{3.15}$$

and analogously by using Equation 3.11 for the odd modes one obtains

$$-n^2 K d \cot(Kd) = \gamma d \quad . \tag{3.16}$$

as characteristic equation, whereby $n = \sqrt{\epsilon_1/\epsilon_2} = n_1/n_2$ applies.

Eliminating β^2 from Equations 3.5 and 3.6 yields $(Kd)^2 + (\gamma d)^2 = k^2 d^2 (n_1^2 - n_2^2)$. By introducing the characteristic parameter V as normalized frequency of the guide, one obtains

$$(Kd)^2 + (\gamma d)^2 = V \quad , \tag{3.17}$$

whereby

$$V = kd \sqrt{n_1^2 - n_2^2} \quad . \tag{3.18}$$

Graphical methods are proposed to solve the transcendental Equations 3.15 and 3.17 [43]. Both equations are plotted as solid lines in the Kd - γd plane, shown in Figure 3.2. The parameter V is represented in this graph by a circle. Each intersection of the solid line with this circle, represents an even TM mode.

The characteristic equation for the odd TM modes, Equation 3.16, is also plotted in Figure 3.2, represented by a dashed line. Thus, each intersection of this dashed line with the circle (V), represents an odd TM mode.

The transverse magnetic modes are labeled with TM_i . Thereby even numbered subscripts represent even TM modes and odd subscripts represent odd modes. These indices are called the order of the mode.

TE Modes

According to [43], the TE modes can be expressed as

$$E_y = \begin{cases} A \cos(Kx), & \text{even TE mode} \\ B \sin(Kx), & \text{odd TE mode} \end{cases} \tag{3.19}$$

3 Theory of multimode optical waveguides

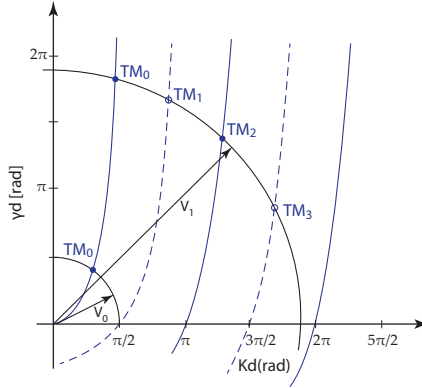


Figure 3.2: Even TM modes (solid lines $n^2Kd \tan(Kd) = \gamma d$) and odd TM modes (dashed line $-n^2Kd \cot(Kd) = \gamma d$) as graphical solution in the Kd - γd plane, whereby $V = kd \sqrt{n_1^2 - n_2^2}$.

for the core region, and

$$E_y = \begin{cases} Ce^{-\gamma x} & \text{upper layer} \\ De^{\gamma x} & \text{lower layer} \end{cases}, \quad (3.20)$$

in the two cladding regions. The characteristic equations for TE modes are

$$Kd \tan(Kd) = \gamma d, \quad \text{even TE mode} \quad (3.21)$$

$$-Kd \cot(Kd) = \gamma d, \quad \text{odd TE mode.} \quad (3.22)$$

The only noticeable difference between the characteristic equations of the TM and TE modes lies in the material depending factor n^2 applied for the TM modes. The corresponding factor for the TE modes yields unity, because $\mu = \mu_1/\mu_2 = 1$. This is, because the considered dielectrics are non-magnetic.

Field distribution

The graph in Figure 3.2 shows that only a certain number of discrete modes can exist in a slab waveguide. The normalized thickness parameter V determines the number of modes. For values of $V < \pi/2$, only one mode can propagate, representing a singlemode slab waveguide. For all other possible values of V the waveguide is called to be multimode. Furthermore, the graph in Figure 3.2 exhibits, that the number of modes is increased by one for every $\pi/2$ -increase of V .

Figure 3.3 shows the magnetic field distribution H_y for the TM modes obtained from the graphical solution of a slab waveguide shown in Figure 3.2. The symmetric even TM modes exhibit a maximum at the center $x = 0$, while the asymmetric odd TM modes exhibit a zero-crossing.

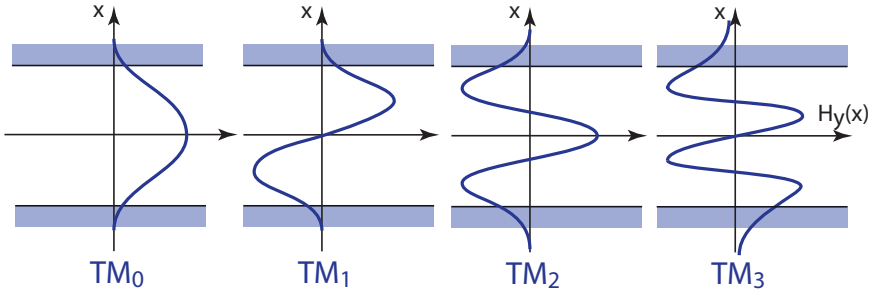


Figure 3.3: Solutions of the magnetic field distribution in a slab waveguide, representing the four lowest order TM modes, $TM_0 \dots TM_3$, exhibiting the sinusoidal characteristic in the core region and the exponential decay in the cladding.

Plane wave method

The periodic magnetic field distribution of the TM modes in the core section of the waveguide, shown in Figure 3.3 can be represented as interference pattern of two plane waves under an angle. The waves, represented by rays in Figure 3.1, are propagating in a zig-zag-pattern in the slab waveguide. To yield the specific field pattern of a TM mode, the waves propagate with a specific angle, which is related to the order of the TM mode. One wave propagates slightly upward under an angle $+\theta_N$ and the other one downward with $-\theta_N$, whereby N represents the order of the TM mode. The propagation angle can be calculated as

$$\theta_N = \arccos\left(\frac{\beta_N}{n_1 k}\right) . \quad (3.23)$$

The minimum value of the propagation constant is $\beta > n_2 k$, according to Equation 3.7. This yields the angle

$$\theta_c = \arccos\left(\frac{n_2}{n_1}\right) \quad (3.24)$$

which describes the maximum acceptance angle.

The electromagnetic field penetrates into the cladding layer with an exponential decay therein, illustrated in Figure 3.3. In the plane wave approach, this is accounted by an effective reflection plane located in the cladding and not exactly at the core-cladding interface, see Figure 3.4. This leads to the GOOS-HÄNCHEN-shift between the incident and reflected beams along the dielectric boundary [49, 43].

3 Theory of multimode optical waveguides

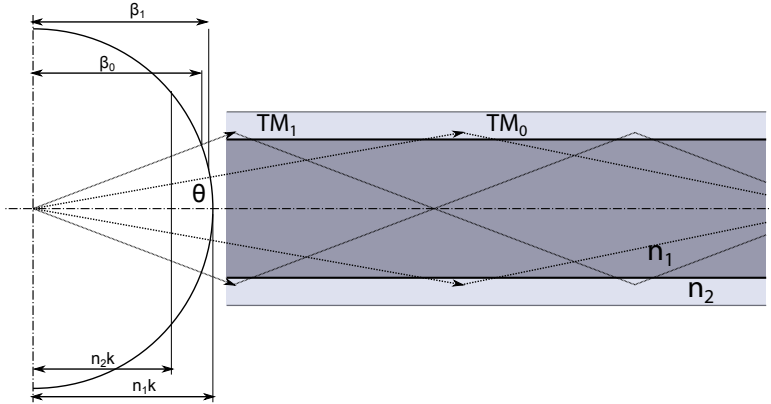


Figure 3.4: and the bounce angles θ_N of a slab waveguide shown in the k_z and k_y space.

3.3 Rectangular dielectric waveguides

A rectangular dielectric waveguide confines, in contrast to the slab waveguide, the optical waves in two dimensions. An ideally rectangular cross-section geometry according to Figure 3.5 is considered as rectangular waveguide herein. Only the very simple configuration of a rectangular core region with refractive index n_1 , embedded in the cladding material n_2 , is considered here.

The convention for mode designation in a rectangular dielectric waveguide is different to the case of a dielectric slab waveguide. The E^x and E^y modes are similar to the TM modes and the TE modes, respectively. Their mode numbers represent the number of extrema in the field distribution. The mode E_{pq}^i with $i = x, y$ represents a mode with p and q extrema in the x - and y -direction, respectively.

Marcatili

A widely used approach to find the approximate solution for the modes of a rectangular waveguide has been proposed by MARCATILI [75], which is explicitly described in [54]. The simplification in this method considers the field components in the four dashed regions in Figure 3.6 as negligible. Thus, the continuity conditions for the electric and magnetic fields are only imposed at the four interfaces between core and cladding. The basic idea is to consider the rectangular waveguide as the superposition of two slab waveguides, one oriented in x -direction and one in the y -direction, respectively. The dispersion equation now has to be satisfied in both directions.

The polarization of E_{pq}^x is in the x -direction, and thus $E_y = 0$. The principal field components of this modes are E_x and H_y . The boundary conditions are: continuity of E_x and H_z at $y = \pm h$, and continuity of E_z and H_y at $x = \pm w$. The waveguide is invariant in z -direction, and thus the partial derivatives in the z -direction are constant at $-j\beta$. The propagation constant β is related to the effective refractive

3.3 Rectangular dielectric waveguides

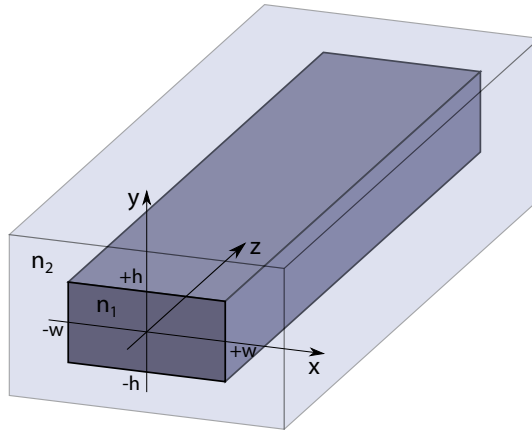


Figure 3.5: Rectangular waveguide structure, whereby the core region n_1 is embedded within in the cladding dielectrics n_2 , while $n_1 > n_2$ to yield light guiding.

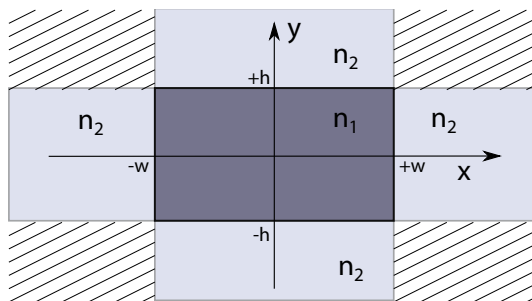


Figure 3.6: Cross-section of rectangular waveguide structure with the dashed corner regions omitted as acceptable simplification to calculate the modes according to MARCATILI [75], as described in [54].

3 Theory of multimode optical waveguides

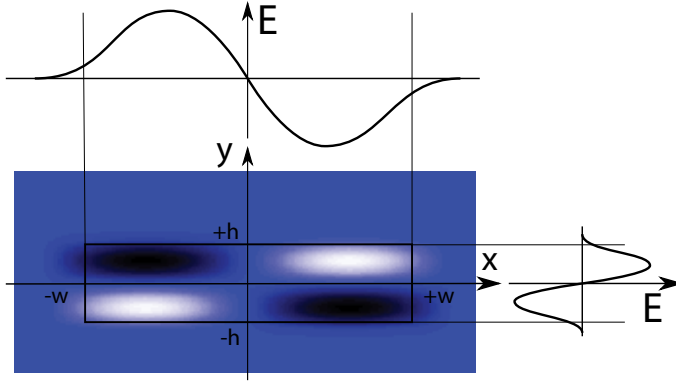


Figure 3.7: Electric field distribution for a $TM_{p=1,q=1}$ mode in a rectangular dielectric waveguide.

index n_{eff} and the wave number in vacuum k_0 by $n_{eff} = \beta/k_0$.

The relation between the wave vector components and the propagation constant β can be found [54] as

$$k_x^2 + k_y^2 + \beta^2 = k_0^2 n_1^2 \quad (3.25)$$

$$\gamma_x^2 = k_0^2 (n_1^2 - n_2^2) - k_x^2 \quad (3.26)$$

$$\gamma_y^2 = k_0^2 (n_1^2 - n_2^2) - k_y^2 \quad (3.27)$$

Parameter γ_i is introduced to ease the notation of the subsequent equations.

The approach is to treat the rectangular waveguide as a combination of two perpendicular slab waveguides, which are related by Equation 3.25. Thus, in analogy to the slab waveguide approach, the characteristic equations in x - and y -direction can be stated [54] as

$$k_y h = \arctan\left(\frac{\gamma_y}{k_y}\right) + q \frac{\pi}{2} \quad q = 0, 1, 2, \dots \quad (3.28)$$

$$k_x w = \arctan\left(\frac{n_1^2 \gamma_x}{n_2^2 k_x}\right) + p \frac{\pi}{2} \quad p = 0, 1, 2, \dots \quad (3.29)$$

whereby Equation 3.29 is simplified by the assumption $k_0 n_{1,2} \gg k_y$. This restricts the application to waveguides with small refractive index difference $n_1/n_2 - 1 \ll 1$ and, hence, to modes with small propagation angles [115].

The propagation constant β can now be derived by (i) numerically solving Equation 3.29, by incorporating Equation 3.26, to obtain the wave vector x -component k_x ; in a similar way (ii) k_y can be obtained from Equation 3.27 and 3.28; and in a final step (iii), the propagation constant β is calculated using Equation 3.25.

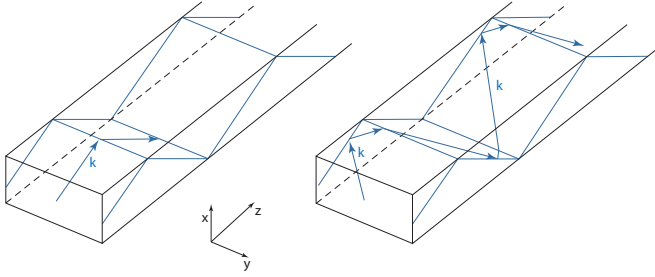


Figure 3.8: Propagating light rays in a dielectric waveguide; with wave-vector components in x -direction only (*left*), and with vector components in both, x - and y -direction (*right*), respectively.

The resulting electric field distribution for a TM-like mode is shown in Figure 3.7. Analogous to the slab waveguide, the field distribution of one mode in the core region is a superposition of sinusoidal solutions in the x - and y -direction, while in the cladding region an exponential decay occurs. Due to the approximation of omitting the field in the cladding regions close to the corners (dashed regions in Figure 3.5) and the assumption $k_0 n_{1,2} \gg k_y$, the MARCATILI method is in particular valid for modes far from the cut-off.

Plane wave method

The electro-magnetic field distribution of the TM_{11} mode shown in Figure 3.7, can be represented as interference pattern. In contrast to the previously described slab waveguide, there are four plane waves required to obtain such a pattern, two propagating in the xz -plane and two in the yz -plane, respectively. This can be represented as a light ray with k_x and k_y wave vector components. This is illustrated in Figure 3.8 (*right*) by a light ray, which is reflected at all four core/cladding interfaces. Figure 3.8 (*left*) shows the special case of a ray propagating only in the xz -plane. Thus, the wave vector has no k_y components. This case is similar to the modes in a slab waveguide.

A descriptive way to show the modes in a rectangular waveguide is to designate their respective wave vector components in the k_x - k_y -plane. In Figure 3.9, the k -vector components of the TM modes in a waveguide are represented by dots in the k_x - k_y -space. Lower order modes are closer to the origin. The propagation conditions for the k -vector are

$$\sqrt{k_x^2 + k_y^2} \leq n_1 k_0 \sin \bar{\theta}_c \quad (3.30)$$

[94], whereby $n_1 k_0 \sin \bar{\theta}_c$ is represented as circle in the k_x - k_y -plane in Figure 3.9. The dots are approximately spaced by $\pi/2w$ and $\pi/2h$ in the k_x - and k_y -direction, respectively.

The number of modes can be approximated by counting the dots in the inner circle of the k_x - k_y -diagram shown in Fig 3.9 [94]. This leads to the approximation

3 Theory of multimode optical waveguides

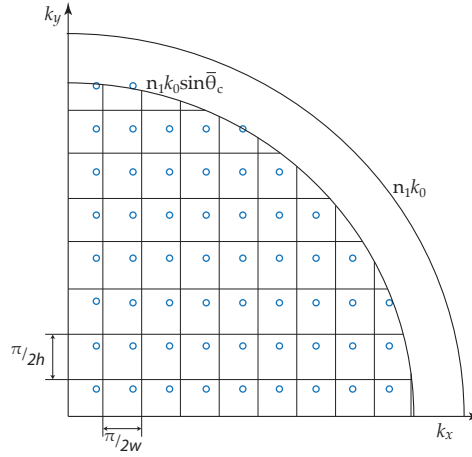


Figure 3.9: Circles represent the k -vector components of the modes in a rectangular dielectric waveguide in the k_x - k_y -space.

$$M \approx \pi \frac{4wh}{\lambda^2} NA^2 \quad , \quad (3.31)$$

for the number of guided modes M in a rectangular waveguide. The inner circle is thereby described by Equation 3.30 and indicates the propagation condition for the k -vector.

3.4 Weakly-guided step-index fiber

A step-index fiber consist of a circular core region with a refractive index n_1 , embedded in an annular cladding n_2 , shown in Figure 3.10, whereby $n_1 > n_2$. It represents the simplest index profile configuration of a fiber. The key parameters of the fiber structure include the core radius a and the normalized index difference Δ , defined as

$$\Delta = \frac{n_1^2 - n_2^2}{2n_1^2} \quad .$$

Herein, only fibers are considered which meet the weakly-guiding approximation criteria $\Delta \ll 1$. Therefore, the difference between the refractive indices of core and cladding are very small, i.e., $n_1 \approx n_2$, which leads to $\Delta \approx \delta n/n_1$. This statement is true for the majority of glass fibers [7]. The calculation of the linearly polarized modes described in the following is according to [7]. The numerical aperture ($N.A.$) defines the maximum acceptance angle for rays incident on the front facet, $N.A. \equiv \sin \theta_{N.A.} = n_1/n_2 \sqrt{2\Delta}$. The $N.A.$ and the fiber core diameter are in particular of importance for practical applications of optical fibers.

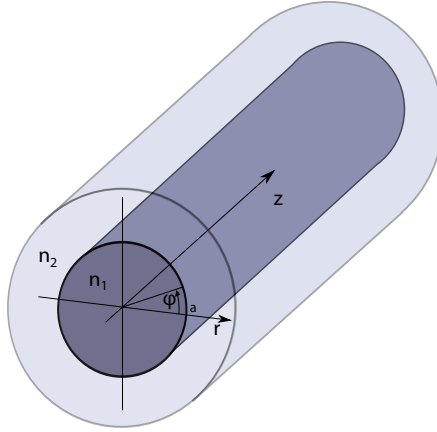


Figure 3.10: Structure of a circular step-index fiber with n_1 and n_2 representing the refractive indices for core and cladding, respectively.

The electromagnetic field distribution in the fiber is calculated for the linearly polarized LP modes. The LP modes are approximations for TE, TM, and hybrid modes under the aforementioned weakly-guiding criteria. They are, in contrast to the hybrid modes, linearly polarized and can thus be described by an electric field component in x -direction and a magnetic field component in y -direction, using the cylindrical coordinates with the components r , ϕ , and z . The weakly-guiding properties of the fibers lead to electromagnetic field components which are orthogonal and predominantly perpendicular to the propagation axis z .

Starting from the Helmholtz vector equations $\nabla^2 \mathbf{E} + k^2 \mathbf{E} = 0$ and $\nabla^2 \mathbf{H} + k^2 \mathbf{H} = 0$, one can derive the wave equation for a propagating plane wave with rectangular components as

$$\nabla_i^2 E_x + (n_1^2 k_0^2 - \beta^2) E_x = 0, \quad r \leq a$$

in the core region and

$$\nabla_i^2 E_x + (n_2^2 k_0^2 - \beta^2) E_x = 0, \quad r > a$$

in the cladding region. The wave equation for variations in r and ϕ is

$$\frac{\partial^2 E_x}{\partial r^2} + \frac{1}{r} \frac{\partial E_x}{\partial r} + \frac{1}{r^2} \frac{\partial^2 E_x}{\partial \phi^2} + (n_i^2 k_0^2 - \beta^2) E_x = 0 \quad i = 1, 2 \quad . \quad (3.32)$$

The solutions for the electric field components E_x are expected to be a set of discrete modes. Each mode depends on r , ϕ , and z according to $E_x = R\Phi e^{-j\beta z}$. By substituting this expression into Equation 3.32 and introducing the constant l^2 , this can be separated into

$$\frac{d^2 \Phi}{d\phi^2} + l^2 \Phi = 0 \quad (3.33)$$

3 Theory of multimode optical waveguides

and

$$\frac{d^2 R}{dr^2} + \frac{1}{r} \frac{dR}{dr} + \left[(n_i^2 k_0^2 - \beta^2) - \frac{l^2}{r^2} \right] R = 0 \quad . \quad (3.34)$$

After separation, Equation 3.33 only involves the function Φ which depends on the azimuthal parameter ϕ . It can be solved as

$$\Phi(\phi) = \begin{cases} \cos(l\phi + \alpha) \\ \sin(l\phi + \alpha) \end{cases} \quad . \quad (3.35)$$

The integer l represents the azimuthal mode number for linearly polarized modes, LP_{lm} , while α is a constant phase shift. This solution for the azimuthal function exhibits a sinusoidal variation of the field for the angular parameter in case $l \geq 1$. For $l = 0$, the amplitude of the electromagnetic field is constant along the azimuthal parameter ϕ .

Equation 3.34 is a form of the Bessel Differential Equation. The corresponding solutions are the Bessel functions of the first kind J_n and the modified Bessel function of the second kind K_n . Evaluating the Bessel coefficients and setting the boundary conditions accordingly, see [7], the electric field can be described as

$$E_x = \begin{cases} E_0 J_l(ur/a) \cos(l\phi) e^{-j\beta z}, & r \leq a \\ E_0 \left[\frac{J_l(u)}{K_l(w)} \right] K_l(wr/a) \cos(l\phi) e^{-j\beta z} & r > a \end{cases} \quad (3.36)$$

with a being the radius of the core region, while the parameters u and w are determined as

$$\begin{aligned} u &= a \sqrt{n_1^2 k_0^2 - \beta^2} \\ w &= a \sqrt{\beta^2 - n_2^2 k_0^2} \quad . \end{aligned} \quad (3.37)$$

The eigenvalue equation for the LP modes is derived as

$$\frac{J_{l-1}(u)}{J_l(u)} = -\frac{w}{u} \frac{K_{l-1}(w)}{K_l(w)} \quad . \quad (3.38)$$

The solution of this transcendental equation requires graphical or numerical methods, see Figure 3.11 [7]. The normalized frequency parameter V contains the structural parameters of the fiber and the wavelength of interest, and is calculated as

$$V = \sqrt{u^2 + w^2} = n_1 a k_0 \sqrt{2\Delta} \quad . \quad (3.39)$$

The left-hand and right-hand side of Equation 3.38 are calculated as function of the parameter u . The solution of the left-hand-side equation leads to curves which exhibit a tangent function like behavior. The asymptotes and zeros are defined by the zeros of the ordinary Bessel function $J_l(V)$. Positive and negative parts of all branches are assigned to the radial mode number m [7].

3.4 Weakly-guided step-index fiber

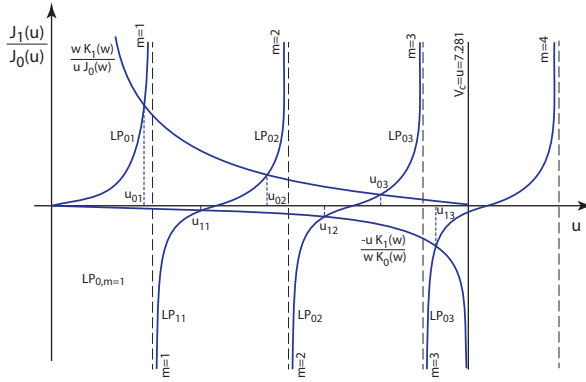


Figure 3.11: Graphical solution of Equation 3.38 to obtain the parameter u_{lm} for $l = 0, 1$ and $m = 1 \dots 3$ of the respective mode LP_{lm} .

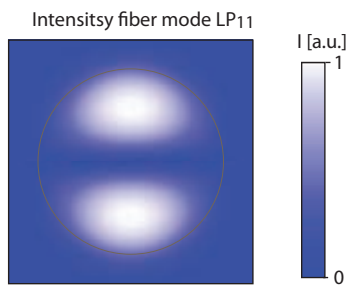


Figure 3.12: Mode field pattern of the linearly polarized LP_{11} mode in a step index fiber with $N.A. = 0.1$ and $r = 7.4 \mu\text{m}$.

3 Theory of multimode optical waveguides

Intersections between the left-hand and right-hand side of Equation 3.38 provide the solution for the parameter u_{lm} . Thereby, each intersection represents the accordingly linearly polarized LP_{lm} mode. The parameter w and the propagation constant β can then be calculated using Equation 3.39 and Equations 3.37, respectively. The parameters u , w , and β are then inserted into Equations 3.36 to obtain the field distribution in the core and cladding region, respectively, see Figure 3.12.

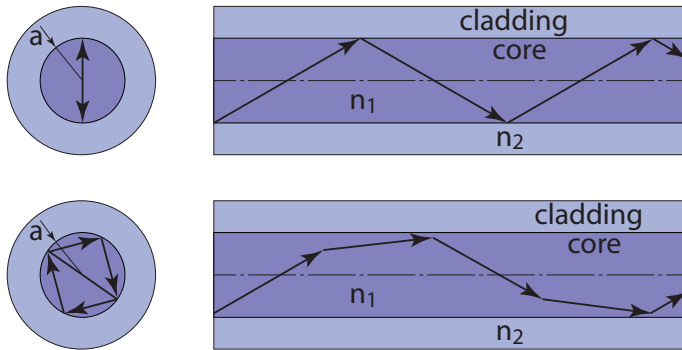


Figure 3.13: Modes in a step-index fiber, with core radius a , described by meridional rays (*top*) and skew rays (*bottom*).

Plane wave method

In analogy to the slab and rectangular waveguide, the electro-magnetic field distributions in the fiber can be described by propagating plane waves which constructively interfere. The wave vector of these waves can be represented by propagating rays in the waveguide. One kind of occurring rays are the meridional rays, see Figure 3.13 (*top*). These rays, which have radial propagation components only, propagate in a zig-zag pattern within the meridional plane. The resulting interference pattern exhibits variations in the radial dimension, but is constant for azimuthal variations, e.g. LP_{lm} for $l = 0$ and $m = 1, 2, \dots$. The other kind are the skew rays, which describe a helical spiral in the fiber, according to Figure 3.13 (*bottom*). They have radial and azimuthal components of the propagation vector and yield electromagnetic field patterns with radial and azimuthal variations, e.g. LP_{lm} for $l = 1, 2, \dots$ and $m = 1, 2, \dots$.

4 Micrometer-accurate passive-alignment of components in PCBs¹

The goal of the work described in this chapter is to achieve passive alignment of components into printed circuit boards with micrometer-accuracy. The herein proposed approach overcomes the discrepancy in alignment tolerances between printed circuit board manufacturing and multimode optics. PCB substrates provide a cost-efficient basis for optical interconnect applications, but they are subject to position tolerances of up to 100 μm over the total board size. In contrast, multimode optics require alignment tolerances which are one order of magnitude lower. The approach makes use of alignment features which provide an acceptable position tolerance within their close vicinity. These localized alignment features are fabricated exclusively using standard PCB manufacturing equipment. They provide a mechanical datum for accurate passive alignment of components on the substrate. The pattern of the multimode waveguide is adjusted to the actual position of the alignment features during the laser-direct writing. In particular demonstrated is the assembly of connectors, which provide the standard MT interface, within a transversal positioning tolerance below $\pm 5 \mu\text{m}$. Thus, the additional coupling loss introduced by misalignment is below 0.5 dB.

¹Part of this work has been published in [65], and led to issued patents [62, 63, 19]

4.1 Introduction

Several components have to be assembled onto a PCB to establish on-board optical communication links. One major obstacle for the integration of such optical elements into standard electronic systems, is the large gap in positioning tolerances between the optics and the electronics regime. In standard PCB processing, manufacturing tolerances of as much as 100 μm , are acceptable. In the world of optics, however, the tolerances for mutual alignment between multimode building blocks are only 5 μm . The challenge is to bridge this discrepancy in alignment requirements.

To achieve a cost-efficient assembly approach, the required alignment should be passive. Thereby, the elements are simply plugged into the board. Also, the production of the PCB should, wherever possible, use the existing standard equipment at the PCB manufacturer.

4.2 Combining optical waveguides and mechanical alignment structures on PCBs

The passive mechanical alignment of modules in the PCB needs robust alignment structures, which are accurately aligned relative to the waveguides. They can be obtained by implementing an additional process step in which alignment structures are formed by photolithography in a copper layer on the board. These copper markers are produced using – and with the same accuracy as – standard PCB layer processes, e.g., film mask exposure. Then, the waveguides are laser-written while the waveguide pattern is adjusted to compensate for the distortion of the substrate. This is where the accuracy is obtained. As a precision tool to fabricate smooth waveguides, the laser direct writing system is now also used to introduce the required alignment precision of the waveguides.

A drawing of a marker pattern and the location on the substrate is shown in Figure 4.1 (*left, center*). These markers contain both the mechanical alignment structures, for the passive alignment, and the optical reference patterns. The optical references are used to determine the adjustments needed during the laser-writing of the waveguide pattern.

4.2.1 Optical PCB fabrication procedure

A thin resin-coated copper (RCC) foil is laminated onto the upper copper layer on the PCB substrate. Then, the copper alignment markers are fabricated into the copper layer of the RCC foil, see Figure 4.1 (*center*).

On top of the substrate with the markers, the optical waveguide layers are fabricated using the established processes described in Section 2.3. Based on the copper marker positions, the proper position and adjustment of the waveguide core pattern are determined after which the pattern is exposed into the waveguide core layer.

4.2 Combining optical waveguides and mechanical alignment structures on PCBs

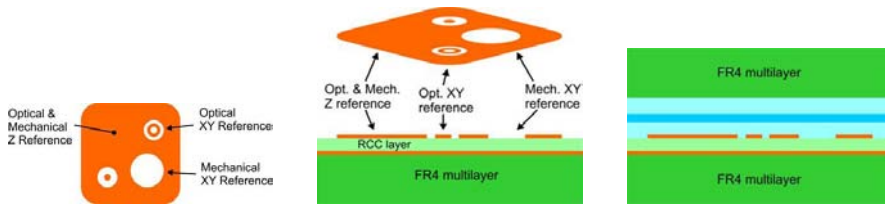


Figure 4.1: Layout of copper marker, showing optical and mechanical alignment structures (*left*), the substrate with the RCC layer and the copper marker, typically $1.5\text{ mm} \times 1.5\text{ mm}$ in size, on top (*center*), and a cross-section of copper markers in an embedded waveguide application (*right*).

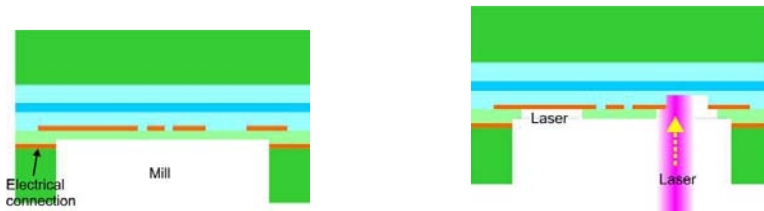


Figure 4.2: Schematic of substrate removed below markers by milling until electrical contact on continuous copper below RCC (*left*); and of cleaning away the resin from marker using a drilling laser, whereby the laser stops on copper, but drilling continues through the mechanical *xy*-reference opening (*right*).

For certain applications, the waveguides are embedded. Thus, a cover substrate is laminated thereon, as shown in Figure 4.1.

To retrieve the markers, a first milling step removes the board material below the markers. The milling depth is controlled by noting the moment of electrical contact between the milling tool and the copper layer below the markers, see Figure 4.2 (*left*). The remainder of the resin at the bottom of the markers is ablated using a drilling laser. This laser stops on copper, but continues to drill through the mechanical *xy*-reference opening in the marker so that at this position we obtain a reference slot. However, the position of this reference slot is not defined by the inaccurate laser drill, but rather by the opening in the marker, which is accurately positioned relatively to the optical reference structures. This laser-drilling step is shown in Figure 4.2 (*right*).

After the laser-drilling step, we obtain a structure with a clean copper area on the bottom surface of the marker, which can be used for accurate *z*-alignment of a mechanical element, Figure 4.2 (*right*). Furthermore, there is now an accurately-positioned alignment slot, Figure 4.2 (*right*), that can be used for *xy*-alignment of the mechanical element, as shown in Figure 4.3 (*left*). A photograph of the complete laser-drilled marker structures, consisting of a group of four markers surrounding an optical access slot in the PCB, is shown in Figure 4.3 (*right*).

4 Micrometer-accurate passive-alignment of components in PCBs

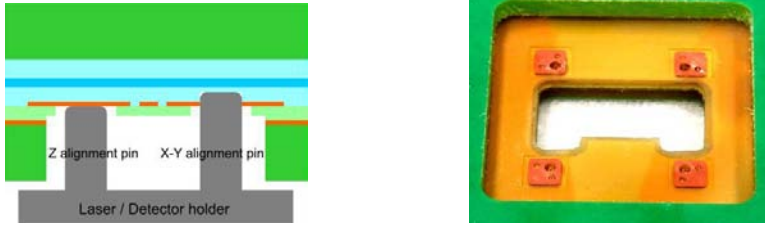


Figure 4.3: Schematic showing that the bottom of marker structure serves as mechanical z-reference, the edge of marker-defined slot as mechanical xy -reference (*left*); photograph of a set of four mechanical alignment markers after processing (*right*).

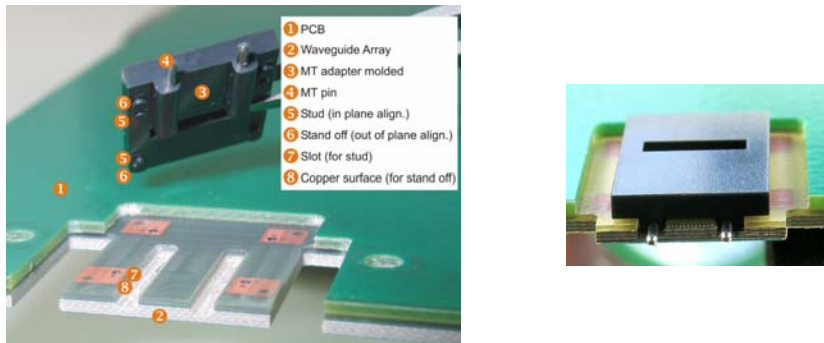


Figure 4.4: Image of injection molded MT adapter and its mating site in the optical PCB (*left*), and of injection molded MT adapter inserted in PCB with illuminated waveguides (*right*).

4.2.2 Passive alignment adapters

We typically use the passive alignment system with an intermediate adapter [21] that provides a link between the mechanical alignment structures in the PCB and the optical elements. One type is an 'MT adapter', which provides an industry-standard MT-pin interface that accepts any element conforming to this standard, be it transmitters, receivers, ribbon cables, or connectors, see Figure 4.4. At the corners of this adapter there are alignment studs that mate with the mechanical alignment slots in the copper markers on the PCB. The two MT pins to the left and right of the waveguide array provide the reference structure for the optical element or cable.

4.2.3 Passive alignment accuracy

For the passive alignment system as described in the preceding paragraph, the total alignment error between waveguide and optical element results from the accumulation of a number of alignment errors in all intermediate alignment steps. The following table lists all steps, together with the process steps that determine the accuracy of each step (in parentheses). Starting from the optical waveguide, the

steps are:

1. Position accuracy in optical PCB between waveguides and optical reference on marker (laser-writer accuracy, optical layer thickness control)
2. Position accuracy on copper marker between optical and mechanical reference (marker lithography)
3. Mechanical fit of adapter to the marker (marker etching, marker laser drill, adapter fabrication)
4. Position accuracy on adapter between marker reference and optical module reference (adapter fabrication)
5. Mechanical fit of optical module to adapter (adapter fabrication, optical module fabrication)
6. Position accuracy on optical module between adapter reference and optical element (optical module fabrication).

The main focus of this work is on steps 2 and 3, which specifically determine the performance that can be achieved using the approach employing a laser-drilled copper marker. To measure this performance, we followed two paths. On the one hand, we directly measured the alignment accuracy between an optical module and embedded waveguides. In this measurement, we tried to minimize the misalignment contributions in steps 1, 4, 5 and 6, to emphasize the effects of steps 2 and 3.

On the other hand, we also performed individual measurements on various aspects of steps 2 and 3 to obtain an exact determination of the contributions of various possible causes of inaccuracy.

These measurements as well as the direct measurement of the passive alignment of a full optical module and the detailed measurements for individual components will be described in the following paragraphs.

4.3 Measurements

4.3.1 Measurement system

Most measurements were performed using an automated three-axis positioning system, in which a measurement platform is supported by high-precision air bearings. A video camera and a height sensor are mounted on the measurement platform. The video camera and image recognition software are used to detect and measure alignment features. The height sensor is based on the chromatic-coded confocal imaging principle and used to measure vertical dimensions. All measurements provide a statistical distribution over a multiple of passive alignment marker sites or over a multiple of passive alignment insertions on one site. The measured standard

deviation includes the alignment accuracy and the measurement accuracy. Therefore, the actual standard deviation for the passive alignment will be smaller, and the value measured gives an upper limit. For the measurement system, we expect a measurement accuracy of better than $0.5\ \mu\text{m}$ for the measurements performed. The following axis convention is used: the z -direction is the vertical, out-of-plane dimension and the x - and y -directions are the horizontal, in-plane dimensions, with the x -direction along the optical axis of the waveguides.

4.3.2 Position accuracy of the copper markers

At PCB manufacturing, the marker pattern is defined using a photolithography foil mask with a resolution on the order of $5\ \mu\text{m}$. The projection optics and the wet etching of the copper provide a smoothing of the marker edge. Also, as reference pattern we used a circle with a size that is much larger than the resolution of both the mask and the measuring camera. This means that the circle edge, which is used for determining the circle center position, spans many mask and camera pixels. The resulting averaging over many pixels would, in principle, allow the position of the center of the circle to be determined with an accuracy of approximately $0.5\ \mu\text{m}$, far below the resolution of mask and camera.

We measured the position error between the optical and the mechanical reference structures on 160 markers spread over four different test cards from two different production batches. The mean position error averaged over all markers was found to be only $0.2\ \mu\text{m}$. The more important number is the standard deviation ($1.2\ \mu\text{m}$), which confirms that the local accuracy in a copper structure produced with standard PCB manufacturing technology can be sufficiently high to meet the targeted $5\ \mu\text{m}$ alignment tolerance for passive alignment.

4.3.3 Mechanical alignment slot size

The size of the mechanical alignment slot after laser drilling is crucial for accurate passive alignment because a too large slot can introduce play between alignment stud and slot. We measured the diameter of the alignment slots by using the height sensor on the positioning system to detect the edges of the slots. An average slot radius of $255.8\ \mu\text{m}$ was found, with a standard deviation of $3.3\ \mu\text{m}$.

Assuming that the adapters that must fit in these slots have alignment studs with a perfect diameter of $500\ \mu\text{m}$, there would be $5.8\ \mu\text{m}$ of clearance between the reference stud and the the alignment slot. Assuming a uniform distribution over the resulting possible position error range, the theoretical standard deviation of the position error of perfect adapters in these alignment slots is $3.4\ \mu\text{m}$.

Table 4.1: Adapter to copper marker set misalignment (standard deviation σ and mean value μ) for two test cards with 10 alignment sites each.

Board	In-plane (x,y)		Out-of-plane (z)	
	$\sigma[\mu\text{m}]$	$\mu[\mu\text{m}]$	$\sigma[\mu\text{m}]$	$\mu[\mu\text{m}]$
A	2.8	<1	23	30
B	2.1	<1	6	18

4.3.4 Alignment accuracy of silicon adapters to the alignment slots

In this measurement we determined the position accuracy of high precision silicon adapters [65] inserted into the test card, with respect to the copper markers. Insertion and clamping of the adapters into the boards was done manually, without any alignment effort. The video camera with image recognition was used to detect the position of each silicon adapter. With the two resulting position matrices, position of silicon adapters and previously measured position of the markers, the misalignment could be calculated.

Table 4.1 shows the in-plane and out-of-plane misalignment of the inserted adapters with respect to the copper marker sets, measured for 10 sites on two different boards.

For the out-of-plane measurements, we found mean values of 18 μm and 30 μm and large standard deviations. This shows that most of the adapters could not be inserted completely. By inspection of the alignment slots we found that the laser drilling of the alignment slots had introduced a slight tapering with increasing depth. Because of their sharp silicon edges, the alignment studs on the adapters got stuck in the soft polymer sidewall of the alignment slot before complete insertion was achieved. This issue only appeared during these measurements using these boards and silicon adapters. Later performed measurements, using new boards in combination with the MT adapter, were successful.

For the in-plane misalignment we found standard deviation values well below 3 μm . These values are even slightly lower than the theoretical value of 3.4 μm that was predicted in the previous section, based on the average alignment slot size. In this case, the tapering of the alignment slot has probably improved the alignment by holding the alignment studs centered in the slots.

4.3.5 Alignment accuracy between an optical module and waveguides

To align an optical module to the mechanical reference in the PCB, we used a MT standard interface adapter, similar to the one shown in Figure 4.4. The measurement concepts are described in detail in [60, 65]. Measurements performed in [65] exhibit standard deviations $\sigma_y = 2 \mu\text{m}$ and $\sigma_z = 5.4 \mu\text{m}$ for the y -direction and the z -direction,

respectively. Experience gained during the manual insertion of the adapters showed — and the measurement results confirmed — that the vertical alignment of these adapters is more critical than the horizontal alignment.

4.4 Conclusions

In the measurements we found that the position error on the copper marker itself is relatively small, with an in-plane standard deviation of only $\sigma_{in-plane} = 1.2 \mu\text{m}$ and a negligible error out-of-plane. A much more significant error is introduced by the over-etching of the marker opening that defines the position of the alignment slots. On average, the radius of the alignment slots proved to be $5.8 \mu\text{m}$ too large, which could theoretically lead to position errors between marker and adapter (step 3) with a standard deviation of $3.3 \mu\text{m}$ in-plane. This theoretical value was confirmed by further measurements of the position of silicon adapters in the markers and of the position of a measurement optical module relative to optical waveguides in the board. Both measurements yielded standard deviations on the order of $3 \mu\text{m}$.

In order to calculate the achievable position errors in the complete passive alignment system, we must also take into account the position accuracy of the optical waveguides (step 1) and the manufacturing accuracy of the adapters and optical modules (steps 4 to 6). The in-plane position accuracy of the waveguides is, thanks to the high-precision laser-writer system, very good, with a standard deviation below $1 \mu\text{m}$. However, the out-of-plane accuracy is determined by the thickness reproducibility of the waveguide layers. Based on our experience we expect a standard deviation in the order of $3 \mu\text{m}$. For the manufacturing accuracy of the adapter and optical modules we assume a standard deviation on the order of $1 \mu\text{m}$. This estimate is based on both the manufacturing accuracy known from standard commercial polymer ferrules for multimode fiber bundles and on the optical transceiver modules, which we have already demonstrated [21].

Combining the standard deviations for all steps in the passive alignment system, we arrive at an overall expected standard deviation on the order of $\sigma_{yz} = 4.5 \mu\text{m}$ for the transversal positioning. This value is within the acceptable alignment error of $\sigma_{yz}^{0.5dB} = 5 \mu\text{m}$, which is the amount of offset that would introduce an optical coupling loss of about 0.5 dB.

Thus, a successful demonstration of a novel passive alignment concept for the implementation of optics into PCBs in which we combined optical building blocks with position tolerance requirements of $5 \mu\text{m}$ with the PCB manufacturing tolerance regime of $100 \mu\text{m}$, can be reported.

4.4.1 Outlook and continuing work

The main sources of inaccuracy are, (1) the etching of the copper layer and, (2) the thickness accuracy of the cladding layers, for the in-plane and out-of-plane misalignment, respectively. The influence of the copper etching (1) can be reduced

by implementing microfine circuit technology. Recent progress in ink-jet layer deposition enables control of the cladding layer thickness (2) to within $\pm 1.5 \mu\text{m}$.

An extended passive alignment approach for flexible multilayer waveguide stacks, based on the herein proposed copper marker approach, has been demonstrated in [51]. A position tolerance of the waveguide core of $\pm 3 \mu\text{m}$ was determined for the 48 waveguide cores in the connector.

5 Concept of embedded micro-mirrors¹

This chapter introduces the concept of micro-mirrors embedded in the polymer waveguide layer. Light can be redirected by these mirrors within the waveguide plane – in-plane – and vertical to the waveguide plane – out-of-plane. The herein proposed micro-mirrors are directly fabricated on the cladding layer. The fabrication processes and tools are similar to the ones used in PCB manufacturing and the established polymer waveguide fabrication, which are designed for cost-efficient fabrication on large-scale substrates. A metallic layer, which is chemically deposited on the micro-structures, provides the reflectivity for the light. The goal is to provide advanced functionalities - in-plane corner, vertical optical via, and vertical light coupling - to the existing polymer waveguide technology by using these embedded micro-mirrors.

¹This work led to issued [17] and pending [64] patents

5.1 Introduction

State-of-the-art electrical wiring in PCBs enables routing of electrical signals in all three dimensions. Therefore, complex routing schemes can be realized to distribute the electrical signals to specific locations on the PCB. The lateral, or in-plane, routing of electrical channels is realized by structuring a metal layer on a substrate. To facilitate routing in the third dimension, electrical vias are implemented. These are vertical electrical channels connecting electrical pads on different wiring layers of the PCB. The layout of such three-dimensional electrical interconnects is mainly limited by the signal integrity for high-frequency applications. The electrical lines need to be fabricated within tight fabrication tolerances to meet the electrical impedance requirements. Electrical vias, which enable the signal routing in the vertical dimension, are unavoidably introducing imperfections in the impedance match and the signal shielding.

Optical interconnects are a research focus to cope with the expected aggregate off-chip or off-package bandwidth of 50 Tb/s at 25 GHz [45] in the near future. This will lead to some thousand optical channels running on a single optical PCB. This results in the demand for advanced waveguide routing capabilities in the optical domain to arrange all these links. As of now, the basic polymer waveguide technology, described in Section 2.3, provides straight and bent waveguide segments only. The minimum radius required for waveguide bends prevents compact waveguide routing, and the layer-based fabrication method limits the waveguides to in-plane routing. In principal, several independent optical layers can be stacked. However, they cannot be optically connected due to the lack of vertical coupling elements.

In consequence, to provide advanced and compact waveguide routing capabilities, optical turning elements need to be introduced. Herein we propose embedded micro-mirrors to redirect the optical path in- and out-of the waveguide-plane. In this way we extend the available waveguide routing features of straights, bends and crossings with sharp corners and vertical vias. Such advanced routing capabilities are expected to support our waveguide technology to master the demands of future optical interconnect applications.

5.2 State-of-the-art mirrors

Various approaches of mirrors in optical interconnects are under development. A selection of approaches are described in the following, grouped by the fabrication method.

5.2.1 Discretely fabricated optical routing elements

The herein described approaches for mirrors in optical interconnects are based on elements fabricated independently from the waveguide substrate. These mirrors are inserted and attached prior or subsequently to the waveguide fabrication process.

- Deep proton lithography makes use of a collimated proton beam to change the physical and chemical properties of optical grade PMMA. Then, either a selective etching solvent to remove the irradiated regions or monomer vapor which diffuses into the irradiated regions and expands the volume are deployed. Therewith, waveguides with a cross-section of $500\ \mu\text{m} \times 500\ \mu\text{m}$ and lens arrays have been demonstrated. Current research focus is on smaller waveguide cross-sections and the combination of lenses and waveguides within a complex optical routing element [20].
- CENTRAL GLASS provides an optical routing element whereby an array of 2×12 waveguides are redirected by 90° . The intended application is the optical coupling of horizontally placed optoelectronic elements, e.g. VCSELs and photodiodes to the waveguides in the substrate. An advantage are the vertical waveguides which are able to bridge the vertical gap between optoelectronic (OE) element and waveguides. An additional mechanical datum for alignment purposes will eventually simplify the assembly process. A similar approach has been published by NTT [39].
- KIM [56] demonstrated a stacked polymer waveguide block having double-reflection turning mirrors based on total internal reflection. Structuring the upper cladding is required to provide the air cladding for total internal reflection mirrors. Measurements show that double-reflection mirrors provide lower optical loss than single reflection mirrors.

The main drawback of this kind of approaches is the need for an assembly step of a very tiny discrete element. In order to achieve the optical alignment requirements, see Section 4, any kind of passive alignment concept might be of interest.

5.2.2 Optical routing elements fabricated by subtractive process

The approaches described herein remove part of the polymer waveguide in order to facilitate mirror surfaces.

- Several groups are working towards laser ablated mirrors [95, 23]. GHENT UNIVERSITY investigated a KrF excimer laser ablation process in acrylic polymers [37, 35, 108]. Thereby, 45° mirrors were cut into the waveguide, followed by a lift-off metallization and polymer filling of the gap.
- CHOI [11] proposes to use a microtome blade to cut a 45° facet into the waveguide to obtain an vertical coupling mirror. By cutting at elevated temperature (120°C) a smooth mirror surface is assured. Out-of-plane turning mirrors, which redirect the light path towards the substrate, have been demonstrated by coating the tilted facet with aluminum.
- Another widely investigated approach is the use of a dicing blade to cut the waveguide facet under an angle and thus to obtain an out-of-plane mirror [55]. The mirrors are either based on TIR or on the light reflection on a metal layer.

5 Concept of embedded micro-mirrors

These subtractive approaches provide tilted waveguide facets with an adequate surface quality for mirror applications. The size of dicing blades and commercial microtome blades restricts the arrangement of narrow mirrors. Both, TIR and metalized mirrors, bear drawbacks. TIR mirrors need to be protected or need an air-gap in the cladding, whereas the metallization process requires the use of shadow masks or a lift-off process, including a photolithographic step

5.2.3 Waveguide endfacet as routing element

The tilted endfacet of a waveguide acts directly as vertical coupling mirror.

- Tilted photolithography has been proposed in [111] to obtain the tilted endfacet of the waveguide core.
- Molding or casting are used to directly shape the tilted endfacet during the waveguide core formation process.

5.3 Requirements for mirrors in polymer waveguide applications

For this work, the focus is on PCB compatible fabrication for high-end applications introducing high-density waveguide patterns. Therefore, the following requirements can be derived:

- Mirrors shall be embedded in the waveguide layer during the fabrication thereof
- In-plane (lateral) redirection of the light path to provide sharp corners in the lateral waveguide path
- Out-of-plane (vertical) redirection of the light path to provide vertical light coupling
- Ability to realize multi-layer waveguide stacks
- Compatibility of the mirror fabrication with the baseline polymer waveguide fabrication processes
- Scalability to large-size substrate PCB fabrication
- Applicability of mirror-specific processes for future manufacturer

5.4 Embedded micro-mirrors

The in-plane and out-of-plane micro-mirrors proposed herein are based on metallized micro-structures. Their cross-sectional dimensions are in the range of the polymer waveguide core size, which is about $50\ \mu\text{m}$. They are created directly on the lower cladding, prior to the actual waveguide core fabrication. An improved UV-laser direct writing tool, based on the one used in the baseline polymer waveguide technology, see Chapter 2.3, is deployed to create the micro-structures. The laser direct writing tool already demonstrated the capability to fabricate polymer waveguides with a very smooth, optical-grade, sidewall. Proof therefore are the low-loss waveguides manufactured therewith. The implication is that a waveguide sidewall would also yield an appropriate mirror surface.

Once a micro-structure with the size of a waveguide cross-section and optical-grade surface is available, a reflective metal layer is required to form the desired micro-mirror. The key concept is to have a metal layer which can be deposited by a wet-chemical process and applied selectively only onto the micro-structure and not onto the surrounding lower cladding. This selectivity shall be achieved by material specific activation of the micro-structure. Thus, an additional masking layer can be avoided. The focus is on wet-chemical metal deposition in order to avoid expensive tools and to increase the acceptance by PCB manufacturers. The development of this wet-chemical, selective metal-plating process is described in Chapter 6 in more detail.

Now, having the micro-mirrors available on the lower cladding, the waveguides themselves are fabricated using the polymer waveguide technology described in Chapter 2.3. This results in a self-contained optical layer which has waveguides and micro-mirrors already integrated. Multilayer waveguide stacks can be accomplished by either stacking individual waveguide layers or by processing a next waveguide layer on top of the previous one according to [14].

5.5 Design

The design can be described as embedded micro-mirrors using an approach where the mirror is placed prior to the waveguide core fabrication. Thereby, the mirrors are created directly onto the lower cladding, prior to the waveguide core fabrication. This leads to an in-plane mirror design as shown in Figure 5.1 (*left*). Common arrangements will feature corners with an approximately 90° in-plane turn of the optical path.

An out-of-plane micro-mirror is shown in Figure 5.1 (*right*), where the waveguide is coupled to a vertical light path. The mirror consists of a structure with two surfaces tilted by 45° with respect to the vertical axis. A waveguide is then connected with one of the tilted mirror surfaces. Depending on the surface orientation, the light of the waveguide is either redirected in the positive or negative vertical direction, which leads to upward and downward pointing out-of-plane mirrors, respectively.

5 Concept of embedded micro-mirrors

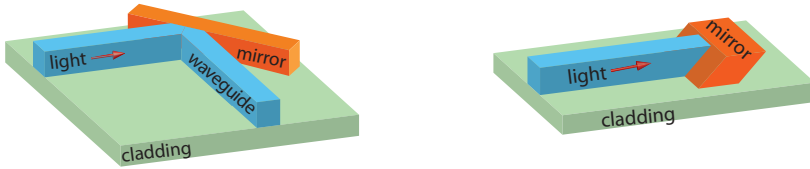


Figure 5.1: 3D schematic of an in-plane mirror with two waveguides intersecting under an 90° angle on the mirror surface (*left*), and of an out-of-plane mirror with a waveguide connected to the 45° tilted mirror surface (*right*).

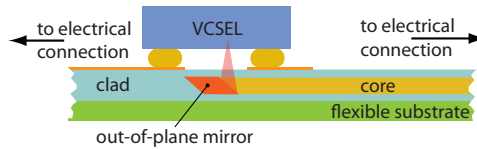


Figure 5.2: Cross-section illustration of an out-of-plane mirror vertically coupling to an optoelectronic element mounted directly thereon.

This arrangement is in particular - of interest to couple waveguides with a vertical optical path to an optical element, e.g., an optoelectronic element or an optical connector, see Figure 5.2.

In another embodiment, shown in Figure 5.3, two out-of-plane mirrors, one upward and one downward pointing, are arranged to form a vertical optical via. Thereby, waveguides from different optical layers can be interconnected. The thickness of the top cladding has an effect on the occurring losses, because the vertical propagation distance without guiding directly correlates to it. The shorter the vertical separation of the mirrors is, the lower is the occurring loss. The minimum cladding thickness between the two mirrors is limited by the deposition technique. A laterally variable top-cladding thickness, eventually facilitated by ink-jet printing, provides the connector-specific vertical pitch in desired locations, while the minimal-vertical pitch is realized in other locations.

The fact that the micro-mirrors are the same size as the waveguide cores, see Figure 5.1, provides ease of integration into the existing waveguide fabrication. An aspect which influences the metal-deposition process-development is that the lower optical cladding will be exposed to the fabrication process. Thereby, it is indispensable that the optical-grade surface of the cladding remains in good order.

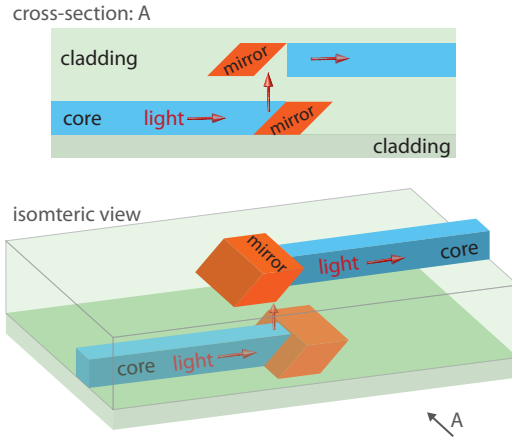


Figure 5.3: Isometric and cross-sectional illustration of two out-of-plane mirrors arranged to form a vertical optical via to interconnect two different optical layers.

5.5.1 Layout density considerations

A very common waveguide pitch used for optical interconnects is $250\ \mu\text{m}$, adopted from the quasi-standard for multimode optical fiber bundles. By applying a $100\ \mu\text{m}$ pitch, the linear density of a one dimensional waveguide array can be more than doubled, without major fabrication issues. In addition, by restricting the waveguide cross-sectional dimension to about $35\ \mu\text{m} \times 35\ \mu\text{m}$, one can also apply the very tight $62.5\ \mu\text{m}$ wide quarter-pitch [22, 95, 18]. This results in an aspect-ratio of 1.3 between gap width and waveguide height, and a minimum ratio between pitch p and waveguide width w of $p/w = 1.8$.

The eventually applicable density will be limited by the micro-mirrors. One parameter is the minimum length of a mirror-body required to provide a flat mirror surface in the region where it intersects with the waveguide. The intended on-the-fly approach to fabricate the micro-structures deploys a switching of the laser beam intensity while the laser head is moving over the substrate. Therefore, one has to allow some extra length for the micro-mirror to compensate for the areas where the laser is switched on and off. Let us assume a margin of one times the micro-mirror depth on each side of the waveguide. The depth of the structure is similar to the waveguide width. This leads to a pitch to waveguide width ratio of $p/w \approx 3$ and a resulting pitch of approximately $125\ \mu\text{m}$ for the targeted waveguide width of $42\ \mu\text{m}$. This, compared to a minimal pitch of $75\ \mu\text{m}$ required for $42\ \mu\text{m}$ waveguide cores. However, one has to keep in mind that this increase of the pitch is only required in the area where micro-mirrors occur. The increased area demand can be limited to specific locations by using a variable pitch. Thereby, waveguide bundles can be routed very space efficient with minimum pitch in areas without mirrors.

5.6 Reflectivity of metal layers

TIR mirrors are in the ideal case perfectly reflecting without any loss, thus providing a reflectivity of $R = 1$. Furthermore, efficient reflectors can be realized by thin-film Bragg-mirrors, which however are very demanding in fabrication and thus not applicable for this purpose. Metal reflectors are always subject to absorption. The reflectivity of a metal, assuming a perfect surface, depends on the type of metal, the incident wavelength, and the incident angle.

The incident angle for this application is mainly 45° . Exemplarily for gold, the difference in reflectivity for unpolarized light between perpendicular and 45° incidence is with 1‰ negligible.

The wavelength regime utilized in the herein described optical interconnect approaches is limited to 850 nm. Only a few metals exhibit acceptable reflectivity at this wavelength. These are aluminum, copper, gold, lithium, and silver which exhibit a reflectivity of 0.87, 0.97, 0.98, 0.93, and 0.98, respectively. Among these metals, gold certainly provides superior chemical properties. In particular the inert chemical behavior of gold and the wide range of industrial deposition processes available for gold surface layers are crucial factors. Moreover, gold is already an indispensable coating material in the PCB industry.

5.7 Summary

Herein described is the concept for area-efficient and fabrication-efficient micro-mirrors for in-plane and out-of-plane routing of polymer optical waveguides. An integral fabrication approach is being contemplated, whereby the micro-mirrors are fabricated directly on the lower optical cladding. Further advantages are the compatibility to existing polymer waveguide fabrication and established PCB manufacturing as well as the inherently provided scalability to large-size PCB substrates.

6 Reflective metal layer by selective chemical plating ¹

This chapter is focused on the development of a plating process for a reflective metal layer. This layer will be deposited onto the previously described micro-structure in order to complete the micro-mirror fabrication. The basic concept is to selectively activate the surface of the micro-structure, whereon then the reflective metal layer is deposited in an electroless plating bath. The main tasks described herein are: the development of the acryl-monomer based material, the selective activation of the free acrylic groups on the surface by aminolysis, the complexing of a palladium catalyst onto the reactive amine group, and the electroless deposition of the nickel-phosphor and gold layer. Large-size benchmark mirrors fabricated with this process achieve a reflectivity of $R = 0.86$, which corresponds to 89 % of the maximum reflectivity of gold.

¹Part of this work has been published in [59]

6.1 Introduction

The key aspects of the herein proposed wet-chemical metal deposition process are the selectivity and the capability to deposit metal on electrically isolated structures. Thereby, selectivity implies that only a specific material will be metalized, but not other materials surrounding the specific material. This is achieved by making use of the different chemical properties of the materials. Only one of them is susceptible to the activation process, while the others remain in the original state. Therefore, no additional lithographic masking layer is required. In the herein proposed approach, the micro-structure, which acts as body of the mirrors, shall be made out of the activatable material.

Cost-efficiency is crucial for the commercialization of polymer waveguide based optical interconnect approaches. This can be achieved by making use of fabrication processes, which are either standard for, or which can easily be implemented by the PCB manufacturer. For this reason, we restrict ourselves to wet-chemical processes, which are daily business for PCB manufacturers. Another advantage is that the required equipment is less costly than vacuum based deposition tools. This is advantageous in order to lower the entrance barrier for future manufacturers.

By evaluating wet-chemical metal deposition processes, with respect to the applied restrictions, electroless plating turns out as a viable solution. Fortunately, these kind of processes are very common in the printed circuit board industry [48, 74, 93]. An additional advantage of these electroless plating processes is their capability to uniformly coat irregular surfaces [102].

6.2 Approach

The approach towards an applicable process is based on the requirements previously set in Chapter 5, and is listed in the following.

- i Reflective metal layer, whose process is compatible with large-area substrate fabrication, cost-efficient, and compatible to PCB manufacturing. Therefore, equipment intensive and costly processes such as sputtering are inapplicable.
 - ▷ Plating process
- ii Isolated micro-structures, placed on the lower cladding, need to be plated. Thus, electro-plating cannot be used.
 - ▷ Autocatalytic (electroless) metal plating process
- iii Electroless plating processes require a catalyst which is bound to the surface. Plating will only occur on areas covered by the catalyst.
 - ▷ Palladium, a very common catalyst, can be complexed to reactive amine groups.

- iv The required selectivity implies that only the micro-mirror body, and not the surrounding cladding, is covered by amine groups.
 - ▷ Ethylenediamine, a linear molecule with an amine group at each end, can be selectively attached to dangling acrylic groups.
- v Micro-structures with vertical and inclined faces, which can be fabricated with waveguide fabrication tools, are required. In addition, they should provide free acrylic groups on the surface.
 - ▷ UV-curable acrylic resin, which can be structured by laser direct-writing. By using monomers with high functionality, e.g. number of acrylic groups in a molecule, dangling acrylic groups remain on the surface.

6.3 Process Description

The following description of the individual process steps is illustrated in Figure 6.1.

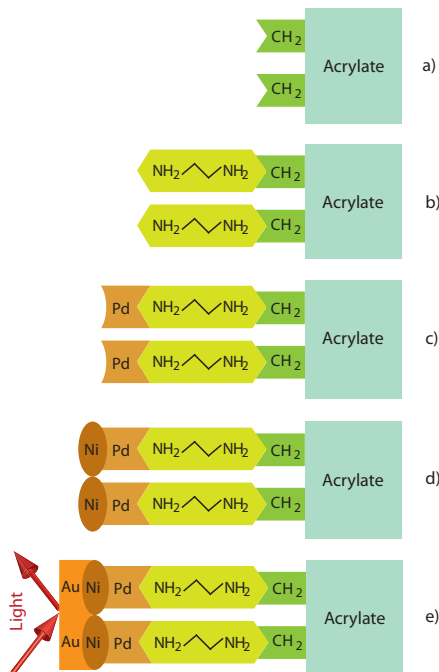


Figure 6.1: Diagram of selective metal deposition process steps: a) acrylate structure, b) selective surface activation, c) selective catalyst deposition, d) electroless nickel deposition, and e) immersion gold process.

6.3.1 Polymer cladding material

The micro-mirrors are fabricated directly on top of the lower optical cladding. Therefore, the cladding material must meet the following requirements: a) It has to withstand the chemicals used. In particular, the optical properties of the cladding material must not be altered; b) The cladding material must provide good adhesion for the micro structures; c) It has to be compatible with the waveguide polymer material used, e.g., in terms of optical and chemical properties.

6.3.2 Photosensitive acryl-monomer resin

A straight forward way to fabricate micro-structures is to use a photosensitive material [67, 72]. A custom blend of acryl monomers and additives is used to obtain a photocurable acryl resin. This choice is based on the intended selective deposition process which uses functionalization of free acryl groups on the surface.

The following requirements apply for the cured acrylate polymer: a) provision of free acryl groups on the surface; b) curability with UV sources common for polymer waveguide fabrication, i.e., UVA flood exposure lamp or a laser source $\lambda = 355$ nm; c) capability to form micro-structures with vertical dimensions similar to the cross-sectional size of the multimode waveguide cores (35 - 50 μm); d) provision of appropriate adhesion to the underlying cladding polymer; and e) the resulting surface of the cured micro-structures shall provide optical grade roughness.

The acryl monomer blend described in Table 6.1 is used for the fabrication of the micro-mirrors in Chapter 7. A basic formulation for a UV-curable acrylic resin was obtained from the supplier (SARTOMER). The final resin recipe, as listed herein, is the result of a series of experiments. Mixtures of various acryl monomers with different photoinitiators and additives were blended in-house. Micro-structures and thin layers with each mixture were fabricated. These samples were then tested and optimized according to the aforementioned requirements a) - e).

Acryl monomers

Acryl monomers are classified by their functionality and by the type of their chemical backbone. Thereby, the functionality describes the number of acrylate groups present on the monomer. Therefore, mono-, di-, and tri-functional acrylate monomers contain 1, 2, or 3 functional acrylate groups, respectively. The functionality influences the degree of crosslinking in the final polymer and thus also the shrinking. For the intended application, higher degree of functionality is expected to lead to more free acrylic groups on the surface of the cured polymer. Experiments reveal that acryl-monomer blends with high content of the trifunctional SR368D (all monomers obtained from SARTOMER) monomer yielded very efficient metal plating.

Important properties such as curing shrink, flexibility, and adhesion are influenced by the type of backbone. SR833S, a difunctional acryl monomer, is used to improve adhesion and flexibility of the crosslinked material. The diacrylate SR238B (difunctional) is a low viscose monomer which provides fast curing, good adhesion

Table 6.1: Composition of the photosensitive acryl monomer resin.

Monomer/Additive	Functionality of monomer	Amount [wt%]
SR368D	3	45.2
SR833S	2	21.7
SR238B	2	12.0
SR531	1	7.3
CN704		9.0
2-Hydroxy-2-methylpropiophenone		4.8

and good chemical resistance. Finally, SR531, a monofunctional monomer, is added to improve adhesion and flexibility and provide low curing-shrink.

Photoinitiator

Liquid 2-hydroxy-2-methylpropiophenone (SIGMA-ALDRICH) has been chosen over the powdery TPO (Lucirin[®] from BASF). Both photoinitiators are suitable for UV-curing in the intended wavelength range. Finally, the decisive factor was the simpler processability of the former one. The photoinitiator generates free radicals by means of UV-photon absorption, which then initiate the photopolymerization of the monomers. In general the direct free radical polymerization yields a simple process, whereby only the curing and one development step are required, without the need for intermediate baking steps. However, the occurring oxygen inhibition can be a drawback [101]. The inhibition takes place when oxygen acts as a comonomer and forms a less active peroxy radical. This can result in incomplete surface curing or an undercuring of the layer. In particular thin layers are affected, because oxygen can diffuse through the complete layer, resulting in an uncured layer. Curing in an inert-gas atmosphere and oxygen scavengers are two solutions to overcome this issue. Therefore, thin layers below 1 μm thickness were cured in a nitrogen curing chamber.

An amount of 4.8 wt% of the hydroxyphenylketone photoinitiator has been found to provide suitable curing of micro-structures, either by UV-laser or UV-lamp exposure.

Additives

An acrylated polyester based adhesion promoter, CN704 (SARTOMER), is added to further increase the adhesion.

6.3.3 Selective surface functionalization by aminolysis

The key aspect of the herein proposed metal deposition process is the selectivity. Various functionalization approaches for a variety of applications can be found, such as biochemistry [78], nanotechnology [40, 90], and microfluidics [38]. Among these approaches, several make use of amine groups as a reactive species [29, 38, 78, 100].

6 Reflective metal layer by selective chemical plating

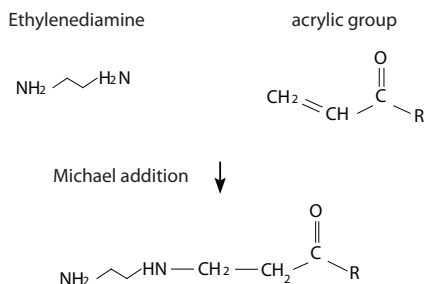


Figure 6.2: Michael addition of ethylenediamine to an acrylic group.

Dissolved ethylenediamine (EDA, SIGMA-ALDRICH) has been identified as suitable solution to selectively functionalize the surface of the aforementioned acryl. The EDA contains two primary amine groups NH_2 , one on each end of the molecule. One of these amine groups can bind to the unreacted acrylic groups on our acrylate microstructure by the highly selective Michael's addition [29, 96], see Figure 6.2. The presence of EDA on the acrylate surface is verified by XPS measurements which identify the N-H bond specific binding energies, see Figure 6.3 (*left*).

Michael addition

The Michael addition [29, 96] describes the addition of an amine group to an unsaturated carbonyl compound, in this case the acrylic group, see Figure 6.2. Due to the fact that the PSSQ and the PU cladding, the surrounding materials, do not exhibit unsaturated carbonyl compounds, they are not affected by the process. Thus, having structures with reactive acrylic groups placed on an inert cladding leads to a selective functionalization of the former. Experiments confirm that the PSSQ and the PU cladding are, indeed, not susceptible to the conjugate addition of amine groups.

It has been verified experimentally that ethanol (SIGMA-ALDRICH) is an efficient solvent for EDA to realize the Michael addition of the amine group to the acrylic group. However, having the samples immersed into this solution for up to sixty minutes leads to severe damage of the PU cladding. By using the less strong solvent hexanol (SIGMA-ALDRICH), the EDA is still efficiently dissolved and the amine successfully added to the acrylic group, while the cladding is not visibly affected.

Reactive surface amine group

The remaining amine group of the EDA now acts as reactive amine group on the acrylate surface and, therefore, provides the desired surface functionalization.

6.3.4 Selective catalyst deposition

A catalyst is required to eventually initiate an autocatalytic metal plating process. This is conventionally achieved by colloidal deposition on a previously etched surface. A more sophisticated approach is to chemically bind catalyst atoms to

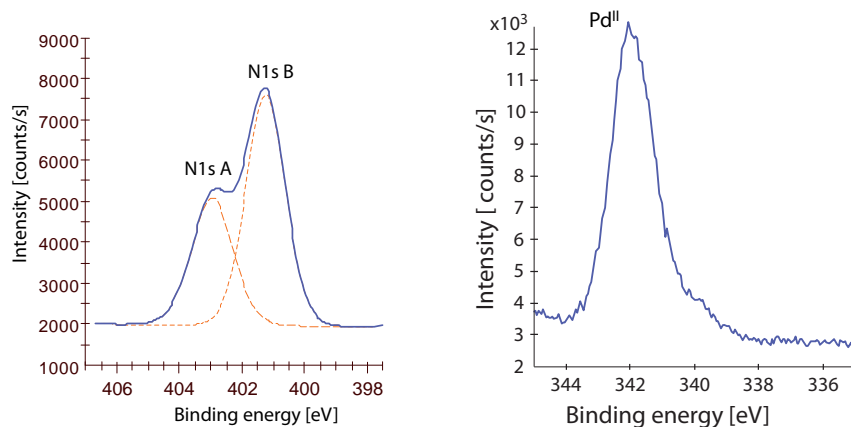


Figure 6.3: XPS spectra unveiling the amine groups, by the N-H bond specific energies, which are attached on the surface of the acryl layer (*left*), and exhibiting a binding energy peak at 342.0 eV, which can be attributed to Pd^{II} complexes (*right*).

active surface groups [6, 46, 47, 114]. This can be done by covalent bonding of Pd^{II} complexes to the reactive amine group. Coordination chemistry describes the formation of such compounds between a metal ion and a negatively charged molecule. This process is very selective to specific materials, therefore providing the desired selectivity for the catalyst deposition. In addition, a covalent bond provides a strong metal-polymer interface. The process is herein performed by immersing the substrates into an aqueous Pd-solution. It is made up from sodium-tetrachloropalladate (Na_2PdCl_4 , SIGMA-ALDRICH), which provides the palladium ions, dissolved in DI- H_2O (deionized water). Morpholineethanesulfonic acid (MES, SIGMA-ALDRICH) and sodium chloride (NaCl) are added to adjust the pH value to 4.9 and to increase the sodium ion concentration, respectively, thereby, influencing the shelf-life and Pd-deposition efficiency of the solution [24].

The XPS measurement of a thin acryl layer which has undergone the aminolysis treatment and been immersed into the aqueous sodium-tetrachloropalladate solution, as shown in Figure 6.3 (*right*), exhibits Pd^{II} complexed to the surface amine group.

6.3.5 Electroless nickel deposition

The covalently bonded palladium complex, which is present on the surface, acts now as catalyst to initiate the autocatalytic nickel plating process. This electroless process is performed in an acidic solution containing nickel salt and various additives. Such processes are widely used in the printed circuit board and surface finishing industry [48, 74, 93]. This process enables a good surface quality and a uniform layer growth is achieved.

Among the commercially available nickel plating solutions for a high-bright

finish, Melplate 865M (ENTHONE) is favorable for the work herein, mainly due to a lower process temperature range of 82 - 90 °C. This helps to reduce the thermal impact on the cladding and the acrylate polymer. The samples herein were plated at temperatures as low as 72 - 76 °C. As is common for bright electroless nickel layers, the final phosphorous content range is 4 - 6 %.

The plating bath is diluted by 3:1 (75 % of the original formulation) and adjusted to 4.8 pH by adding sulfuric acid (4 M H₂SO₄) or ammonia hydroxide (3 M NH₄OH) to the heated solution. Plating durations of 2 - 3 min in combination with deposition rates of approximately 0.2 μm/min yield nickel-phosphorous layers of 0.5 μm thickness.

6.3.6 Immersion gold process

The immersion gold process is a chemical deposition of a thin gold layer onto a metallic base material. It is an electroless process and thus no external electrical potential is required. Once the substrate is immersed into the heated immersion gold bath, surface metal atoms, nickel atoms in the herein described case, are substituted with gold atoms. Generally, such a process requires the substrate metal to be less noble, i.e., having a lower electronegativity, than the precious metal to be deposited. The growth rate follows an exponential decay due to the dependency on the nickel-atom diffusion through the growing gold layer into the gold bath. Thus, the gold layer thickness is limited to about 100 nm [27]. An advantage is the conformal layer deposition onto complex three-dimensional structures. Therefore, it is ideally suitable for the herein presented micro-structures. Due to the conformal behavior, the achievable surface smoothness, and thus the optical quality, strongly depends on the topography of the underlying nickel layer.

Two different types of immersion gold processes were deployed. A first type is prepared by adding 588 mg KAu(CN)₂ (potassium dicyanoaurate; SIGMA-ALDRICH) and DI-H₂O to 20 mL of the commercially available Immersion Gold I (ENTHONE) makeup solution, this according to the suppliers specifications. The other type is the commercially available ready-to-use solution Instagold Flash (GOLDTOUCH INC.). The former bears the potential advantage of a lower processing temperature of 70 °C, compared to 85 °C of the latter, whereas the latter avoids handling of the very toxic (T⁺) potassium dicyanoaurate salt and, given the low gold salt concentration, provides economical advantages. The standard processing time for both solutions is in the range of 3 - 5 min. A potential nickel oxide layer is removed by a preceding dip into a 5 % HCl solution. This ensures that the process is instantaneously initiated across the nickel surface.

The required gold layer thickness can be calculated using the optical properties of gold. Thereby, the minimum gold thickness in order to achieve a transmission of less than 1 %, is 55 nm (absorption coefficient $\alpha_{850nm} = 83 \mu\text{m}^{-1}$ [88]). Based on an expected deposition thickness of 100 nm after 12 min plating [27] and by considering an exponential decrease of the plating rate due to its diffusion limited characteristic,

one can assume that a plating duration of 4 min will be sufficient to deposit the targeted minimum thickness of 55 nm.

6.4 Characterization

The property of interest for the deposited metal layer is the optical reflectivity. Influencing parameters are the chemical composition of the top metal layer and the surface morphology of the layer. These parameters are characterized herein by means of benchmark mirrors as specimen.

6.4.1 Benchmark mirrors as characterization specimen

The benchmark mirrors, used to develop the selective metal plating process, are based on a silicon substrate. The native silicon-oxide of the substrate is removed to improve the adhesion thereon. An approximately 0.5 μm thick acrylate resin layer is then spin coated onto the substrate. A temperature step is required to remove the solvent of the diluted acrylate resin prior to the UV flood exposure under nitrogen ambience.

This planar, acrylate-coated substrates are then processed according to Sections 6.3.3 to 6.3.6. After the final process step, the immersion gold deposition, the benchmark mirrors are ready for characterization.

6.4.2 Optical characterization equipment

In the following, the optical tools used to characterize the reflectivity of the metal layers in this chapter and in Chapter 7, are explained.

6.4.2.1 Microspectrophotometer

The versatile microspectrophotometer (J&M) is herein used in the reflectance mode only. This, in order to obtain the spectral reflectivity of the corresponding mirror sample. The region of interest can be set by selecting the appropriate microscope lens magnification and adjusting the rectangular-shaped aperture. The light source is set to the desired wavelength of 700 nm with $FWHM = 19$ nm (full width half maximum). Unfortunately, the available equipment cannot be operated at 850 nm due to detector limitations. However, the difference in reflectivity of a gold layer between these two wavelengths is $\Delta R = 0.014$ ($R_{Au700nm} = 0.962$ and $R_{Au850nm} = 0.976$) or approximately 1.4 %. Thus, one can extrapolate the measured reflectivity to the desired wavelength of 850 nm without introducing relevant errors. This is feasible, because the effect of the surface roughness on reflectivity changes is negligible over this small wavelength range of 700-850 nm. All measurements are performed relative to a reference mirror, a commercially available gold mirror $R_{Ref700nm} = 0.96$ (THORLABS).

6 Reflective metal layer by selective chemical plating

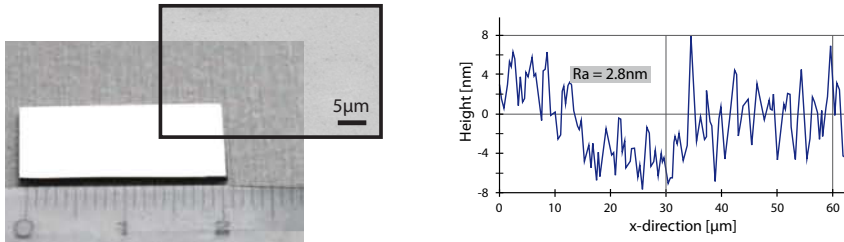


Figure 6.4: Photograph of a benchmark mirror ($20 \times 10 \text{ mm}^2$) with electron micrograph detail of the surface (*left*), and the surface profile, measured by the white light interferometer (*right*), exhibiting a roughness $R_a = 3 \text{ nm}$.

6.4.2.2 Spectrophotometer

A UV-VIS-IR spectrophotometer (PERKINELMER), with a wavelength range of 200-2000 nm, is used in reflectance mode to characterize the large-area benchmark mirrors. The applicability for tiny mirrors is limited by the spot size of about 5 mm and the minimum mechanical size of the sample of 20 mm.

6.4.2.3 Free-space reflectivity setup

Additionally, an optical setup based on a 850 nm wavelength laser source has been built. Thereby, the end facet of a single mode fiber is magnified and imaged onto the surface of the micro-mirror under investigation, resulting in a spot size thereon of $20 \mu\text{m}$. The laser beam hits the micro-mirror preferentially under an incident angle of 45° . Thereafter, the part of the reflected light which fulfills the *N.A.* restrictions of the collecting lens, is guided towards the optical power detector and hence measured. Determination of the reflectivity is carried out by comparing the measurement values with the reflected optical power of a reference mirror.

6.4.3 Benchmark mirror measurements

The benchmark mirrors are based on a silicon substrate, whose native oxide has been stripped previously, whereon an approximately $0.5 \mu\text{m}$ thick layer of the acrylic monomer resin is deposited and UV cured. The reflective metal layer is then plated as described earlier in Section 6.3. Figure 6.4 (*left*) shows a photograph with an interferometer scan (*right*) of a completed benchmark mirror. It exhibits a gold surface roughness $R_a = 3 \text{ nm}$, measured over a scan range of $60 \mu\text{m}$, a value well below the $\lambda/20$ -criteria required for optical grade surfaces.

Layer conformity and nano-scale roughness

The surface topography of the nickel layer itself and of the gold layer plated thereon is measured with an AFM, shown in Figure 6.5 (*top*). Therewith, the surface quality of the layers and the degree of conformity of the gold layer is investigated. The

images generated from the AFM measurements reveal an increased roughness of the gold layer in the nano-scale regime. Clearly visible is the finer granularity in the surface image of the gold layer (*top right*). To quantify this observation, the power spectral densities calculated from the AFM measurements are compared in Figure 6.5 (*bottom*). This allows us to determine an increase in roughness for features with a spatial frequency above $30 \mu\text{m}^{-1}$. Features in the nickel layer with a lateral size larger than 35 nm are conformally mapped by the overlying gold layer. Light scattering is sensitive to roughness with a spectral frequency below $5 \mu\text{m}^{-1}$ for a wavelength of $\lambda = 850 \text{ nm}$, which relates to a lateral resolution of $\lambda/4$. Thus, no derogation of the optical reflectivity of the gold surface due to this nano-scale roughness is expected.

Surface impurities

XPS measurements are used to identify impurities on the gold surface, whereby the sampling depth is limited to a few nanometers. The measurements reveal nickel and phosphor atoms on the gold layer, which potentially could impede the reflectivity.

Future process optimization would require the following: extensive XPS measurements to quantify the amount of impurities, investigations towards the correlation between the amount of impurities and the optical reflectivity, and a process to reduce the impurities.

Reflectivity

Figure 6.6 shows the reflectivity of $R_{Ni} = 0.6$ and $R_{Au} = 0.86$, for the nickel and gold layers, respectively. The metallic layers are fabricated according to Sections 6.3.5 and 6.3.6, deploying the Instagold Touch (GOLDTOUCH INC.) bath for the gold layer. They are measured at a wavelength of $\lambda = 700 \text{ nm}$ and compared to the expected reflectivity [88] of polished nickel and gold. The measured layers achieve as much as 89 % of their maximum material-specific reflectivity. The arrows in the graph point to the expected reflectivity values for 850 nm wavelength, extrapolated from the measurement at 700 nm and the known wavelength dependency of the reflectivity for the respective metal.

6.5 Summary

A material-selective surface activation, in combination with an electroless metal plating process, has been developed. The custom acrylate resin formulation provides photosensitivity for UV-patterning and the desired surface chemistry, free acryl groups, for the selective activation. The acryl monomers are commercially available and are mixed with a photoinitiator and additives accordingly to obtain a good plating efficiency, better adhesion, and low curing-shrinkage. The aminolysis is selective to free acryl groups and provides reactive amino groups on the surface of the cured resin. These reactive species are then used to complex palladium thereon, which yields an efficient catalyst for the subsequent electroless nickel-phosphour

6 Reflective metal layer by selective chemical plating

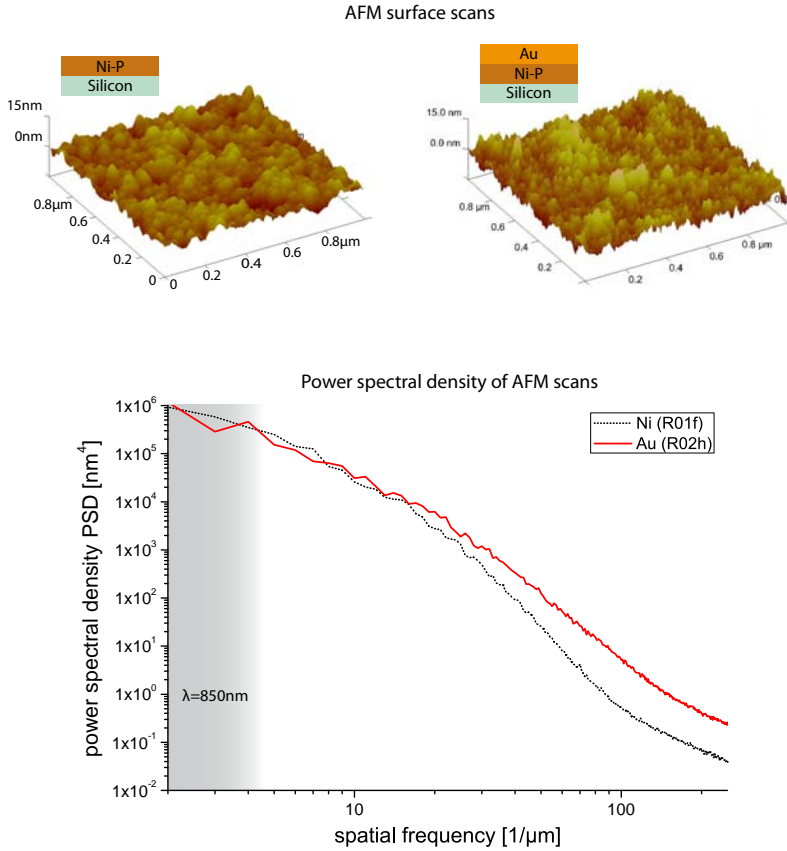


Figure 6.5: AFM topographical image showing the nickel layer only (*top left*) and the added gold layer (Immersion Gold I) (*top right*) of a benchmark mirror with a surface roughness of $R_{a(\text{Ni})} = 1.5 \text{ nm}$ and $R_{a(\text{Au})} = 1.75 \text{ nm}$, and a reflectivity $R_{\text{Ni}} = 0.5$ and $R_{\text{Au}} = 0.4$, respectively. The power spectral density (PSD) (*bottom*) calculated from the above AFM measurements reveals a difference between both layers in the nano-scale roughness, whereby the gold layer exhibits an increased amplitude for features with a spatial frequency above $30 \mu\text{m}^{-1}$, which correlates to a feature size smaller than 35 nm . The grayish area on the left indicates the spatial frequency to which scattering measurements of light (850 nm) are sensitive.

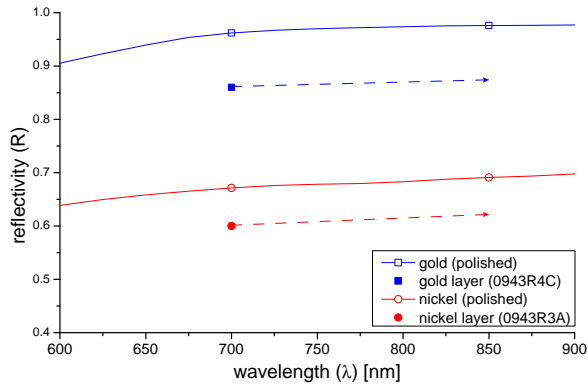


Figure 6.6: Reflectivity of wet-chemically deposited nickel and gold layers measured using the microspectrophotometer and the expected reflectivity of polished nickel and gold [88] as comparison.

plating. The final immersion gold layer allows for an increase in reflectivity in the desired wavelength range of $\lambda = 850 \text{ nm}$. The electroless plated layers, nickel-phosphor and gold, exhibit a good conformal mapping of the substrate topography and yield very smooth surfaces with roughness values of $R_a < 2 \text{ nm}$. The immersion gold layer processed on large-size benchmark mirrors achieves a reflectivity of $R = 0.86$, which corresponds to 89% of the maximum reflectivity of gold.

7 Fabrication and characterization of embedded micro-mirrors

This chapter is concerned with the manufacturing of the embedded micro-mirrors proposed in Chapter 5, using the selective metal plating process developed previously in Chapter 6. The fabrication processes required to build the waveguide layer with the embedded micro-mirrors are described in Section 7.1 and 7.2. The resulting micro-mirrors are analyzed in Section 7.4 and are optically characterized in Sections 7.5 and 7.6. The final section of this chapter explores an electro-optical flex board with integrated out-of-plane micro-mirrors as basis for a compact parallel optical module. The integration scheme is discussed and the fabricated waveguide layer with vertical light-coupling based on micro-mirrors is presented.

7.1 Fabrication of the optical layer stack

The fabrication sequence for waveguides and micro-mirrors embedded in the optical layer stack is as follows.

- Substrate preparation
- Lower cladding deposition
- Micro-structures fabrication based on acrylic monomer (Chapter 5)
- Reflective layer deposition onto micro-structures (Chapter 6)
- Waveguide core fabrication
- Upper cladding deposition

7.1.1 Substrate

For the herein proposed approach, any substrate compatible to conventional polymer waveguide fabrication is applicable [15]. For our experiments, we preferably use a resin-polyimide-resin sheet, with a thickness between 100 μm and 120 μm , as flexible substrate. For some experiments also FR4 boards or glass sheets are used as rigid substrates.

7.1.2 Lower cladding

The lower cladding has, compared to the standard waveguide fabrication process (Section 2.3), to provide important additional features. It needs to provide sufficient adhesion for the acrylate-based micro-mirrors and it has also to withstand the chemistry used for the selective metal-plating. Thus, various claddings based on three different material types are investigated.

Polyurethane cladding

Two different kinds of polyurethane claddings are used herein. PU1 is the cladding normally used in the base technology for planar polymer waveguides, described in Section 2.3. The PU2 cladding, from the same supplier is employed in this work, mainly due to its superior chemical resistance.

The liquid PU-cladding, which contains no solvents, is applied by doctorblading onto the substrate. A smooth movement of the blade, provided by a translation stage at a constant feed of 4 mm/s , ensures a smooth surface. After the deposition, the substrate remains on the vacuum chuck for the subsequent 15 min i-line ($\lambda = 365 \text{ nm}$) UV-exposure (LOT ORIEL, $P = 25 \text{ mW/cm}^2$). Thereafter, the cladding undergoes a thermal treatment at 80 $^{\circ}\text{C}$ for up to 180 min.

PSSQ cladding

The PSSQ cladding (polysilsesquioxane) is under development as highly reliable optical material for the base technology, described in Section 2.3. It provides an excellent chemical resistance and thermal reliability.

The liquid PSSQ cladding is also applied by doctorblading. A 10 min soft-bake at 90 °C in an oven is required to evaporate the remaining solvent. The i-line UV exposure takes time for 20 min. Thereby, the photo acid generator (PAG) in the polymer absorbs the photon energy and generates the acid catalyst, required to catalyze the polymer condensation. The post-exposure bake (90 °C [1]) and the hard bake (145 °C [1]) are used to provide the diffusion of the acid and for the curing of the silsesquioxanes, respectively [1].

Alternative cladding

Commercially available epoxy-based optical materials, which provide an applicable refractive index, are also considered as lower cladding. The doctorbladed epoxy layer is thermally cured in an oven.

7.1.3 Acrylic monomer based micro-structures

7.1.3.1 Acrylic monomer layer

The acrylic monomer, described in Section 6.3.2, is deposited by doctor blading onto a lower cladding layer. A doctor blade distributes the liquid monomer to a layer with a controlled thickness and a smooth surface. The desired layer thickness depends on the waveguide core thickness, because the final mirror thickness should be equal to, or slightly higher than, that of the waveguide.

7.1.3.2 Laser-direct-writing of micro-structures

The micro-mirrors are patterned by exposing the acrylic monomer with a UV-laser spot. The laser-head, which contains the optics to form the laser spot, is mounted on the three-axis linear robot system, described in Section 2.3. A newly deployed diode-pumped, mode-locked, frequency-tripled Nd:YAG-laser (PALADIN from COHERENT) which provides a quasi-CW (quasi continuous wave) beam at $\lambda = 355$ nm, is used as the UV source. The free space beam passes through an acousto-optic modulator (AOM) into a high-power beam dump. The sound waves in the modulator are used to diffract the required fraction of the output power ($P_{opt} = 2$ W) and to couple it into a fiber. The intensity of the sound wave correlates with the optical power of the diffracted light, i.e., the power in the first order diffraction. The fiber, which provides singlemode operation in the near ultra-violet region (STOCKER YALE), is then routed to the laser head.

Vertical laser head for in-plane mirrors

A vertical laser head, Figure 7.1 (*left*), is mounted to expose micro-structures with vertical sidewalls as basis for in-plane mirrors.

The divergent laser beam from the fiber endfacet is collimated with a first lens and then directed towards an aperture as convergent beam using another lens, whereby the pinhole aperture is placed slightly out of focus. The beam diameter at the pinhole position is about twice the pinhole diameter. Therefore, the aperture partially masks

the gaussian-like beam and provides an intensity profile with steep edges. The pinhole is imaged with a magnification of $m = -1/3$ onto the polymer layer by using a biconvex lens.

Accurate positioning of the micro-mirrors is obtained by precisely referencing the laser spot with respect to the laser-writer camera. This is done in all three dimensions with a precision better than $1\ \mu\text{m}$. For this, a $\varnothing 5\ \mu\text{m}$ precision pinhole is mounted on an stationary optical power meter. The camera is then aligned to the pinhole, and subsequently the laser spot is aligned to the pinhole as well. Therefore, the laser beam is moved over the stationary pinhole to obtain the intensity profile of the beam. Figure 7.2 (*left*) shows the adjusted optical intensity profile of the laser spot. Varying the vertical position of the laser spot reveals that the depth of field, i.e., the range wherein the spot has an acceptable shape for laser writing, is larger than $\pm 40\ \mu\text{m}$.

Figure 7.3 shows cross-sections of micro-structures for in-plane mirrors exposed with the previously described laser system. This confirms that the imaging optic used is generating a spot with sufficient depth of field for laser-direct writing of structures with a height of up to $100\ \mu\text{m}$.

Tilted laser head for out-of-plane mirrors

In the case of out-of-plane mirrors, a tilted laser head is used to expose the required tilted shapes, see Figure 7.1 (*right*). The top part, from the fiber port to the aperture pinhole, remains identical for both, vertical- and tilted-type laser heads. An imaging system consisting of a first plan-convex lens with $f = 30\ \text{mm}$ and a second plan-convex lens with $f = 15\ \text{mm}$ is used to image the aperture onto the substrate with a magnification $m = -1/2$. The collimated beam between the two lenses is deflected by a mirror towards 45° direction with respect to the vertical axis. A prism is used to couple the 45° tilted beam efficiently into the photosensitive layer of the substrate. A liquid glycerin film is used to provide refractive index matching between prism and substrate. Immersion exposure is already used in semiconductor fabrication to increase the applicable numerical aperture (N.A.) of the photolithography tool. The alignment procedure of camera and laser spot is done by using two edges of a metal film on a glass substrate. The beam is moved sequentially over the two perpendicular edges to determine the center of the spot. A power meter with a $\lambda = 355\ \text{nm}$ wavelength laser-line filter is mounted under an angle of 45° below the glass substrate. Thereafter, the vertical direction is adjusted until the desired intensity profile of the spot is achieved, see Figure 7.2 (*right*). The shown intensity profile is basically the derivative of a line scan. Mainly measurement inaccuracies of the optical power meter lead to the strong perturbations in the calculated beam profile.

The resulting width of the structure for a specific photosensitive material depends, besides the laser-spot profile, strongly on the writing speed of the moving laser and the total optical power in the laser beam. Common process parameters for the acrylate structures are listed in Table 7.1. By applying the multipass writing procedure, the micro-structure is exposed m times, each time with $1/m$ of the totally required UV dose. The advantage is an improvement of the cross-sectional shape of

7.1 Fabrication of the optical layer stack

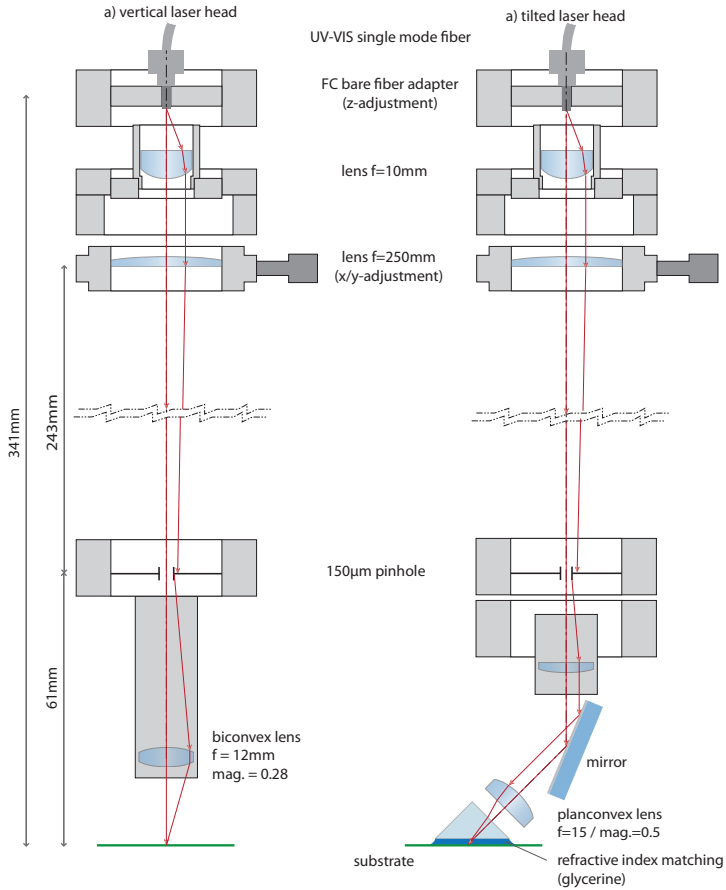


Figure 7.1: Schematic of the vertical laser head (*left*), and tilted laser head (*right*), only the part below the pinhole needs to be replaced to change between vertical- and tilted-type laser head.

Table 7.1: Laser direct writing process parameters for fabricating acrylate monomer based microstructures.

Parameter	Symbol	Value	Unit
Spot size FWHM	w_{spot}	53	μm
Optical power spot	P_{spot}	540	μW
Effective writing speed	v_{eff}	8	mm/s
Number of passes	m	4	
Spot speed ($v_{spot} = m \cdot v_{eff}$)	v_{spot}	32	mm/s

7 Fabrication and characterization of embedded micro-mirrors

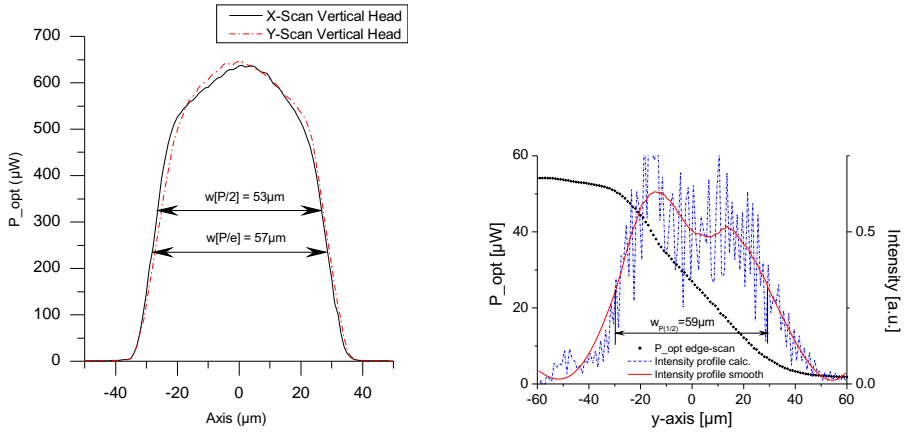


Figure 7.2: Optical intensity profile of the laser spot along x- and y-axis measured through a pinhole mounted on a stationary power meter (*left*), and measured edge-scan and the calculated intensity profile derived from it (*right*).



Figure 7.3: Cross-section micrographs of in-plane micro-mirrors on lower cladding, showing vertical sidewalls of over 120 µm in height, with only a small inclination on the bottom part of the structure (exposed by a laser-diode based vertical laser-head) (*left*), micro-structure with about 50 µm cross-sectional dimension (exposed using the frequency tripled Nd:YAG laser) (*right*).



Figure 7.4: Cross-section of tilted acrylate micro-structures on a polyimide substrate (*left*) and on a lower PU-cladding (*right*), both are patterned using the tilted laser-head. The acrylate structure on the lower cladding shows delamination (*right*).

the micro-structure, by reducing the effect of rounded shoulders.

The cross-section of a tilted acrylic micro-structure on a polyimide substrate is shown in Figure 7.4 (*left*). A laser-writing speed of $v_{eff} = 8 \text{ mm/s}$ and optical power of $P_{spot} = 500 \text{ } \mu\text{W}$ were applied for this structure. A similar structure, which is fabricated directly on a lower cladding, Figure 7.4 (*right*), exhibits delamination. This is an indicator for high stress within the acrylic structure and insufficient adhesion between acrylate and lower cladding.

7.1.3.3 Development of the acrylic polymer

A solvent-based development process removes all of the unexposed acrylate monomer, unveiling the cured body of the micro-mirror. Different solvents, such as dimethylformamid, propylenglykolmonomethylethylacetat PGMEA, and ethanol, can be used to dissolve the unexposed acrylate monomer. However, the weak chemical resistance of the lower cladding restricts the choice of the solvent. The surface quality of the lower cladding must not be degraded. Having solvents affecting the lower cladding would degrade the surface quality of the core-cladding interface and, thus, increase the propagation loss of the optical waveguide.

In case of the PU based lower cladding, the sample is agitated for 60 s in a cyclohexanol (SIGMA-ALDRICH) bath. Thereafter, a dip in an ethanol (SIGMA-ALDRICH) bath in combination with an ethanol rinse removes any residuals. In case of other, less critical substrates, the acrylic monomer can be removed by agitating the sample directly in an ethanol bath for 60 s with a subsequent ethanol rinse.

7.1.3.4 Surface quality of the micro-structures

The surface quality of the vertically oriented mirror surface of the in-plane micro-mirror patterned by vertical laser-direct writing, shown in Figure 7.5 (*top*), is comparable to the surface quality of waveguide core sidewalls. The quantitative characterization of the mirror surface in Section 7.5.1 reveals a surface roughness of $R_a = 20 \text{ nm}$ (50 μm scan range).

In contrast, the surface roughness of the 45° oriented mirror-surface of the out-of-plane micro-mirrors, shown in Figure 7.5 (*middle, bottom*), clearly exceeds the roughness of the in-plane micro-mirror, see Section 7.5.1. This difference can be explained by the deployment of the tilted laser head. A lens, a mirror, a prism, a glycerin layer, and a cover glass are in addition inserted into the optical path and potentially cause disturbances in the beam. Nevertheless, smooth tilted surfaces of micro-structures based on PSSQ core material have been achieved using the same tilted laser head, see Figure 7.11. Since the PSSQ material is solid during the UV exposure, there is no need to use a cover glass. Taking this into account, the potential source of the increased surface roughness is the cover glass. In particular, the anti-sticking layer on the bottom side of the cover glass seems to be critical. This layer is applied onto the cover glass from liquid phase (diluted fluoinert FC77 from 3M) or

7 Fabrication and characterization of embedded micro-mirrors

Table 7.2: Process steps and the respective process parameters for the selective deposition of the reflective metal layer.

Process step	Process detail	Temp.	Duration	Additional parameter
Surface functionalization	Ethylene-diamine in hexanol	20 °C	50 min	N ₂ ambience
Selective catalyst deposition	Aqueous Na ₂ PdCl ₄ solution	20 °C	12 min	pH 4.9
Electroless nickel plating	Nickel-phosphorous bath M865 (ENTHONE)	72 °C	80 s	Dilution 3:1
Immersion gold	Instagold (GOLD TOUCH)	86 °C	150 s	pre-cleaning 5%HCL

gas phase (C₄F₈). The layer is required to separate the cover glass from the liquid acrylic resin and, thus, enables the cured acrylic structures to be finally released.

7.1.3.5 Adhesion of the micro-structures on the lower cladding

The lower cladding layers made of PU1 or PU2 material provide good adhesion of the micro-structures thereon.

However, the PSSQ and epoxy based cladding layers provide only insufficient adhesion for the acrylate-based micro-structures. This effect occurs, despite the fact that the acryl monomer resin has been improved for adhesion by adding an adhesion promoter and acryl monomers, which provide low curing shrinkage and improved adhesion, see Section 6.3.2.

7.1.4 Selective deposition of reflective layer

7.1.4.1 Selective metal-plating of the micro-structures

The following processes are required to obtain the reflective metal coating: selective surface functionalization of the acrylic micro-structure, selective catalyst deposition thereon, electroless nickel deposition initiated by the catalyst, and immersion gold layer deposition onto the nickel, see Sections 6.3.3, 6.3.4, 6.3.5, and 6.3.6, respectively. The enabling step for the selective metal coating is the selectivity of the surface functionalization process. The other processes are intermediate steps required to facilitate the deposition of the desired gold layer, which provides the high reflectivity in the near-infrared (NIR) range.

7.1 Fabrication of the optical layer stack

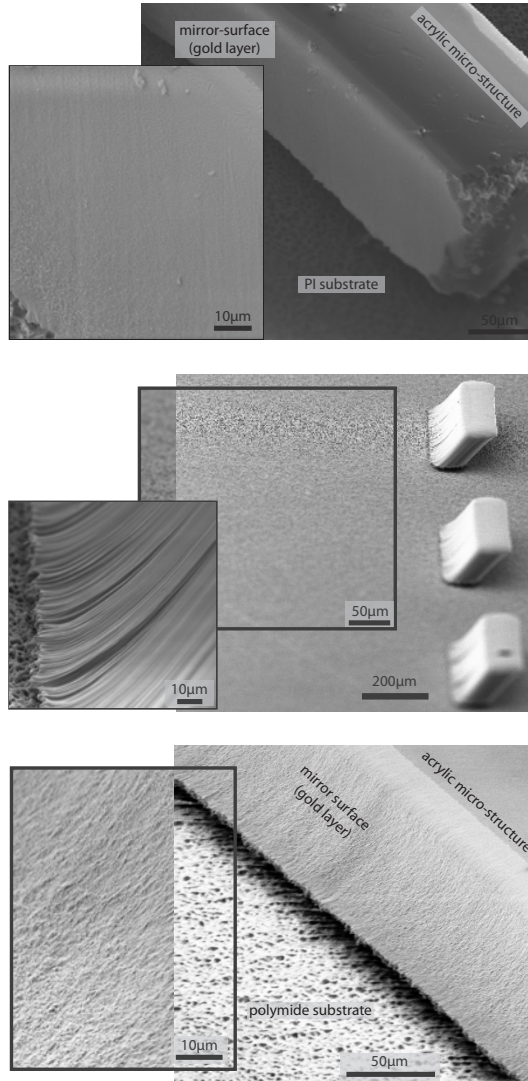


Figure 7.5: Electron micrographs of a vertical mirror surface of an in-plane micro-mirror (*top*), and tilted mirror surface of an out-of-plane micro-mirror (*middle, bottom*), reveal the different surface smoothness and the characteristic roughness of each sample.

7.1.4.2 Chemical resistance of the lower cladding

Experiments show that the PU1 cladding layer is severely affected by the surface functionalization and the NiP-plating process. The initially smooth surface is covered with defects which are visible to the naked eye, thus certainly not applicable as an optical surface. However, the PU2 cladding layer remains intact during the metal-plating process, but, only after the initially proposed ethanol [29] has been replaced by a less harsh solvent. Hexanol shows the best trade-off between resistance of the cladding and efficiency of the surface activation process.

Test samples made of PSSQ and epoxy material were exposed to the selective plating process without any apparent damage to the cladding.

7.1.5 Waveguide fabrication

7.1.5.1 Layer deposition

For ease of manufacturing, all waveguide cores herein are manufactured using the PU core material. Depending on the experiment, the PU cores are fabricated on PU1, PU2, or PSSQ lower claddings and are covered with PU1 top cladding.

The layer deposition is carried out by doctor blading. This process is applicable due to the fact that the resulting liquid layer is thinner than the gap between substrate and blade. This reduction factor is approximately 0.65 for the materials used. This implies that the substrate-to-blade gap is about 1.5 times the desired layer thickness, which is equal to the mirror thickness. Thus, the blade moves over the micro-mirror with a gap of about 0.5 times the mirror height, see Figure 7.6. However, the prospective method for accurate layer deposition on large-scale substrates is expected to be ink-jet printing [1].

7.1.5.2 Waveguide core laser writing

UV exposure of the waveguide core pattern is done by the vertical laser-head mounted on the three-axis robot-system using the 355 nm wavelength laser source, see Section 7.1.3.2.

The laser-direct writing parameters applied to define the waveguide core pattern are listed in Table 7.3.

Although the core material provides a wide process window in terms of UV dose, the latter should be kept close to the minimal level. Refraining from doing so might lead to growth of dendrite-like polymer structures close to where the laser hits the micro-mirror, see Figure 7.9 (*right*). These structures are caused by UV light scattered from the metallic surface of the micro-mirror.

The in-plane mirror needs an accurate intersection of two waveguides at the position of the mirror surface. A smooth and precise motion of the laser spot is provided by the deployed laser writing system, see Section 2.3. Furthermore, the writing speed needs to be constant to avoid cross-section variations in the waveguide.

7.1 Fabrication of the optical layer stack

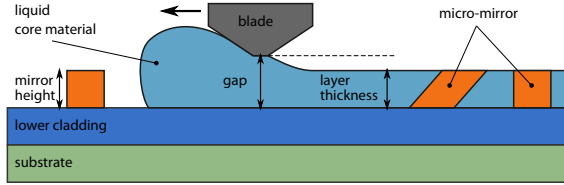


Figure 7.6: Illustration of the doctorblade coating the liquid core material onto the lower cladding. The resulting layer thickness, which is equal to the height of the micro mirrors, is about 0.65 times smaller than the adjusted gap between blade and substrate.

Table 7.3: Process parameters for patterning the PU waveguide core material.

Parameter	Symbol	Value	Unit
Spot size	w_{spot}	52	μm
Optical power spot	P_{spot}	0.7 - 1.0	mW
Effective writing speed	v_{eff}	8	mm/s
Number of passes	m	4	
Speed of laser spot	v_{spot}	32	mm/s

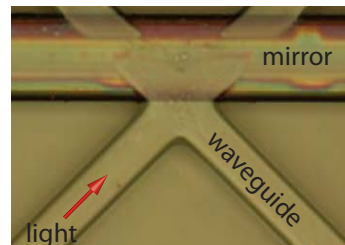
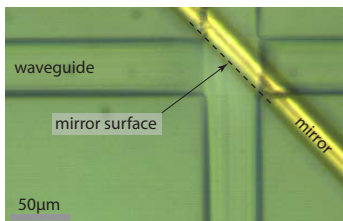


Figure 7.7: Top view of waveguide core and in-plane mirror shown in an image taken immediately after UV exposure with the digital camera mounted on the gantry (*left*); top-view microscope image (*right*) of in-plane mirror directly fabricated on the lower cladding with two waveguides intersecting on the mirror surface.

Therefore, the idea is to immediately turn off the laser once it has passed the mirror surface. However, the required micrometer accurate on-off control of the laser power is not yet deployed in the control system of the laser writing tool. Thus, in the current approach, the laser is moved at constant speed over the mirror and decelerated afterwards. This leads to an increased area requirement behind the micro-mirror. However, a subsequent version of the control system will provide a laser power control procedure which will be triggered by the actual position of the laser spot. The laser intensity will be adjusted within less than a millisecond. Given a laser moving speed of 25 mm/s , the laser intensity could be switched-off within a distance of less than $25 \text{ }\mu\text{m}$.

7.1.6 Upper cladding

The upper cladding is applied by doctorblading the liquid cladding polymer. Depending on the used material, PU1 or PSSQ, the parameters for the UV curing and baking steps are according to the fabrication of the lower cladding, described in Section 7.1.2. Generally, the targeted layer thickness of the upper cladding is approximately $20 \text{ }\mu\text{m}$ thicker than the height of the enclosed waveguide core layer. This leads to a gap of $108 \text{ }\mu\text{m}$ between doctor blade and lower cladding to eventually obtain a $70 \text{ }\mu\text{m}$ thick upper cladding.

7.2 Fabrication process for the characterization samples

For characterization purposes, we also used an alternative fabrication approach, where the micro-mirrors are fabricated separately on a different substrate. With this approach, any chemical interference of the cladding material with the delicate metal-plating process can be obviated.

A resin-polyimide-resin laminate is used as chemically inert substrate to fabricate the micro-mirrors thereon, according to Sections 7.1.3 - 7.1.4. A sharp blade is used to peel off the micro-mirror from the flexible substrate without affecting the mirror surface.

The individual micro-mirrors are then placed onto the lower cladding. The attachment of the micro-mirror was either realized by using a UV-curable optical-grade underfill adhesive (VITRALIT 6127 from PANACOL) or by placing them onto partially precured cladding material. A final UV exposure is then used to cure the adhesive or completely cure the cladding, respectively.

7.3 Fabrication process for the reference samples

Out-of-plane reference samples are intended to exclude fabrication issues related to the acrylate structuring and the wet-chemical metal plating. Therefore, the acrylate

resin is replaced by the photosensitive PSSQ core material and a common gold sputter process is used instead of the chemical gold plating process. These samples shall provide a reference value for the insertion loss of an embedded out-of-plane micro-mirror.

The PSSQ cladding material is used as the lower cladding. The micro-structure with the shape of an out-of-plane micro-mirror is fabricated out of PSSQ core material using the tilted laser head described in Figure 7.1. An immersion fluid between PSSQ layer and coupling prism is used to overcome the air gap during the tilted laser-beam exposure. This approach is applicable because the uncured PSSQ core material is already firm. In contrast, an additional cover glass is employed for the tilted UV curing of the liquid acrylate resin. The reflective layer on the tilted surface of the micro-structure is obtained by sputtering an approximately 200 nm thick gold film thereon. A shadow mask is used to protect the lower cladding around the micro-mirror. The waveguides and the upper cladding are then fabricated according Section 7.1 using the PU material.

7.4 Realized micro-mirrors

7.4.1 Embedded in-plane micro-mirrors

7.4.1.1 In-plane mirror fabricated directly on cladding

The in-plane micro-mirror illustrated and shown in Figure 7.8 (*top, middle*) is fabricated based on a PU2 cladding, an acrylate-based micro-mirror and PU waveguide core structure.

Figure 7.8 (*bottom*) shows an in-plane micro-mirror based on the PSSQ lower cladding and PU waveguide core material. The body of the micro-mirror is fabricated using the PSSQ core material. The reflectivity is achieved by sputtering a gold layer through a shadow mask thereon. The waveguide core exhibits a slight pile-up towards the height of the micro-mirror. This is due to the waveguide core layer that is slightly thinner than the micro-mirror height. This effect can be reduced by adjusting the mirror height and waveguide core thickness accordingly.

Aside from the thickness variation, the waveguide core shape close to the mirror remains undistorted, thus minimizing a negative impact on the optical properties of the waveguide path.

7.4.1.2 In-plane mirror characterization samples

The herein discussed in-plane micro-mirrors are fabricated on a separate, chemically inert substrate and then glued onto a lower cladding, as stated in Section 7.2. A clear drawback of this procedure is the pile-up of the viscous material, used to attach the micro-mirror, onto the mirror surface, illustrated in Figure 7.9 (*top right*). This effect occurred for both cases, for the liquid optical-grade adhesive (VITRALIT 6127)

7 Fabrication and characterization of embedded micro-mirrors

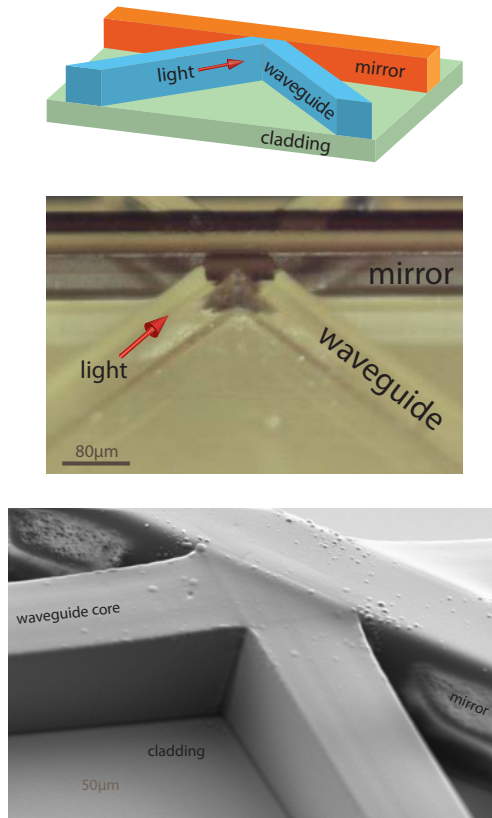


Figure 7.8: Isometric illustration (*top*) of an in-plane micro-mirror; a tilted stereo micrograph (*middle*) of an in-plane micro-mirror, fabricated and selectively gold plated directly on the lower PU2 cladding, shown with two waveguide cores intersecting on the mirror surface; an electron micrograph (*bottom*) of an in-plane reference sample micro-mirror, whose micro-structure is made of PSSQ material, showing the mirror and the joining waveguide cores (all top claddings omitted for visibility).

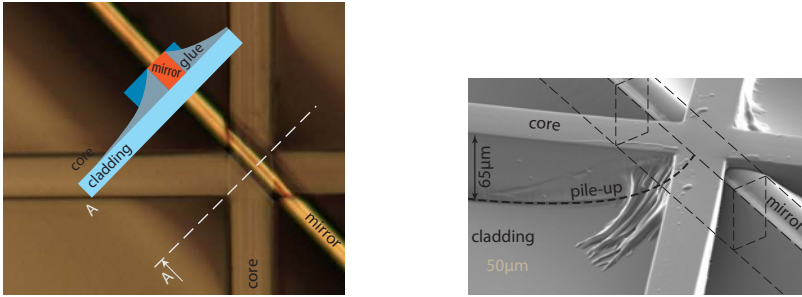


Figure 7.9: Microscopic top-view with a schematic cross-section (*left*) and a SEM image (*right*) of independently fabricated in-plane micro-mirrors with waveguides intersecting on the mirror surface, revealing the pile-up of the adhesive onto the mirror surface and the growth of dendrite-like structures.

as well as for the precured cladding, which remains viscous on the surface. Thus, the waveguide cross-section is distorted and the light is only partially guided. This leads to increased insertion losses in the optical path.

7.4.2 Embedded out-of-plane micro-mirrors

7.4.2.1 Out-of-plane mirror fabricated directly on cladding

The out-of-plane micro-mirrors, which are processed directly on the cladding material, exhibit a partial delamination of the micro-structure. This is visible in the region of the -apex of the micro-structure, see the cross-section in Figure 7.4 (*right*). This deviation from the intended mirror geometry is expected to yield a poor optical performance. Thus, no optical characterization is performed with this micro-mirror type.

7.4.2.2 Out-of-plane mirror characterization samples

The herein presented out-of-plane characterization samples are fabricated on an chemically inert substrate and are then transferred onto the optical cladding layer, according to Section 7.2. The electron micrograph images in Figure 7.10 show the main drawbacks of this fabrication approach. A recess or a pile-up of the lower cladding can be observed for a micro-mirror placed on the partially cured cladding. The surface of the partially cured cladding remains viscous. If it gets in contact with the mirror surface during the placement it results in a pile-up (*top*). Otherwise, the cladding stays below the mirror and leads to a recess of the cladding material close to the micro-mirror (*bottom*). Additional experiments with a transparent adhesive delivered similar results. Both surface deviations, pile-up and recess, lead to reduced light guiding and, thus, to increased insertion losses of the optical path.

7 Fabrication and characterization of embedded micro-mirrors

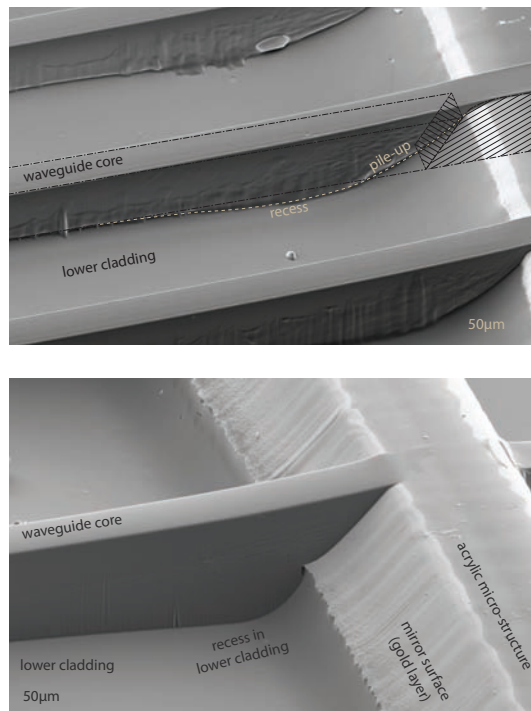


Figure 7.10: SEM images of out-of-plane micro-mirrors independently fabricated and subsequently attached onto the lower cladding, shown with waveguides connecting to the mirror surface, revealing a pile-up of the lower cladding onto the mirror surface (*top*) or a recess in the lower cladding close to the micro-mirror (*bottom*).

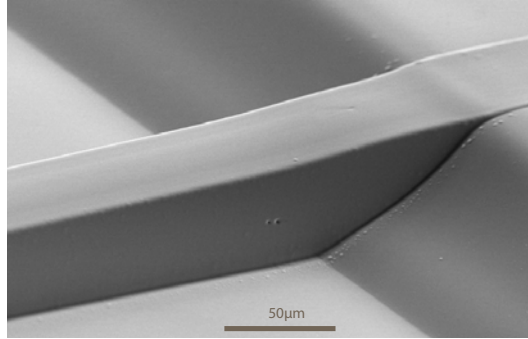


Figure 7.11: SEM image of an out-of-plane micro-mirror reference sample made out of the photosensitive PSSQ material with a sputtered gold film as reflecting layer and a waveguide made of PU material connecting to the mirror surface.

7.4.2.3 Out-of-plane mirror reference samples

Figure 7.11 shows an out-of-plane micro-mirror reference sample fabricated according to Section 7.3. The tilted mirror surface of the PSSQ micro-structure is very smooth compared to the tilted mirror surface of the acrylate based ones (Figure 7.5). This is because UV exposure of the PSSQ material is done without a coated cover glass, thus reducing optical distortions of the UV laser beam. The laser-direct-written waveguide is made of PU core material. The geometry of the waveguide core is very close to the ideal shape proposed in Chapter 5.

7.5 Mirror reflectivity

7.5.1 Micro-mirror reflectivity

The reflectivity of the micro-mirror characterization samples is measured using the microspectrophotometer (Section 6.4.2.1) and yields values of $R_{in-plane} \approx 0.5$ and $R_{out-of-plane} \approx 0.2$ for the in-plane and out-of-plane micro-mirror characterization samples, respectively. Both values are below the reflectivity achieved for the gold layer of the benchmark mirrors, see Section 6.4.3. The gold layer of the micro-mirror characterization samples and the benchmark mirrors are fabricated using the same chemical plating process described in Chapter 6. The origin of the difference in reflectivity for this gold reflectors is analyzed in the following. The reflectivity of such a gold layer depends strongly on the topography and on the layer quality.

Topography

The topography is used to describe the deviation from the ideal mirror surface. It leads to (i) scattering of the incident light and to (ii) pointing errors of the reflected beam. Both effects can lead to optical losses, because part of the reflected light will not be collected from the respective waveguide.

7 Fabrication and characterization of embedded micro-mirrors

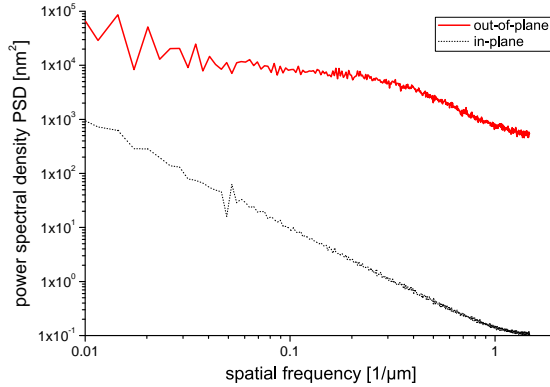


Figure 7.12: Power spectral density (horizontal scans) of an in-plane and an out-of-plane micro-mirror surface, measured with the optical profiler (VEECO).

The surface roughness of an in-plane micro-mirror is measured in horizontal and vertical direction using an optical profiler (VEECO) and yields a roughness of $R_a^h = 8 \text{ nm}$ and $R_a^v = 19 \text{ nm}$, respectively, for a scan range of $50 \mu\text{m}$. The surface roughness of an out-of-plane micro-mirror is measured to be $R_a^h = 270 \text{ nm}$ and $R_a^v = 132 \text{ nm}$ for the horizontal and vertical scan direction, respectively. Both, the in-plane and the out-of-plane micro-mirror, are made of acrylate resin and fabricated according to the process sequence for characterization samples, see Section 7.2. The different roughness values for the in-plane and out-of-plane mirrors are expected to originate from the coated cover glass required for the tilted UV exposure of the out-of-plane micro-structure. In contrast, the out-of-plane reference sample, made of PSSQ core material and UV-cured without the coated cover glass, shows much smoother surfaces, see Figure 7.11.

The power spectral density (PSD) resolves the roughness of the surface into spatial frequencies. Figure 7.12 shows the power spectral density of the horizontal line scans of the in-plane and out-of-plane micro-mirror characterization samples. It reveals that the amplitude of the out-of-plane surface roughness is significantly higher over the complete spatial frequency range (10 mm^{-1} to $1 \mu\text{m}^{-1}$). A correlation between the reduced reflectivity value and the increased surface roughness of the out-of-plane compared to the in-plane micro-mirror can be observed. This is an indication of the origin of the difference in reflectivity between the two micro-mirror types.

The surface roughness of the in-plane micro-mirror complies well with the commonly used $\lambda/20$ -criterion for optical grade surfaces. Thus, the current fabrication process for in-plane micro-mirrors achieves a surface quality which is acceptable for the current development status of the micro-mirror.

Layer quality

Besides the surface roughness, another effect is required to explain the significant difference in reflectivity between in-plane micro-mirror ($R_{in-plane} \approx 0.5$) and the benchmark mirror ($R_{benchmark} = 0.86$). Impurities in the gold layer are another factor of the surface quality, which is expected to impede the metallic reflectivity properties of the gold layer. There are different sources leading to impurities in the gold layer. First, nickel and phosphor from the underlying metal layer can contaminate the gold layer, see Section 6.4.3. However, these nickel and phosphor based impurities would also appear in the benchmark mirrors. Thus, they do not provide an explanation for the difference in reflectivity between micro-mirrors and benchmark mirrors.

The microscopic dimension of the micro-mirror, compared to the benchmark mirrors, potentially leads to less efficient selective activation and catalyst deposition processes. The resulting nonuniform growth of the metal layers would affect the reflectivity properties of the material.

Micro-mirrors on cladding

In-plane micro-mirrors fabricated on PU2 cladding material yield a reflectivity of $R_{in-plane} = 0.13$ after the selective metal plating process. This value is significantly lower than the reflectivity for the in-plane micro-mirror characterization samples ($R_{in-plane} \approx 0.5$). This indicates that the lower cladding material could impair one or more processes of the selective metal-plating. In particular, the harsh selective surface activation, the delicate catalyst deposition, and the nickel plating at elevated temperatures are potentially affected. Understanding all the failure mechanisms and quantifying their influence to the achievable reflectivity will be a crucial task in the further optimization of the micro-mirror process.

7.6 Micro-Mirror insertion loss**7.6.1 Characterization method**

The embedded micro-mirrors are characterized by the insertion loss of the complete optical path, consisting of input and output waveguides and micro-mirror, according to the optical setup in Figure 7.13. The 850 nm wavelength light from a tuneable diode laser is coupled into the waveguide by an optical fiber through an immersion fluid layer. Singlemode fibers have been employed to obtain reproducible mode launch conditions at the waveguide input facet. The presented insertion losses are adjusted for the propagation losses of the waveguides.

7.6.2 Results

Figures 7.8 to 7.10 show electron micrographs of micro-mirrors with waveguide cores connecting to the mirror surface. Once the upper cladding is applied on these structures, insertion losses are measured using the setup shown in Figure 7.13.

7 Fabrication and characterization of embedded micro-mirrors

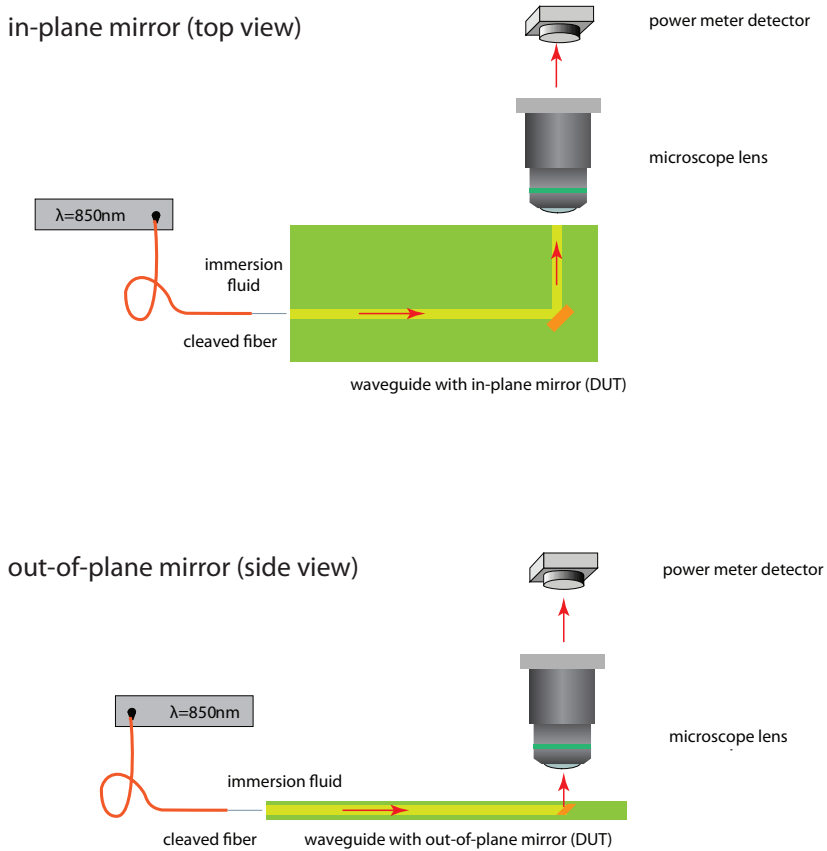


Figure 7.13: Schematic of insertion loss measurement setup for embedded in-plane (*top*) and out-of-plane (*bottom*) micro-mirrors, using an 850 nm wavelength diode laser and a cleaved fiber to butt-couple the light into the waveguide, and microscope lens to image the endfacet onto the power meter, whereby reference waveguides are used to calibrate the measurements.

The insertion loss measurements of the characterization samples, the reference sample and the micro-mirror are summarized in Table 7.4 and supplemented with the respective reflectivity value, if applicable. The reflectivity losses allow for a qualitative comparison, but they do not provide a quantitative insertion loss value. This is because the optical properties of the used measurement equipment for insertion loss and reflectivity measurements are different.

In-plane micro-mirror insertion loss

The reduced reflectivity $R = 0.13$ of the selectively gold plated in-plane mirror is expected to be owing to the PU cladding material during the plating process. Thus, no insertion loss measurements are performed on this sample.

The characterization sample in-plane micro-mirror exhibit an insertion loss of 5.5 dB. Part of this loss value can be allotted to the low reflectivity ($R = 0.5$) of the micro-mirror itself. Various deviations from the ideal geometry of the waveguide intersection contribute further losses. The most obvious deviations are the pile-up of the lower cladding, the dendrite-like structures of core material, the slight height difference between mirror and core as well as possible mirror-surface deviations, see Figure 7.9.

Out-of-plane micro-mirror insertion loss

For the reference sample out-of-plane micro-mirror, based on the smooth surface of the direct-on-clad approach and the sputtered gold layer, an insertion loss of only 1.5 dB is achieved. Small deviations from the ideal geometry of the waveguide and mirror configuration, shown in Figure 7.11, are expected to contribute radiation losses. However, this loss value can be taken as target figure for the further optimization of the out-of-plane micro-mirrors.

The characterization sample out-of-plane micro-mirrors in Figure 7.10 exhibit an insertion loss of approximately 7 dB. The main loss contributors are (i) the low reflectivity of the mirror surface ($R = 0.2$), described in Section 7.5.1, and (ii) the deviations from the ideal geometry of the waveguide and micro-mirror intersection.

7.7 Micro-mirrors in an electro-optical flex board

The work in this section describes the implementation of out-of-plane mirrors into an electro-optical flex board as a substrate for high-speed optical data transmitter and receiver assemblies. The goal of this integration approach is to explore the potential of embedded micro-mirror for compact parallel optical modules.

One advantage of optical interconnects is the very high bandwidth density with respect to electrical interconnects, see Section 1.1. To fully exploit this advantage, a very high level of integration of the electro-optical module is required.

The herein proposed design of an electro-optical flex assembly is meant to be attached on top of a carrier laminate. This brings the optical conversion very close to the processor, thus avoiding long electrical traces and allowing a very high

7 Fabrication and characterization of embedded micro-mirrors

Table 7.4: Tables a) to c) represent the measured reflectivity and insertion loss values for the a) characterization samples micro-mirrors, b) the reference sample micro-mirrors, and c) the micro-mirrors fabricated on a PU2 cladding layer.

a) Characterization sample micro-mirror				
Mirror type	Gold layer	Figure	Mirror reflectivity	Insertion loss
in-plane	wet-chemical	7.9	0.5	5.5 dB
out-of-plane	wet-chemical	7.10	0.2	7 dB

b) Reference sample micro-mirror			
Mirror type	Gold layer	Figure	Insertion loss
out-of-plane	sputtering	7.11	1.5 dB

c) Micro-mirror fabricated on cladding			
Mirror type	Gold layer	Figure	Mirror reflectivity
in-plane	wet-chemical	7.8	0.13

electrical wiring density. An electro-optical conversion module, with a high-density electrical connector, on the one-hand side, and a dense optical connector, on the other hand side, can be used to add additional high-speed I/O channels to a processor package, see Figure 7.14, thus providing a solution to overcome the data bottleneck between carrier laminate and printed circuit board in high-performance computing applications [113].

7.7.1 Design

The herein proposed test vehicle can be described as an active optical flex. One end of the flexible substrate is terminated with a high-density electrical connector [113], the other end provides the alignment features for an MT-compliant optical connector [51]. The out-of-plane mirror couples the light directly from the optoelectronic chip to the waveguide array. The top view and various details are shown in Figure 7.15. This active optical flex can be designed as transmitting (VCSEL) or receiving (photodiode) device. The individual elements of this active optical flex are discussed in the following.

Polyimide Substrate

A 50 μm thick polyimide (PI) sheet is used as flexible substrate. This thickness allows for impedance-matched electrical differential-lines with a very narrow pitch. On the top and the bottom side of the substrate, the copper traces and the electrical vias are manufactured by the PCB supplier. For reliable electrical interfaces, the copper is

7.7 Micro-mirrors in an electro-optical flex board

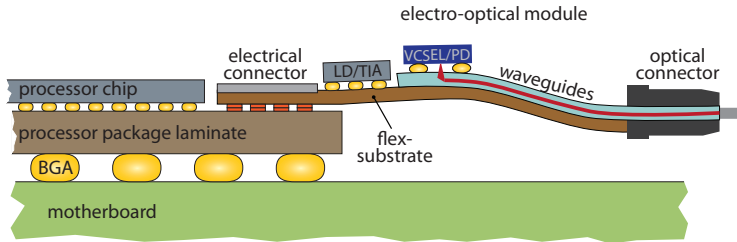


Figure 7.14: Illustration of a potential application of the electro-optical flex module [113], whereby the high-density electrical connector of the electro-optical flex is directly attached to the processor package laminate.

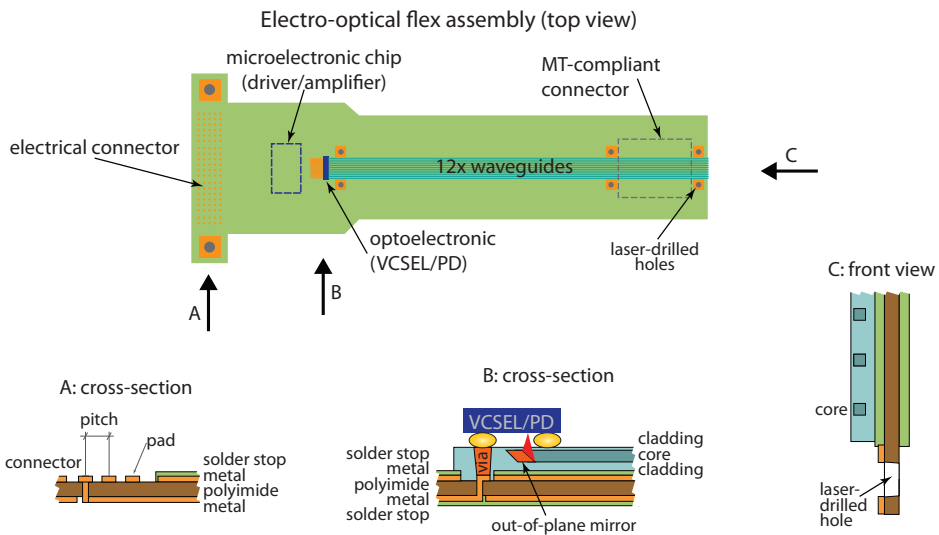


Figure 7.15: Design of the electro-optical flex assembly with a top view (*top*) of the complete assembly, a cross-section detail of the electrical connector part (*view A*) and the optoelectronic part (*view B*), and a front view of the optical connector area (*view C*).

7 Fabrication and characterization of embedded micro-mirrors

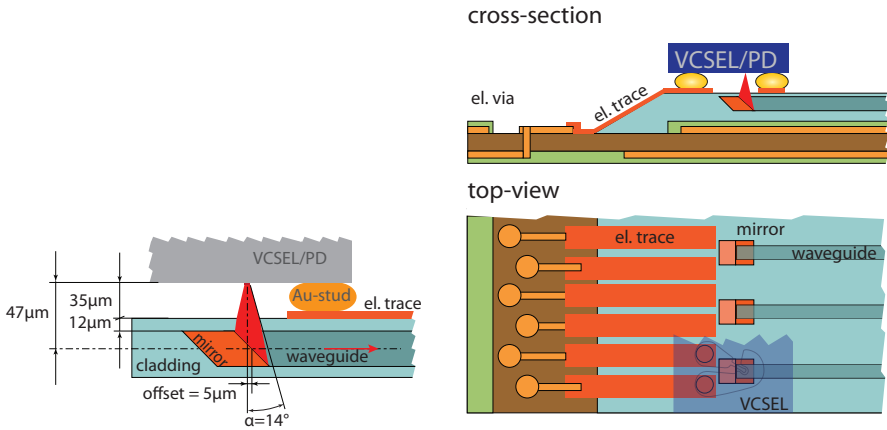


Figure 7.16: Layout of the light coupling from a VCSEL to the waveguide using a out-of-plane mirror (left), illustration of the electrical slope approach to facilitate the electrical connection from the cladding top-side to the substrate (right).

protected with a nickel and gold layer. The metal traces, except all electrical pads and alignment features, are covered with a structured solder stop mask to obtain electrical insulation.

Microelectronic chip

Low-power CMOS (complementary metal oxide) based laser-driver and amplifier chips are intended to be mounted on the transmitting and receiving optoelectronic flex, respectively. Commercially available 12-channel laser-drivers and TIAs (transimpedance amplifier) provide a bandwidth of up to 12.5 Gb/s per channel and consume, combined, less than 8 mW/Gbps per channel.

To simplify the assembly of the prototype, the microelectronic chips are currently electrically connected to the flexible substrate using wire-bond technology. In an ultimate design, flip-chip assembly will be used because of the following advantages: a) no unmatched impedance along the bond wire, b) manufacturing efficiency, and c) simplified thermal management.

Optoelectronic element

The optoelectronic elements, i.e., the VCSEL and PD arrays, which provide the E/O (electro-optical) conversion are directly coupled to the micro-mirror, without additional optical elements. Both light beams, the one from the VCSEL to the micro-mirror and the one from the micro-mirror to the PD, are divergent. For geometric optical reasons, the distance between the active optical area of the optoelectronic element and the embedded micro-mirror is important. Extending this distance above a maximum value leads to excess coupling losses, because the micro-mirror or the active area of the PD are smaller than the cross-section of the divergent beam. Figure 7.16 (left) shows the parameters for the transmitting module: waveguide

thickness of $42\ \mu\text{m}$, beam-divergence half-angle of $\alpha = 14^\circ$, and an $\varnothing 7\ \mu\text{m}$ light emitting area on the VCSEL. The distance between center of the micro-mirror and the active area of the VCSEL is set to $47\ \mu\text{m}$. This leads to a maximum top cladding thickness above the micro-mirror of $12\ \mu\text{m}$ and a maximum gap thickness between cladding and VCSEL of $35\ \mu\text{m}$. The electrical traces on top of the cladding are designed to be $5\ \mu\text{m}$ thick. In a similar manner, the positioning parameters for the receiving module can be calculated. For this, the active area of the PD of $\varnothing 70\ \mu\text{m}$, and the divergence of the waveguides have to be taken into consideration.

The connection between the optoelectronic chip and the electrical traces is realized by gold stud balls on the chip and conductive adhesive. This method allows to comply with the aforementioned maximum gap between cladding and optoelectronic chip of $35\ \mu\text{m}$. The required precise alignment of the optoelectronic chip to the flexible substrate and the curing of the conductive adhesive can be done by means of a flip-chip bonder.

Electrical traces

The electrical connection from the electrical traces on top of the optical layer to the signal layer on the substrate, can be accomplished as follows:

a) "Via in Pad": In this approach, the electrical vias directly terminate in the pads for the attachment of the optoelectronic chip, shown in Figure 7.15 (*cross-section B*). This requires the capability to laser-drill vias with a diameter of $80\ \mu\text{m}$ and a pitch of $125\ \mu\text{m}$. Challenging is in particular the short distance between electrical active pads and the optically active area.

b) "Via plus fan-in": In this case an electrical fan-in is added between the electrical vias and the pads for the optoelectronic chip, this to relax the requirements for the via fabrication. Various methods are known to fabricate these traces on top of the cladding. A straight forward method would be sputter deposition of a metal layer. Structuring is performed by photolithography in combination with either lift-off or etching. The metal traces can then be used directly or as a seed layer for an electroless metal-plating. Another approach is to use a metalized photoimageable auto-catalytic resin, proposed by [57]. In this approach, the photosensitive resin acts as seed layer for the electrochemical metal deposition process.

c) "Electrical slopes": This method combines the electrical vias and traces into one process step, see Figure 7.15. A slope in the cladding is fabricated by using laser milling, similar to the via drilling. This slope ranges from the board level to the top of the waveguide layer. On this slope, electrical traces can then be fabricated using one of the aforementioned processes (sputter deposition with lift-off or etching, photoimageable auto-catalytic resin, and metal plating). Another approach already used in the industry, is ink-jet printing to write the electrical lines directly with a conductive nano-ink [31, 30]. After printing, the ink is sintered to achieve the desired low-resistance condition.

All approaches have in common that the electrical connection to the optoelectronic chip (VCSEL or photodiode) can be obtained either by conductive adhesives or by soldering. All electrical pads on the optoelectronic chip are on one side of the optical

active array, e.g., on the left-hand side in Figure 7.15 (*top*). The pad on the right-hand side of the active area is used as mechanical support. Finally, the chip will be permanently glued to the cladding. An optical underfill can be considered below the PD to further relax the positioning requirements in vertical and lateral direction. This, because the divergence of the beam propagating in an optical adhesive is reduced compared to the propagation in air.

Integration and thermal management

The concept is also compatible with the stacking of several flex assemblies on top of each other. The optical connector can combine multiple substrates, resulting in a MT-compliant multilayer, e.g., 4×12 connector [51].

The TIA mounted on the receiver module dissipates a total power of 0.8 W [44] for the 12 channels on the module. Regarding the transmitter module, there, the laser driver contributes 14 mW of dissipated power per channel [44], and the VCSEL contributes another 14 mW ($I_{VCSEL} = 6.5$ mA, $V_{VCSEL} = 2.1$ V, $\Delta V_{VCSEL}^{P-P} = 450$ mV) [112] per channel. This results in a total of 0.34 W of dissipated power for the 12-channel transmitter module. These power levels require an adequate thermal management. The backside of the VCSEL array can directly be connected to a heat spreader, while the PD array does not require one. The thermal management of the microelectronic chips for the wire-bond and the flip-chip approach are different. The wire-bond approach requires that the backside of the microelectronic chip is glued to the substrate with a thermally conductive adhesive. The thermal resistance of the substrate itself is reduced by using copper vias as thermal vias, while the substrate is connected to a heat spreader. In the flip-chip approach, the backside of the microelectronic chips is directly accessible to attach a heat spreader. Single substrate assemblies might be thermally connected to an existing heat sink. For multi-substrate assemblies, one can consider a fin-like structure (interleaved heat spreader) to provide heat dissipation close to the microelectronics. In such a case, thinned microelectronic chips could reduce the space requirements and improve the heat transfer.

Electrical connector

A compression-based high-density electrical connector is employed to connect the active flex to the processor package [113] (Figure 7.14). The gold surface of an electrical pad on the optical flex assembly is directly in contact with the pad on the package. A compressible plate distributes pressure uniformly among the pads and provides dimensional compliance in the vertical direction. The test vehicle design herein has a pitch of 800 μm between connector pads, see Figure 7.15 (*view A*), to enable compatibility with existing hardware. Connectors with a pitch of 400 μm have successfully been tested. A 200 μm pitch connector is under investigation.

Passively aligned MT-compliant connector

Based on the passive alignment concept for rigid printed circuit boards, described in Chapter 4, passive alignment approaches for flexible substrates have recently

been proposed [50, 51, 61]. Our approach makes use of laser-drilled copper marker structures. It uses an injection-molded high-precision ferrule and a reusable ceramic base plate [50, 51]. This enables the accurate alignment of one or more waveguide layers with respect to the MT-compliant alignment pins. The same marker patterns have been included on the optical end of the flex, enabling the passive alignment of the MT-compliant ferrule thereon.

7.7.2 Fabrication

The samples are fabricated using the processes described in Section 2.3. For ease of fabrication, the PU waveguide material set is used. The out-of-plane mirror, which is required to couple the light from the optoelectronic device to the waveguide, is fabricated according to the manufacturing approach for characterization samples, described in Section 7.2. Now the micro-mirror is removed from the substrate and placed onto the partially cured lower cladding. An additional UV exposure step is required to cure the lower cladding and permanently attach the micro-mirror. In the next step, the waveguide array, which runs in a straight line from the connector to the micro-mirror, is fabricated. The upper cladding finalizes the optical layer and provides the slope whereon the electrical traces will be placed, see Figure 7.16.

The metallic pads and the electrical traces, required to connect the optoelectronic die to the signal pads on the substrate, are fabricated according to the design of the electrical slope approach, described in Section 7.7.1. The metal layer is a sputtered gold film. Infrared laser ablation (SMART LASER SYSTEMS) is used to directly structure the gold layer. The electro-optical flex board is then ready for populating of the optoelectronic and electronic devices at a PCB assembler.

7.7.3 Experimental results

Figure 7.17 shows the built electro-optical flex board as basis for the parallel-optical transmitter module, including waveguides and out-of-plane mirror. The waveguide end-facet is illuminated using a red laser. The light is then reflected by the out-of-plane mirror, noticeable by the red spot on the top-side of the cladding, Figure 7.17 (*detail*). The dashed lines represent the contact metallization and the active area of the respective VCSEL. The active area is aligned to the out-of-plane mirror.

The coupling loss of the out-of-plane mirrors is measured in Section 7.6 using a characterization sample. This sample is fabricated with the same process parameters as used for the flex board and yields a coupling loss of approximately 7 dB.

7.8 Summary

In this chapter, laser-direct-writing of micro-structures based on acrylic resin as a means to fabricate micro-mirrors, embedded in an optical waveguide layer stack,

7 Fabrication and characterization of embedded micro-mirrors

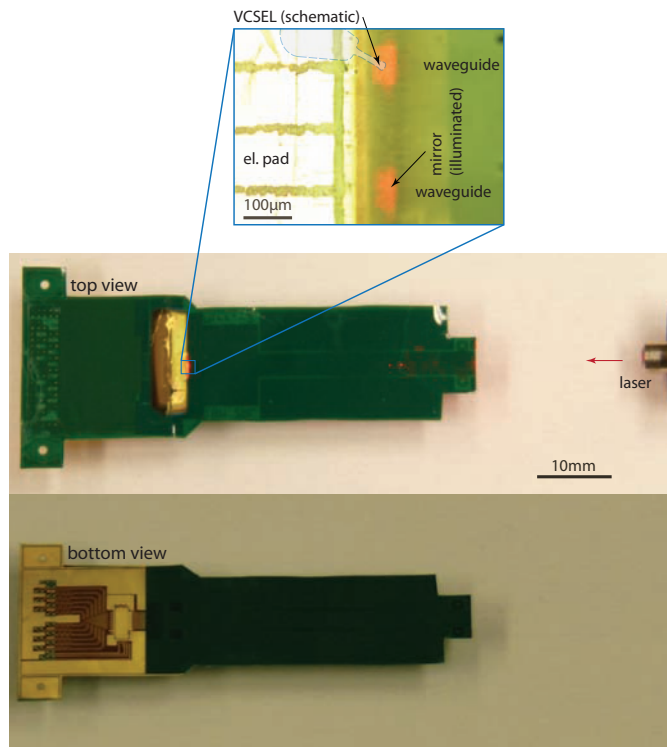


Figure 7.17: Electro-optical flex board with an electrical connector on the left-hand side and an optical facet on the right-hand side; showing the top side (*top view*), a detailed view of the illuminated coupling mirror and the electrical pad (*detail*), and the bottom side with the spot for the electronic chip and the differential signal lines leading to the electrical connector (*bottom view*).

is presented. Two different types, the in-plane (a) and the out-of-plane (b) micro-mirrors, have been fabricated, coated and characterized, according to the processes described in Chapters 5 to 7.

(a) In-plane micro-mirrors are exposed using a vertical UV-laser beam. This is a straight forward adaption of the laser equipment used for the waveguide core fabrication. Mirror-grade optical surfaces, with a roughness $R_a \leq 20$ nm, were realized.

(b) Out-of-plane micro-mirrors are fabricated using a tilted UV-laser beam. Immersion assisted prism coupling is used to realize a 45° tilted laser passing the photosensitive acrylate layer. Because of the liquid state of the acrylate resin, an intermediate cover glass with anti-sticking coating is required. The demonstrated out-of-plane micro-mirrors exhibit a surface roughness of $R_a = 270$ nm. The higher roughness, compared to the in-plane structures, can be explained by the anti-sticking coating on the cover glass. The same laser configuration used in combination with a firm photosensitive layer, and thus without the need of a coated cover glass, leads to a surface morphology comparable to the one of the in-plane structures.

The selective wet-chemical metal plating process, described in Chapter 6, was used to create micro-mirrors by applying a reflective gold layer on top of the aforementioned (a,b) micro-structures. The micro-mirrors built on polyurethane cladding exhibit very low reflectivity. The cause is a chemical interaction of the cladding material with the chemistry of the selective metal deposition process. Therefore, in order to obtain characterization samples, the micro-mirrors were fabricated on an inert substrate and subsequently transferred to the lower cladding. This enabled the fabrication of embedded micro-mirror characterization samples independent from the cladding. This way, gold coated in-plane micro-mirrors which exhibit a reflectivity of $R_{in-plane} \approx 0.5$ are demonstrated.

The fabrication of in-plane and out-of-plane micro-mirrors embedded in the optical layer has successfully been demonstrated. A critical process remains the core layer deposition and the UV patterning of the waveguide cores. The layer thickness has to be controlled accurately to match the height of the micro-mirrors. In case of a thicker core layer, some of the guided light would not impinge on the mirror surface. On the other hand, a thinner core layer exhibits the tendency to pile-up to the edge of the micro-mirror. This leads to variations in the waveguide core cross-section and thus to additional optical losses. Positioning errors of less than ± 2 μ m between waveguide and in-plane micro-mirror were achieved. This accuracy is based on the vision system and the position accuracy of the laser writing tool.

An insertion loss of 5.5 dB was achieved for in-plane micro-mirrors, which were fabricated as characterization samples on a chemically inert substrate.

A reference sample of an out-of-plane micro-mirror, which is fabricated based on a firm photosensitive (PSSQ) material in combination with a sputtered gold layer, yields an insertion loss of only 1.5 dB. This is due to the low surface roughness of the mirror surface and the high reflectivity of the sputtered gold layer.

The advantage of the compact integration scheme, which is based on the proposed

7 Fabrication and characterization of embedded micro-mirrors

embedded out-of-plane micro-mirrors, is demonstrated by the electro-optical flex board as substrate for a compact optical module, described in Section 7.7. The concept of this flexible module is to convert the electrical signals to the optical domain on top of the processor package laminate, thus placed very closely to the processor and connected with a very high-density interconnects to the processor laminate. These additional off-package data channels can help to reduce the data bottleneck between processor laminate and PCB. The key feature is the embedded micro-mirror approach, in combination with the electrical layer fabricated directly on top of the upper cladding. This allows for placing the active area of the optoelectronic chip with a vertical separation of only 70 μm from the center of the waveguide layer, thus eliminating the need for additional lenses or beam-shaping mirrors. An economical optical connectorization of the module is provided by the implemented passive alignment technique.

8 Experiments on modal power coupling in waveguides

A mode coupling matrix approach is presented to describe the light propagation characteristics of multimode waveguides. An optical link is thereby described as concatenated waveguide segments and each segment is represented by a modal power coupling matrix, which describes the relation between input and output modal power distribution of the waveguide segment.

The experimental section demonstrates an optical setup for measuring the modal power coupling matrix for simple waveguide elements. The respective mode field pattern on the waveguide input facet is generated by means of a spatial-intensity and a spatial-phase modulator. Individual modes are observed via an intensity measurement of the waveguide end-facet. In addition, an approach which deploys optical Fourier transformation is tested to analyze the modal power distribution if multiple modes are present.

8.1 Introduction

Generally, the adequate design of an optical system requires comprehensive knowledge about the light propagation in the respective system. In optical interconnect applications, it is required to predict the performance and, in particular, the required optical power budget for the signal transmission.

One approach to obtain this data is to employ optical simulation. Several powerful simulation tools are available for optical applications. Ray tracing tools are successfully used in the design and optimization of lenses and optical imaging systems. The beam propagation method is preferably applied to waveguide applications with very few modes. Ab-initio methods, such as the finite-difference time-domain simulation, are used to model complex electro-magnetic systems, such as photonic band gap structures. Beam propagation and ab-initio simulations are limited to relatively - compared to the wavelength - small structures.

The main challenges for an efficient simulation tool for multimode waveguide applications arise from the large number of modes, the light scattering at the imperfect core-cladding interfaces, and the numerous reflections which occur during the long propagation distances. Various research efforts towards the simulation of multimode communication systems are in progress. Ray-tracing based approaches are in particular of interest because of their potentially time-efficient algorithm [99]. A hybrid ray-tracing approach has been demonstrated to cover arbitrary core shapes and nano-scale surface roughness [5]. Furthermore, highly multimodal waveguides are successfully simulated using the coupled power theory [69]. For the time being, no commercially available optical simulation tool is able to cope with the requirements of multimode waveguide systems, which are of interest herein.

Currently, the common approach to predict the optical performance of a multimode link relies on basic propagation loss measurements only. The propagation loss, an important characteristic number of multimode waveguides, is measured as difference between the input and output optical power. The propagation loss of the optical link is then calculated by summing up the individual waveguide segments. Such a link might consist of straight waveguides, waveguide bends, waveguide crossings, coupling mirrors and connections. Experience gained during the bring-up phase of various optical interconnect prototypes shows that significant discrepancies between calculated and actually measured loss values in an optical link can occur. These discrepancies arise from the limited data provided by the scalar insertion loss value. In an actual multimode optical element, the propagation loss differs significantly for the different optical modes, and due to imperfections in, and straightness deviations of the waveguides, the modal power distribution will change during the propagation. Thus, the effectively occurring propagation loss value in a section of an optical link can vary due to the changes in the modal power distribution during propagation. Hence, the loss values of individual waveguide elements are, in general, not sufficient to predict the actual loss value of a complete optical link.

8.2 Model for mode propagation in waveguides

Light waves can only propagate as discrete modes in a dielectric waveguide. Each guided mode corresponds to an electromagnetic field distribution as a solution of MAXWELL'S equations for the waveguide [76]. Analytical and numerical approaches to calculate the modes in different types of waveguides are described in Chapter 3. Perturbations and nonuniformities in the longitudinal direction of the waveguide lead to power coupling between the modes.

8.2.1 Amplitude coupling

The electromagnetic waves in the modes are described by the modal amplitude distribution $\underline{\Phi}$, a complex vector with $Re(\underline{\phi}_q)$ and $Im(\underline{\phi}_q)$ representing the amplitude and the phase of mode $\underline{\phi}_q$, respectively. The coupled-mode theory describes the amplitude coupling between the modes of waveguide structures [97, 98, 42, 69, 71, 77]. The amplitude coupling between guided modes in a waveguide section can be described by the amplitude coupling matrix $\underline{\mathbf{K}}$ which contains the complex amplitude coupling coefficients $\kappa_{p,q}$.

8.2.2 Power coupling

The coupled mode theory is in particular of interest if the various coupling mechanisms, which occur in the waveguide, can be accurately described with coupling matrices [69, 71]. Herein we follow an approach towards an application oriented formalism, in analogy to the coupled mode formalism, in order to describe the mode propagation in waveguides. Thereby, a certain propagation distance in a waveguide is described by a mode coupling matrix which relates the input modal power distribution with the output modal power distribution. The approach pursued herein makes use of an approximation. Instead of using the modal amplitude coupling, only the modal power coupling is considered. This simplification is based on the assumption that the number of modes is very large. This is expected to lead to an averaging effect in the modal amplitude coupling and, thus, only the power carried in each mode will be determined. The phase term of the mode is not taken into account, and is therefore subject to be omitted. Therefore, in analogy to the modal amplitude coupling with $\underline{\Phi}$ and $\underline{\mathbf{K}}$, the modal power coupling formalism is as follows. The amount of light carried in each mode is described by the modal power distribution vector Φ . Its real elements ϕ_q represent the optical power carried in the respective mode q . The vectors ${}_{in}\Phi$ and ${}_{out}\Phi$ describe the input and output modal power distribution, respectively.

$${}_{in}\Phi = \begin{bmatrix} {}_{in}\phi_{q=1} & {}_{in}\phi_2 & \cdots & {}_{in}\phi_Q \end{bmatrix}^T \quad (8.1)$$

$${}_{out}\Phi = \begin{bmatrix} {}_{out}\phi_{p=1} & {}_{out}\phi_2 & \cdots & {}_{out}\phi_P \end{bmatrix}^T \quad (8.2)$$

8 Experiments on modal power coupling in waveguides

In general, the number of elements Q of ${}_{in}\Phi$ is not necessarily equal to the number of elements P of ${}_{out}\Phi$.

A modal power distribution ${}_{in}\Phi$ launched at the waveguide input leads to a certain modal power distribution ${}_{out}\Phi$ at the output. The relation between them is described by the modal power coupling matrix \mathbf{K} with the power coupling coefficients $\kappa_{p,q}$.

$$\mathbf{K} = \begin{bmatrix} \kappa_{p=1,q=1} & \kappa_{1,2} & \cdots & \kappa_{1,Q} \\ \kappa_{2,1} & \kappa_{2,2} & \cdots & \kappa_{2,Q} \\ \vdots & \vdots & \ddots & \vdots \\ \kappa_{P,1} & \kappa_{P,2} & \cdots & \kappa_{P,Q} \end{bmatrix} \quad (8.3)$$

The two-dimensional matrix \mathbf{K} contains the power coupling coefficients $\kappa_{p,q}$ from each input mode ${}_{in}\Phi_q$ to each output mode ${}_{out}\Phi_p$. For each output mode, one can now calculate the total amount of power received from all input modes as

$${}_{out}\Phi_p = \sum_{q=1}^Q \kappa_{p,q} \cdot {}_{in}\Phi_q \quad (8.4)$$

Thus, the power coupling matrix \mathbf{K} , describes how the power is coupled from the input modal power distribution ${}_{in}\Phi$ into the output modal power distribution matrix ${}_{out}\Phi$ by a simple matrix multiplication,

$${}_{out}\Phi = \mathbf{K} \cdot {}_{in}\Phi \quad (8.5)$$

The power coupling matrix of a waveguide section can be interpreted as power transfer characteristic of the respective waveguide.

If preferred, the power coupling matrix can be defined for a unit length, in case of straight waveguides, or, for a unit angle, in case of waveguide bends.

8.2.3 Origin of modal power coupling

Coupling of optical power between modes in a waveguide occurs from perturbations and nonuniformities along the propagation direction. Such possible imperfections are (a) cross-section variations, (b) deviation from straightness, (c) surface roughness, and (d) scatter points.

(a) Cross-section variations lead to a change of the modes in the waveguide. These geometrical variations of the waveguide cross-section originate from the fabrication processes. The polymer waveguide technology deployed herein, which is described in Section 2.3, exhibits geometrical variations of up to about $\pm 4\%$.

(b) Bends in step-index waveguides lead to power coupling between modes. The radius of curvature and the length of the bend influence the coupling coefficients [69]. Three different kinds of bends have to be considered. The waveguides can follow a curved pattern within the waveguide plane, which is parallel to the substrate. In

addition, the waveguides can be curved due to a bending of the flexible substrate. The third kind of bend that can occur are micro-bends which result from the waviness of the substrate. They in particular occur when FR4 substrates are used. This type of substrate is very common to PCB manufacturing. It is made of woven glass fabric embedded in a resin matrix. The resulting waviness exhibits a pitch of 0.8 mm and an amplitude of up to 5 μm . This leads to consecutive micro-bends with radii down to approximately 16 mm.

(c) Perturbations at the waveguide core-cladding interface, the border between the high- and low-refractive index regions, cause the guided light to scatter. The consequence is, that the scattered energy can couple to other guided or unguided modes. The origin of these perturbations is the surface roughness of the waveguide core [89].

(d) Impurities and inhomogeneities in the material are other sources of intrinsic light scattering. They might origin from the material itself or being added during the fabrication. Depending on the geometrical dimension of the scatter points and the physical properties, different types of scatter processes occur [33].

8.2.4 Mode designation in waveguides

The previously described model for the modal power coupling during propagation, Section 8.2.2, is a very general description. The geometry and other properties of the waveguide are not considered therein. Now, one has to define a convention to map the modes of an application-specific kind of waveguide to the previously defined linear array of modal power values ${}_{in}\phi_q$ and ${}_{out}\phi_p$, respectively. Herein proposed are possible conventions for three different types of waveguides. The physical properties of the modes in different types of waveguides are described in detail in Chapter 3.

Step index fiber

Table 8.1: Convention for the designation of the eight guiding-modes of the step-index fiber diameter ($\emptyset 19.7 \mu\text{m}$, $N.A. = 0.1$, $n_{core} = 1.46$, and wavelength $\lambda = 850 \text{ nm}$).

n_{eff}	LP_{lm} mode designation	ϕ_i mode designation
1.4597	LP_{01}	ϕ_1
1.4593	LP_{11}	ϕ_2
1.4587	LP_{21}	ϕ_3
1.4585	LP_{02}	ϕ_4
1.4580	LP_{31}	ϕ_5
1.4576	LP_{12}	ϕ_6
1.4567	LP_{22}	ϕ_7
1.4566	LP_{03}	ϕ_8

The modes are assigned according to the decreasing value of the effective refractive index n_{eff} . It starts with the mode with the highest effective refractive index, the fundamental mode, at index $i = 1$. Table 8.1 shows the mode designation for a specific step-index fiber.

8.2.4.1 Rectangular or arbitrarily shaped dielectric waveguide

Figure 3.9 shows the propagating modes in the k -space for an ideally rectangular waveguide. The approximate TE and TM modes and the corresponding effective refractive index n_{eff} can be obtained using MARCATILI'S method described in Section 3.3. The process used to fabricate planar polymer waveguides leads to deviations from the ideally rectangular core shape. No analytical method is applicable to calculate the effective refractive indices of the propagating modes in such waveguides. Therefore, numerical optical simulation tools have to be employed to obtain the n_{eff} of the modes. The modes for the rectangular or arbitrarily shaped waveguides are assigned in descending sequence of their effective refractive index. Thereby, the fundamental mode exhibits the highest value and is assigned to the index $i = 1$.

8.3 Generic optical link

Based on a set of basic waveguide elements, one can build a generic optical link by concatenating several of these elements, see Figure 8.1. These basic elements can be, but are not limited to, straights, bendings, crossings, and mirrors. In a first step, the modal power coupling matrix \mathbf{K} of each individual element of the generic link needs to be characterized. One approach to characterize the modal power coupling matrix of a waveguide is described in Section 8.4.

The modal power distribution at the input-facet of the first waveguide element described by ${}_{in}\Phi_1$ which is equal to the input modal power distribution of the link, hence ${}_{in}\Phi_1 \equiv {}_{in}^{link}\Phi$. The output modal power distribution at the end of the link is described by ${}_{out}^{link}\Phi$, which is equal to the output modal power distribution of the N^{th} -waveguide element ${}_{out}\Phi_N$. The goal is to calculate the output modal power distribution ${}_{out}\Phi_N$ - the mode specific power assignment - of the N^{th} -waveguide element from the input modal power distribution of the first waveguide element ${}_{in}\Phi_1$. For a waveguide element n , the respective output modal power distribution ${}_{out}\Phi_n$ can then be calculated, according to Equation 8.5, as

$${}_{out}\Phi_n = \mathbf{K}_n \cdot {}_{in}\Phi_n \quad . \quad (8.6)$$

For ideally connected waveguide elements, the input modal power distribution ${}_{in}\Phi_{n+1}$ of the waveguide element $n + 1$, is equal to the output modal power distribution ${}_{out}\Phi_n$ of the previous waveguide element n . Therefore, the calculation for

the complete link yields

$$out \Phi_N = \mathbf{K}_N \cdot \dots \cdot \mathbf{K}_n \cdot \dots \cdot \mathbf{K}_1 \cdot in \Phi_1 \quad . \quad (8.7)$$

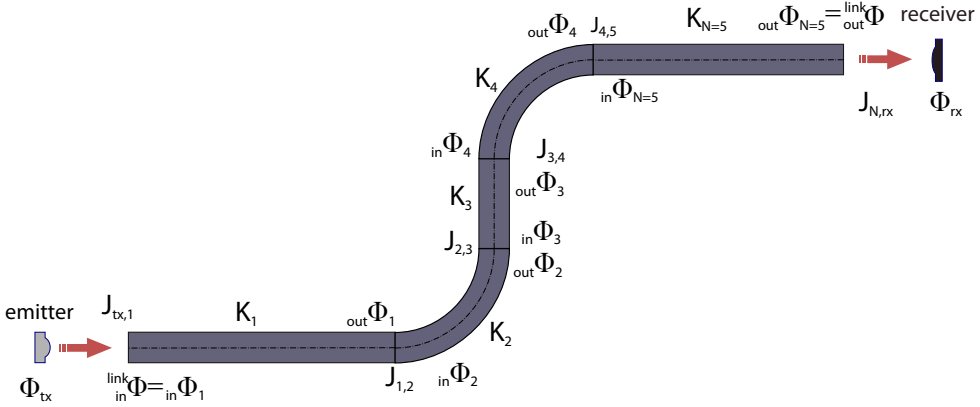


Figure 8.1: Generic optical link consisting of waveguide elements $n = 1 \dots N$, with the modal power distribution $in \Phi_1$ at the input facet of the first waveguide element, the respective modal power coupling matrices \mathbf{K}_n , the joint modal power coupling matrices $\mathbf{J}_{n,n+1}$, and the modal power distribution $out \Phi_N$ at the output facet.

Coupling of emitter and receiver

The input modal power distribution of the link $link_{in} \Phi$ is calculated using the modal power distribution of the emitter Φ_{tx} and the coupling matrix $\mathbf{J}_{tx,1}$ according to

$$link_{in} \Phi = in \Phi_1 = \mathbf{J}_{tx,1} \cdot \Phi_{tx} \quad . \quad (8.8)$$

The modal power distribution of the receiver Φ_{rx} can be calculated in a similar manner, by using the output modal power distribution of the link $link_{out} \Phi = out \Phi_N$ and the respective modal power coupling matrix $\mathbf{J}_{N,rx}$. An exemplary formalism to calculate the modal power distribution at the waveguide input facet generated by a VCSEL can be found in [69].

Imperfect waveguide connections

In certain applications, the connections between the waveguide elements of the generic optical link have to be considered as imperfect. Therefore, a modal power coupling at the connection has to be taken into account. This modal power coupling between the output modal power distribution of one $out \Phi_{n'}$ and the input modal power distribution $in \Phi_{n+1}$ of the subsequent waveguide element can be described as

$$in \Phi_{n+1} = \mathbf{J}_{n,n+1} \cdot out \Phi_n \quad , \quad (8.9)$$

in analogy to the modal power coupling in the waveguide element, described in Equation 8.6. Thereby, the modal power coupling at the waveguide connection is described by the 'joint' power coupling matrix \underline{J} . The lower indices of the matrix $\underline{J}_{n,n+1}$ indicate the connection between the waveguide element n and the subsequent element $n + 1$. The special case of an invariant modal power distribution between two waveguide elements and thus an ideal connection, leads to a joint power coupling matrix equivalent to the identity matrix, hence $\underline{J} = \underline{I}$.

Implementing Equation 8.6 and Equation 8.9 into a generic link with $n = 1 \dots N$ waveguide elements leads to

$${}_{out}\Phi_N = \mathbf{K}_N \cdot \mathbf{J}_{N-1,N} \cdot \mathbf{K}_{N-1} \cdot \dots \cdot \mathbf{K}_{n+1} \cdot \mathbf{J}_{n,n+1} \cdot \mathbf{K}_n \cdot \dots \cdot \mathbf{K}_2 \cdot \mathbf{J}_{1,2} \cdot \mathbf{K}_1 \cdot {}_{in}\Phi_1 \quad , \quad (8.10)$$

with their respective modal power coupling matrix \mathbf{K}_n and joint modal power coupling matrices $\mathbf{J}_{n,n+1}$. Thereby, the modal power distribution at the output of the last waveguide element is calculated for a specific modal power distribution at the input of the first waveguide element. A total of N modal power coupling matrices \mathbf{K} and $N - 1$ joint modal coupling matrices \mathbf{J} are sufficient to describe the mode propagation characteristic of the generic link.

8.4 Experimental approach

8.4.1 Method to determine the modal power coupling matrix \mathbf{K}

The ultimate goal will be a measurement procedure to determine the previously discussed modal power coupling matrix \mathbf{K} of a waveguide element. Herein proposed is an experimental approach to control the mode launch condition at the input of the waveguide element, the input modal power distribution ${}_{in}\Phi$. The controlled mode launch is one important part towards the characterization of the modal coupling matrix \mathbf{K} . The other important part is the analysis of the output modal power distribution ${}_{out}\Phi$ at the end of the waveguide element. Herein, two methods to analyze the modal power distribution are tested. They are used to verify the mode launch and are described in Section 8.4.3.

Equation 8.4 describes that each input mode ${}_{in}\phi_q$ contributes to a specific output mode ${}_{out}\phi_p$, according to the power coupling matrix coefficients $\kappa_{p,q}$. Consequently, by exciting only one mode with the power A according to

$${}_{in}\phi_i = \begin{cases} 0 & \text{for } i \neq q \\ A & \text{for } i = q \end{cases} \quad , \quad (8.11)$$

and measuring the power for each element $p = 1 \dots P$ of the output modal power distribution ${}_{out}\phi_p(q)$, the coupling matrix coefficients $\kappa_{p,q}$ can be determined as

$$\kappa_{p,q} = \frac{1}{A} \cdot {}_{out}\phi_p(q) \quad . \quad (8.12)$$

All coefficients of the power coupling matrix $\kappa_{p,q}$ are then obtained by sequentially launching the input modes $q = 1 \dots Q$ and measuring the respective modal power element p related to the launched mode q , e.g., $_{out}\phi_p(q)$.

8.4.2 Selective mode launch

A controlled, selective mode launch is required in order to excite one particular mode at the input facet of the waveguide. It is necessary that each mode can be excited individually. An optical mode represents a propagating electromagnetic field pattern in a waveguide. The modes themselves, and methods to calculate them, are in detail described in Chapter 3 for different types of waveguides. Controlled intensity and phase patterns I and φ , respectively, applied onto a coherent and linearly polarized plane wave, are herein used to construct the electromagnetic field pattern of the desired mode at the waveguide input facet.

Figure 8.2 (*top*) shows intensity \hat{I} and the phase φ of an optical field pattern in a waveguide in the x -axis and the xy -plane. Given a plane wave in propagation direction z , the intensity peaks are in phase. Thus, the electric field amplitude is given by $\hat{E} = \sqrt{\hat{I}}$, whereby both signals are time-varying. The image shows the situation of maximum electric field.

The goal is to reconstruct the electromagnetic field distribution of the mode from the intensity distribution. This also requires the according transversal phase of the electric field distribution. This can be achieved by applying a phase shift pattern of $\varphi = \pi$ to specific amplitude peaks, see Figure 8.2 (*bottom*). By applying this method, one can obtain electric field distributions, identical to the field distribution of an optical mode propagating in a waveguide.

A device which can spatially modulate arbitrary intensity and phase pattern is required to implement the proposed approach. Therefore, one amplitude and one phase modulating SLM (spatial light modulator) are used. These SLMs [41] are liquid crystal on silicon (LCoS) devices with 1920×1080 individually addressable pixels, operating in reflective mode. The HED-6010 (HOLOEYE) phase modulating display is based on a parallel aligned nematic (PAN) liquid crystal layer to apply a maximum phase shift $\varphi_{max} > 2\pi$ for each pixel. The vertically aligned nematic (VAN) liquid crystal in the HED-6001 (HOLOEYE) microdisplay causes a polarization tilt. The incoming light is linearly polarized in the vertical direction. After the SLM, the light has to pass a horizontally orientated polarizer, the analyzer. Only light which polarization is tilted by the SLM can pass it. The intensity of the light after the analyzer depends on the tilting angle of the polarization [33].

8.4.3 Mode analysis approach

A method to analyze the modal power distribution at the end-facet of the waveguide is required to verify the previously proposed selective mode launch.

8 Experiments on modal power coupling in waveguides

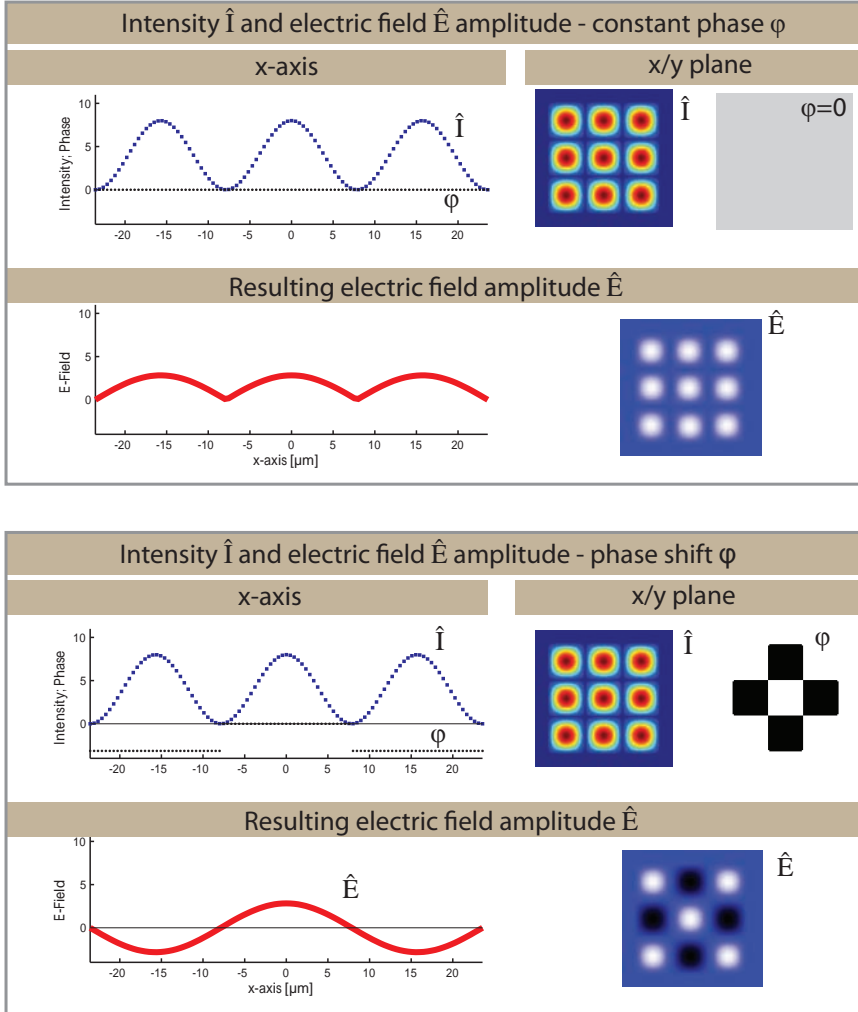


Figure 8.2: Intensity pattern \hat{I} and resulting electric-field amplitude \hat{E} , respectively, at constant phase (top), and the resulting electric amplitude \hat{E} in case of a π -phase shift according to the pattern φ (bottom).

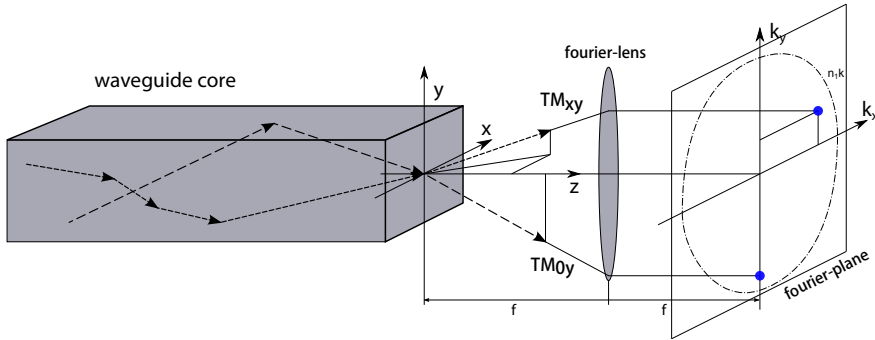


Figure 8.3: A lens, whose focal plane is placed at the waveguide end-facet, provides a Fourier-transformation of the emitting modes and, thus, leads to a spatial separation of the modes in the k_x - k_y -plane (Fourier-plane) according to their respective propagation vector components k_x and k_y [94, 28].

The first method used herein is an image of the intensity pattern at the waveguide end facet, taken by a CMOS camera, see Figure 8.4. This allows one to observe the output modal power distribution at the endfacet, if only one single mode is excited. If more than one mode is excited, interference is dominating the intensity pattern at the endfacet. However, the launch of an individual mode can be verified, but only if no modal power coupling occurs during propagation and thus no other modes are excited.

The second method tested herein is the optical Fourier transformation. It allows for a spatial separation of the propagating modes according to the propagation direction (k -vector) of their constituting plane waves. Modes, and their interpretation as propagating plane waves, have been described in Chapter 3. The idea is to overcome issues with modal interference by separating the modes. Optical simulations have shown that the transverse intensity distribution, for a propagation invariant modal intensity distribution, is variable along the propagation distance [28, 70].

The optical Fourier transformation is realized by a Fourier lens, whereby its foci are positioned on the waveguide facet and the observation plane, respectively [94]. The intensity distribution in the observation plane is detected by a CMOS detector placed in the respective plane. The position of the intensity spots in the observation plane, which represents the Fourier-plane, correlates directly with the transverse component of the k -vectors of the modes. Light propagating in modes with small transverse k -components, i.e., with a small angle between the k -vector and the z -axis, leads to intensity spots closer to the origin of the Fourier-plane (observation plane), see Figure 8.3. In contrast, modes with larger transverse k -components, the higher-order modes, are farther away from the origin of the Fourier-plane.

8.4.4 Optical setup

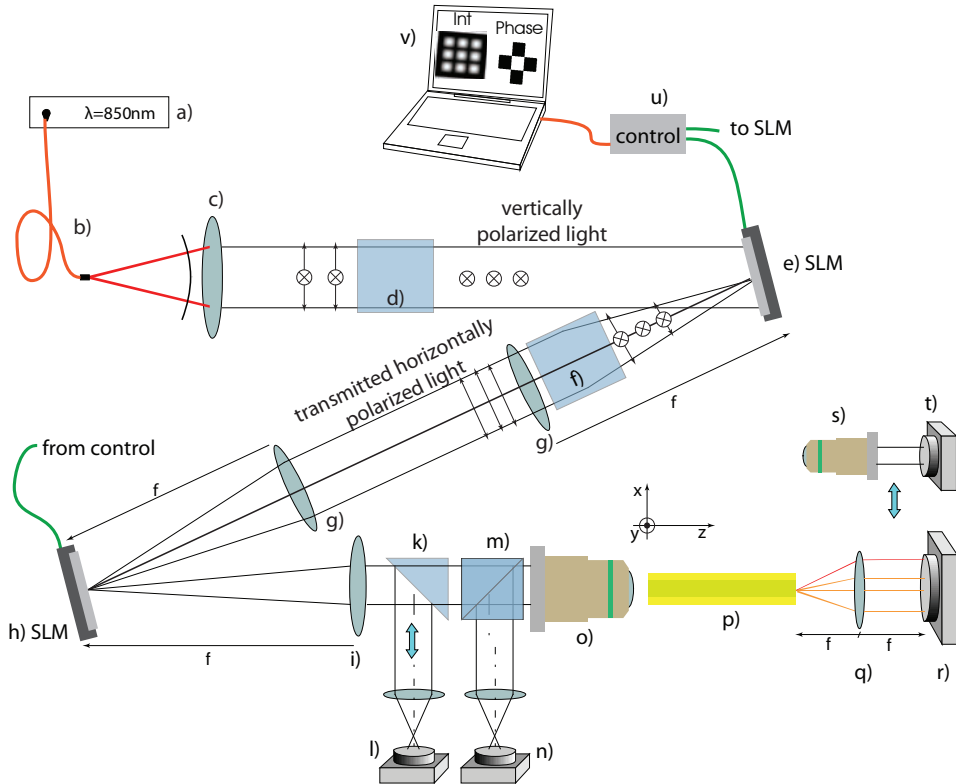
The optical setup used in this chapter is shown in Figure 8.4. A high-brightness LED module is used as the 850 nm wavelength light source (*a*) to illuminate the single mode fiber (*b*). The end facet of the fiber is placed in the focus of the collimating lens (*c*), resulting in a collimated beam. A polarizing beam splitter cube (*d*) is placed in the collimated beam, positioned such that only vertically polarized light can pass. The light then strikes the amplitude SLM (*e*) under an angle $\alpha/2 = 10^\circ$, with respect to the surface normal of the modulator. The polarization is tilted pixel by pixel, according to their respective gray scale value. Thereafter, another polarizing beam splitter cube (*f*) is used as analyzer with horizontal orientation. Light whose original vertical polarization is not altered is completely blocked by the analyzer. Thus, the off-state of a pixel leads to a black pixel.

The intensity pattern of the first SLM is imaged onto the second SLM by using two lenses ($f = 150$ mm) (*g*). Each of them has the focus placed exactly on the respective SLM, which leads to an image on the second SLM (*h*) with a magnification factor of one. This phase shift SLM adds a delay of $\varphi = \pi$ to the desired regions of the intensity pattern. Each microdisplay (SLM) is placed on a six-axis stage and the lenses (*g*) can be aligned in propagation direction.

The SLM control box (*u*) is connected to the computer (*v*) via a standard DVI cable and acts as external monitor. Each SLM (*e,h*) represents one of the color channels (red=amplitude, green=phase) of the RGB-signal, and is addressed by the control box. Accordingly, each pixel of the SLM microdisplay provides 8 bit dynamic range, e.g., gray scale values.

A microscope lens (*o*) (NIKON CFI60 40x) and the corresponding tube lens (*i*) (NIKON) provide a 40-times demagnification of the mode pattern on the SLM onto the waveguide (*p*) facet. A slideable 45° mirror (*k*) can be brought into the light path. In combination with an imaging lens and the CMOS camera (*l*), one can observe the intensity and phase pattern on the phase SLM (*h*). This is in particular required during the setup alignment procedure. The 50/50-beam splitter (*m*), in combination with an imaging lens and the inspection camera (*n*) allows to observe the reflected mode pattern on the waveguide input facet.

The Fourier imaging system consists of lens (*q*) in combination with the NIR enhanced CMOS camera (*r*) (EHD IMAGING), arranged according to Section 8.4.3. In order to capture real-space images of the waveguide endfacet, the Fourier imaging system can be replaced by an imaging system, which consists of the microscope lens (*s*) and a CMOS camera (*t*), in order to observe the waveguide end facet.



- | | |
|---|--|
| a) Light source ($\lambda=850\text{nm}$) LED or laser | m) 50/50 beam splitter cube |
| b) Single mode fiber | n) Camera to observe waveguide facet |
| c) Collimating lens | o) Microscope lens |
| d) Polarizer: polarizing beam splitter cube | p) Waveguide under test |
| e) Amplitude SLM | q) Fourier lens |
| f) Analyzer: polarizing beam splitter cube | r) Camera (sensor placed at fourier observation plane) |
| g) 4f-imaging lens | s) Microscope lens |
| h) Phase SLM | t) Camera to observe end facet (in lieu of fourier camera) |
| i) Tubus lens | u) SLM control box (HEO-1080P) |
| k) Tilted mirror (slideable) | v) Computer (DVI connection to SLM control box), inc. LabView based control software |
| l) Camera to observe SLM | |

Figure 8.4: Spatial light modulator (SLM) based optical setup to launch specific modes in the waveguide under test, and subsequent Fourier- and real- space imaging to analyze the modes at the end facet.

8.5 Experimental results

8.5.1 Selective mode launch in a step-index fiber

The goal of this experiment is to verify the selective mode launch setup. The idea is to use a waveguide with very few distortions. Thus, no significant excitation of other modes should occur during propagation in this waveguide. The modal power distribution at the waveguide output should be equivalent to the one at the input, $\Phi_{out} = \Phi_{in}$. Thus no modal power coupling is detectable. A step-index small-core-size glass-fiber (HPSC-fiber from J-FIBER) is used as low-distortion waveguide. This fiber type is based on very pure glass and provides a very smooth core-cladding interface - compared to the polymer waveguides. Both properties minimize scatter effects, which are one source of undesired modal power coupling. Compared to polymer waveguides, these fibers can be considered as practically ideal waveguides. This is indicated by the low loss of the glass fiber ($\Gamma_{fiber}^{\lambda=850nm} \approx 2 \times 10^{-3}$ dB/m), which is several magnitudes lower than the loss for a polymer waveguide ($\Gamma_{PWG}^{\lambda=850nm} \approx 5$ dB/m). Furthermore, straight fiber sections are used to avoid modal power coupling due to curved waveguides [69, 70].

The modal E -field pattern for the desired mode is calculated [7] and shown in Figure 8.5 (row *a*). Intensity I and phase φ are then generated on the two SLMs accordingly. The generated mode pattern can be observed by taking an image after the second SLM (row *b*). The images of the waveguide end-facet show distinctive intensity patterns which correlate to the respective launched mode patterns. No significant modal power coupling can be observed. These measurements show that an individual mode can be successfully launched in the step-index fiber. The mode propagates through the fiber and can be observed as modal intensity pattern at the end-facet of the fiber.

8.5.2 Variable mode launch in a polymer waveguide

Another method to control the mode launch makes use of a small light spot positioned on the input-facet of the waveguide. The power coupling efficiency from the light spot to the various modes depends strongly on the transversal position of the light spot in the waveguide core. For a light spot positioned in the center of the waveguide, the fundamental and lower-order modes will mostly be excited. Moving the light spot towards the boundary of the core enhances the coupling of optical power to modes with increasing order. Once the spot approaches the core-cladding interface, the modes of highest order in the respective k -direction are launched. Consequently, a spot placed in the corner of the core will preferably launch modes of highest k_x - and k_y -order [69].

Figure 8.6 shows the images of the Fourier-plane of the waveguide end-facet after a propagation length of 40 mm. The fundamental mode is expected to yield an intensity spot located in the center of the k -space. Modes of higher order, and thus

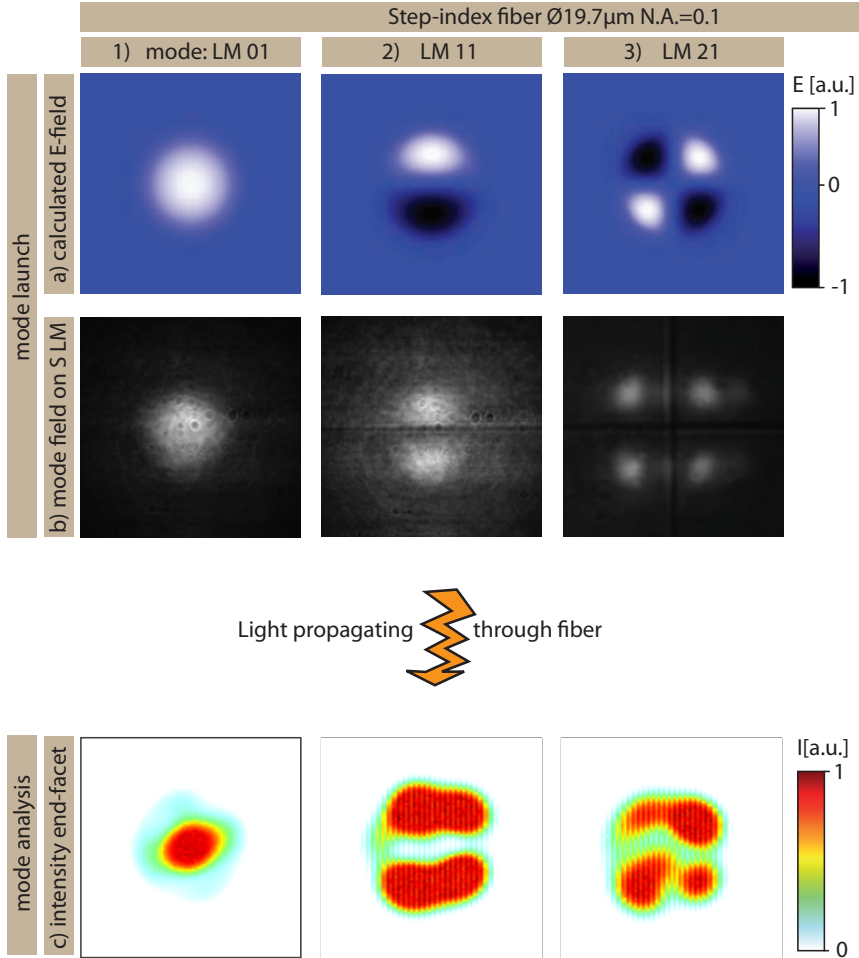


Figure 8.5: Mode propagation measurement of a $\varnothing 19.7\mu\text{m}$ step-index fiber stretch (length = 150 mm, N.A. = 0.1, straight). Modes LM 01, LM 11, and LM 21 (*columns 1-3*) are calculated (*row a*), generated with the SLMs (*row b*), launched at the input-facet, and observed at the end-facet (*row c*) of the fiber.

8 Experiments on modal power coupling in waveguides

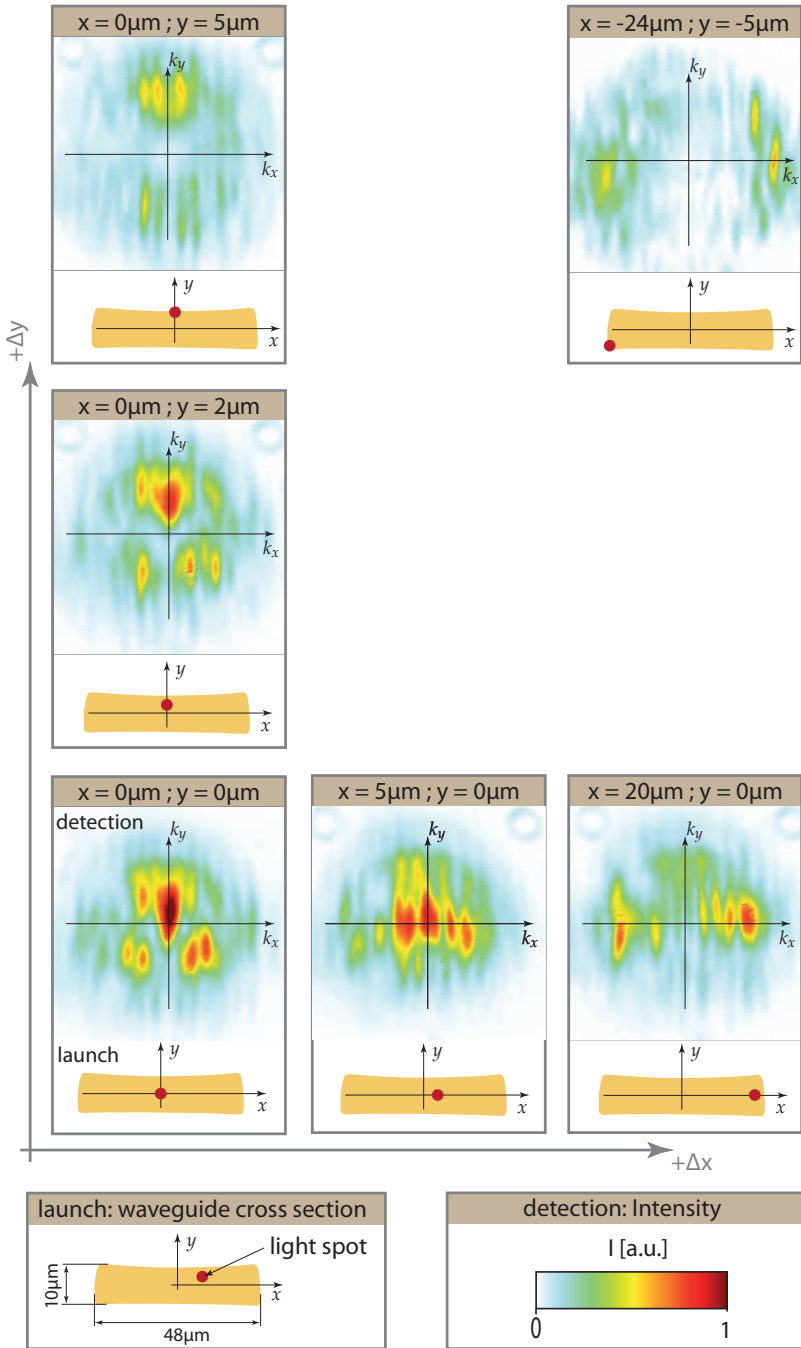


Figure 8.6: Small-spot based mode launch in a $48\ \mu\text{m} \times 10\ \mu\text{m}$ step-index polymer waveguide (length = 40 mm).

with higher propagation components k_x and k_y , are expected to yield intensity spots positioned at higher k_x - and k_y -values, accordingly.

The images in the bottom row of Figure 8.6 show, from left to right, intensity spots with increasing k_x -values, according to spot positions with higher x -values. In analogy, one can observe intensity spots with increasing k_y -values for spot positions with increasing y -values. These pictures are shown in the left column, from bottom to top, in Figure 8.6. The top-right image, with the light spot positioned at the corner of the core cross-section, leads to intensity spots in the k -space with highest k_x - and k_y -values. These observations demonstrate the correlation between the order of the excited modes and the intensity distribution detected in the Fourier plane.

Light carried in a mode is expected to yield an intensity spot in the Fourier-plane with a light intensity distribution similar to the sinc-function. This is due to the rectangular aperture of the waveguide. In addition, the spot would be dilated along the direction of the smaller waveguide aperture. In contrast, an infinitely extended plane wave would yield a diffraction limited spot. Since there are several excited modes present, the sinc-function patterns of the individual modes are overlapping and result in a distorted intensity pattern in the Fourier plane. This prevents a quantitative measurement of the modal intensity distribution. Nevertheless, the center of the intensity spot in each quadrant of the Fourier-plane indicates the expected position.

8.5.3 Limitations of the experimental setup

To fully determine the modal power coupling matrix K with a total of $P \cdot Q$ coupling coefficients κ , a total of $P \cdot Q$ measurement values have to be obtained. P and Q represent the number of output and input modes, respectively. The SLM based mode launch concept deployed herein allows to launch one specific mode at the time. In combination with a quantitative mode analysis setup, a total of Q coupling coefficients $\kappa_{p,q}$ can be measured while one specific mode ϕ_p is launched. Thus, the total number of P selective mode launches are required to complete the measurement. The number of modes P and Q can reach up to 1000 for the polymer waveguides of interest. However, an inherent advantage of the SLM mode launch is its capability for a straightforward automation of these measurements. With the used spatial light modulators, at a frame rate of 60 Hz, these measurements would require only tens of seconds, provided that the mode analysis can evaluate all output modes within 15 ms.

The pixel sizes of the spatial light modulators and the 40x-demagnification optics limits the N.A. for the waveguides to be tested. The number of pixels available to reproduce one intensity peak of the highest order modes can be calculated as about 10 for a rectangular waveguide with N.A.=0.3.

The accurate alignment in z -direction of the waveguide input-facet with the imaged mode field is in particular critical. An inspection camera which observes the alignment of the mode field directly on the waveguide facet could solve this issue.

An approach would be to use a pellicle beamsplitter (m) between tubus lens and microscope lens (Figure 8.4) to observe the facet directly through the microscope lens.

8.6 Potential applications

8.6.1 Loss prediction of an optical link

The proposed approach to characterize the optical properties of a waveguide by using the modal power coupling method bears the potential of an effective method to predict the insertion loss of a complete optical link, for any given input excitation. Furthermore, the influence of mechanical misalignment on the insertion loss in a waveguide connector can be evaluated. This is done by splitting it into two optical links connected by a joint power coupling matrix ${}^{conn}\mathbf{J}$, which represents the connector. Thus, the link can be calculated as ${}^{link}_{out}\Phi = \left[2\mathbf{K} \left[{}^{conn}\mathbf{J} \left[1\mathbf{K} \left[{}^{link}_{in}\Phi \right] \right] \right] \right]$. Thereby, variations in the alignment are described by variations in ${}^{conn}\mathbf{J}$, which directly influence the output modal power distribution ${}^{link}_{out}\Phi$ of the link.

8.6.2 Signal-level dependent propagation losses

The majority of optical interconnect applications implement multimode VCSELs as optical sender devices. The optical modes emitted from such a device depend strongly on the current in the laser cavity [112]. The commonly employed non-return-to-zero (NRZ) power modulation scheme uses a low- and a high-signal level. They correspond to the current levels I_{low}^{VCSEL} and I_{high}^{VCSEL} in the VCSEL. Thereby, the driving current for the low signal-level I_{low}^{VCSEL} , is always kept above the lasing threshold level. This is done to avoid turn-on jitter which negatively influences the signal integrity [112].

The different power levels lead to different modal power distributions of the VCSEL output for the different signal levels. The higher driving current in the laser cavity, required to obtain the optical power of the high-level state, leads to higher-order modes emitted by the VCSEL [112]. Consequently, higher-order modes are launched into the optical link when the VCSEL is coupled to the waveguide input facet. These higher-order modes are expected to exhibit a higher propagation loss Γ_{high} because they carry more optical power close to the core-cladding interface and thus are more susceptible to scattering at the dielectric interface. The expected higher propagation losses for the high-level signal Γ_{high} will lead to a reduced optical signal-swing. The signal-swing can be observed as vertical opening of the eye-diagram, which in turn is related to the signal quality of the data-link.

Consequently, in order to predict the signal integrity accurately, the propagation losses for the different modal power launching conditions corresponding to the low

(Γ_{low}) and the high signal-level (Γ_{high}) have to be taken into consideration for VCSEL based optical interconnect applications.

8.7 Summary

The modal power coupling matrix \mathbf{K} is herein used to describe the light propagation characteristic of multimode dielectric waveguides by means of the modal power transfer in the waveguide. Imperfections and straightness deviations of the waveguide inherently lead to power coupling between the propagating modes. The distribution of optical power carried in all modes is described by the modal power distribution vector Φ . The modal power distribution at the end of the waveguide can be calculated as the matrix product of the modal power coupling matrix and the input modal power distribution vector. This modal power coupling matrix approach can be applied to various waveguide types by using an appropriate mode conversion model. Basic mode conversion models are described for circular, rectangular, and arbitrary shaped dielectric step-index waveguides. The optical propagation characteristic of an optical link can be calculated as an arrangement of concatenated waveguide elements.

The capability to selectively launch individual modes in a waveguide is shown. The used optical setup is based on a sequential arrangement of an amplitude-modulating and a phase-modulating spatial light modulator. In particular, the fundamental and the lower-order modes of a step-index fiber were launched successfully. Since the straight fiber causes no significant modal power coupling, the intensity pattern of the launched mode could again be observed at the waveguide end-facet.

Experiments with a variable mode launch show the expected correlation between the order of the launched modes and the obtained intensity pattern in the Fourier plane. For lower-order modes, the intensity is concentrated at the center of the k -space. For launch conditions towards higher-order modes the intensity spots are located more towards higher k -values in the k -space. The current mode analysis setup is not yet capable of resolving the power guided in each individual mode.

9 Conclusions and outlook

This thesis describes a number of add-on technologies which, combined with the basic technology of embedded multimode polymer waveguides, result in a versatile toolbox to build cost-effective high-speed optical data links within future data processing systems.

These technologies are:

- An adjustment-free alignment technique provides a cost-effective method to connectorize the embedded polymer waveguides.
- A technology for embedding micro-mirrors within the polymer waveguide layer improves the versatility of the polymer waveguides by enabling sharp corners in the waveguides and by providing a means to vertically route the optical path.
- A measurement approach to accurately determine the propagation characteristics of simple multimode optical elements. The performance of complex multimode optical systems is then predicted by accumulating the measured propagation characteristics of the constituting simple elements.

In a separate section, the connectorization technology and the embedded micro-mirrors are demonstrated in an electro-optical flex board that can serve as basis for a compact electro-optical module. This module acts as transmitter or receiver for high-speed data transmission.

In the following paragraphs, a detailed conclusion and outlook will be presented on each of the above mentioned technologies and on the electro-optical flex board.

Passive alignment technique

The passive-alignment approach uses copper markers to provide both mechanical fiducials and optical alignment markers for the waveguides. Except for the laser-direct-writing tool - which is in any event required for the optical waveguide patterning - only processes compatible to PCB manufacturing are used to finally arrive at mechanical fiducials, precisely positioned with respect to the waveguides.

The adjustment-free assembly of an MT-compliant adapter onto the optical printed circuit board is successfully demonstrated. The offset between assembled ferrule and the waveguide axis exhibits a standard deviation of $\sigma_{off-axis} < 5 \mu\text{m}$. This position error corresponds to a misalignment induced coupling loss below the targeted 0.5 dB. Further process optimization could reduce the standard deviation of the positioning error even more. In particular the vertical dimension still leaves room for improvement. One can state that, the demonstrated adjustment-free assembly enables - by omitting extensive active alignment procedures - a cost-efficient method to precisely mount external components onto optical printed circuit boards. Hence, a technique is provided that allows to engage the accuracy demanding optics with the relatively coarse electrical PCB technology.

Embedded micro-mirrors

The development of embedded micro-mirrors, which are fabricated as integral part of the waveguide layer fabrication and enable an advanced waveguide routing, is further reported. These micro-mirrors consist of micro-structures with vertical or 45° tilted sidewalls, depending on whether in-plane or out-of-plane mirrors are intended. These micro-structures are selectively covered with a reflective layer, by using a selective metal plating process.

The developed selective wet-chemical metal-plating process applied on a planar substrate yields a gold layer reflectivity of $R_{Au} = 0.86$, see Section 6.4.3. This corresponds to almost 90% of the reflectivity of perfectly polished gold. Based on this convincing result and the applicability of the process for large-size substrate processing, this wet-chemical gold plating process to fabricate the reflective metal layer onto the micro-mirrors, is further pursued.

The UV-laser based structuring of bodies with vertical side-walls for in-plane micro-mirrors is a straightforward implementation of the laser-tool already used for waveguide patterning. Micro-structures with vertical sidewalls, which exhibit a surface roughness of $R_a=20$ nm - a value well below the $\lambda/20$ -criterion for optical grade surfaces - successfully demonstrate the applicability of the laser tool in combination with the custom acrylate resin. In contrast, the 45° tilted surfaces of the out-of-plane micro-mirrors exhibit a roughness of $R_a=270$ nm. This is caused by a cover glass required to protect the liquid acrylate resin from the immersion fluid below the coupling-prism of the laser head. To make the cover glass obsolete, a firm acrylate resin is required. This, since then the resin layer could be in direct contact with the immersion fluid. Therewith, tilted surfaces with an acceptable roughness have successfully been fabricated by structuring a firm polysilsesquioxane-based photosensitive resin.

The highest reflectivity achieved for a metal-plated micro-mirror is $R_{in-plane} \approx 0.5$. It is measured on an in-plane micro-mirror fabricated directly onto a polyimide substrate. The difference in reflectivity between this micro-mirror and the planar mirror ($R_{Au} = 0.86$) indicates different growth conditions for the two metal layers.

Another problem is posed by the chemical properties of the lower waveguide cladding. In-plane micro-mirrors, fabricated directly on a lower cladding, yield a reflectivity of $R_{in-plane} \approx 0.13$. Based on the significantly reduced reflectivity compared to an in-plane micro-mirror fabricated on an inert substrate, the following conclusion is drawn. The polyurethane cladding interacts chemically with the selective plating process and impedes the growth of a highly reflective metal layer. Unfortunately, none of the other investigated optical cladding materials, which would provide improved chemical resistance, provided enough adhesion for the acrylate resin. A comprehensive chemical investigation of the cladding material, the acrylate resin, the selective metal plating, and their interaction will be crucial to further improve the processability of the micro-mirrors.

In order to overcome the chemical influence of the lower cladding during the metal-plating process and to demonstrate actual in-plane and out-of-plane micro-mirrors embedded in a waveguide layer, the micro-mirrors are fabricated on an inert polyimide substrate and are then transferred onto the lower cladding. Based on this inert-substrate approach, micro-mirrors which exhibit reflectivity values of $R_{in-plane} = 0.5$ and $R_{out-of-plane} = 0.2$, for in-plane and out-of-plane micro-mirrors, respectively, are realized. These micro-mirrors, finally embedded in the waveguide layer stack, yield insertion losses of $\Gamma_{in-plane} = 5.5$ dB and $\Gamma_{out-of-plane} = 7$ dB for in-plane and out-of-plane micro-mirrors, respectively. The origins of these loss values are deviations from the ideal waveguide-mirror structure and the aforementioned reflectivity values.

Based on the presented work, three main challenges are identified towards the aim of embedded micro-mirrors with an improved optical performance. First, the issues with the laser-direct-writing of the out-of-plane micro-mirrors could be solved by using a photosensitive resin layer which is firm during the UV exposure, but which still provides the chemical selectivity that is required for the selective metal plating process. Then, only a film of immersion fluid is required between the prism of the laser-head and the photosensitive resin. No coated cover glass impedes the laser beam. Second, the adhesion of the micro-structures on chemically resistant cladding materials (e.g. polysilsesquioxanes) needs to be improved. This involves changes in the resin chemistry and, most probably, also an adjustment of the cladding material itself. Finally, the chemistry of the selective metal-plating process of micro-structures on a cladding needs to be understood and eventually optimized.

This research work on the acrylate resin, the micro-structure patterning, and the selective metal-plating process provides convincing results to further investigate this embedded micro-mirror approach. Therefore, exploring the chemical interaction between the cladding-material, the photosensitive resin, and the selective metal-plating process are indispensable.

Electro-optical flex board

The applicability of the aforementioned integrated micro-mirrors is demonstrated by means of the electro-optical flex board. The embedded out-of-plane micro-mirror enables thereby a very compact vertical light-coupling configuration. The opto-electronic device will be placed directly on the electrical traces on top of the upper cladding. This simple configuration allows to optically couple the optoelectronic device to the waveguide without the need for additional optical elements, i.e., lenses. Additionally, the aforementioned passive-alignment concept is implemented in this flex-assembly to enable an efficient assembly of the optical connector.

The demonstrated electro-optical flex board provides the basis for compact optical transmitter and receiver modules. This approach benefits from the compact integration of the opto-electronic device by using the embedded micro-mirrors. The very dense electrical connection allows for an on-package placement in close vicinity

to the processor. Therefore, additional off-package data channels are provided in order to overcome the expected data communication bottleneck between processor laminate and PCB. Additionally, the high degree of compatibility to standard PCB manufacturing and to the existing polymer waveguide technology is advantageous for future large-scale production.

Propagation characteristic of multimode waveguides

In the final part of this work, an experimental method to determine the mode propagation characteristic of waveguides is investigated. This requires the launch of specific mode patterns at the waveguide input-facet and the analysis of the modal power distribution at the output-facet. The mode pattern for the selective mode launch is controlled by means of two spatial light modulators. They modulate the amplitude and the phase of the incident plane wave in order to construct the desired mode pattern (Section 8.4.2). Herein pursued is an approach to analyze the modal power distribution at the output of the waveguide by separating them according to their k -vector directions. This separation is performed by an optical Fourier transformation as described in Section 8.4.3.

By using the proposed approach, the selective launch of individual lower order modes has qualitatively been demonstrated in step index glass fibers. The low N.A., and thus the low number of modes, and the absence of modal power coupling allow for a simple distinction of the mode patterns imaged at the fiber end-facet.

In contrast, experiments on launching modes in rectangular polymer waveguides turned out to be far more critical and the obtained results are less significant. The relatively high N.A. of the polymer waveguides, compared to the aforementioned step index glass fibers, leads to a high number of modes. The resolution of the current optical setup is not yet sufficient to accurately enough reproduce the required mode patterns.

Experiments with the small-spot-launch approach qualitatively demonstrate the correlation between the order of the excited modes and the detected intensity distribution in the k -space.

To eventually determine the proposed modal power coupling matrix K of the waveguide, the currently qualitative modal power distribution measurements need to be quantified. The presented mode characterization setup with mode launch and mode detection, is applicable for waveguides with a low numerical aperture of up to N.A.=0.1 and a cross-sectional dimension of up to 20 μm .

An additional application for the discussed mode propagation characteristic, besides the aforementioned performance prediction, is a method for advanced process controlability. Process deviations, such as the roughness of the waveguide core sidewall, are expected to exhibit a unique fingerprint in the modal power coupling matrix K of the respective waveguide. The reason is, that not only the conventionally measured amount of propagated light is obtained, but rather the multi-dimensional propagation characteristic of the waveguide.

Bibliography

- [1] E. Anzures, R. Dangel, R. Beyeler, A. Cannon, F. Horst, C. Kiarie, P. Knudsen, N. Meier, M. Moynihan, and B. J. Offrein. Flexible optical interconnects based on silicon-containing polymers. In *Proceedings of SPIE: Photonics Packaging, Integration, and Interconnects IX*, volume 7221, page 72210I, San Jose, USA, Feb. 2009. 11, 65, 72
- [2] C. Berger. Optical interconnect demonstrator with embedded waveguides and butt-coupled optoelectronic modules. In *Adaptive Optics: Analysis and Methods / Computational Optical Sensing and Imaging / Information Photonics / Signal Recovery and Synthesis*, page IWD2, Charlotte, U.S.A., June 2005. xii, xiv, xvi
- [3] C. Berger, L. Dellmann, P. Dill, F. Horst, B. J. Offrein, M. Schmatz, S. Oggioni, M. Spreafico, and G. Macario. Integration of optical I/O with organic chip packages. In *Proceedings of the SPIE: Photonics Packaging, Integration, and Interconnects VIII*, volume 6899, pages 689912–689912–9, San Jose, USA, Feb. 2008. 4, 5
- [4] C. Berger, B. J. Offrein, and M. Schmatz. Challenges for the introduction of board-level optical interconnect technology into product development roadmaps. In *Proceedings of the SPIE: Optoelectronic Integrated Circuits VIII*, volume 6124, pages 144–155, San Jose, USA, Feb. 2006. 6
- [5] T. Bierhoff. *Strahlenoptische Analyse der Wellenausbreitung und Modenkopplung in optisch hoch multimodalen Wellenleitern*. PhD thesis, Universität Paderborn, Deutschland, 2007. 6, 94
- [6] S. L. Brandow, M. S. Chen, R. Aggarwal, C. S. Dulcey, J. M. Calvert, and W. J. Dressick. Fabrication of patterned amine reactivity templates using 4-chloromethylphenylsiloxane self-assembled monolayer films. *Langmuir*, 15(16):5429–5432, 1999. 55
- [7] J. A. Buck. *Fundamentals of Optical Fibers*. Wiley, New Jersey, 2nd edition, 2004. 26, 28, 106
- [8] R. T. Chen and C. Choi. Optical interconnects. *Synthesis Lectures on Solid State Materials and Devices*, 2(1):1–104, 2007. 6
- [9] T. C. Chen. Research directions for nano-scale science and technology. In *Advanced Materials and Technologies for Nano and Oxide Electronics*, New Delhi, India, Feb. 2007. 3
- [10] T. C. Chen. Research challenges for cmos scaling: Industry directions. In *International Conference on Frontiers of Characterization and Metrology for Nanoelectronics*, Albany, U.S.A., 2009. 2
- [11] C. Choi, L. Lin, Y. Liu, J. Choi, L. Wang, D. Haas, J. Magera, and R. T. Chen. Flexible optical waveguide film fabrications and optoelectronic devices integration for fully embedded board-level optical interconnects. *Journal of Lightwave Technology*, 22(9):2168–2176, 2004. 11, 43
- [12] J. H. Choi, L. Wang, H. Bi, and R. T. Chen. Effects of thermal-via structures on thin-film VCSELs for fully embedded board-level optical interconnection system. *IEEE Journal of Selected Topics in Quantum Electronics*, 12(5):1060–1065, 2006. 6
- [13] R. Dangel, U. Bapst, C. Berger, R. Beyeler, L. Dellmann, F. Horst, B. J. Offrein, and G.-L. Bona. Development of a low-cost low-loss polymer waveguide technology for parallel optical interconnect applications. In *Biophotonics/Optical Interconnects and VLSI Photonics/WBM Microcavities, Digest of the LEOS Summer Topical Meetings*, page 2, June 2004. 6
- [14] R. Dangel, C. Berger, R. Beyeler, L. Dellmann, M. Gmür, R. Hamelin, F. Horst, T. Lamprecht, T. Morf, S. Oggioni, M. Spreafico, and B. J. Offrein. Polymer-waveguide-based board-level optical interconnect technology for datacom applications. *IEEE Transactions on Advanced Packaging*, 31(4):759–767, Nov. 2008. xii, xiv, xvi, 6, 45
- [15] R. Dangel, C. Berger, R. Beyeler, L. Dellmann, F. Horst, T. Lamprecht, N. Meier, and B. J. Offrein. Prospects of a polymer-waveguide-based board-level optical interconnect technology. In *IEEE Workshop on Signal Propagation on Interconnects*, pages 131–134, Ruta di Camogli, Italy, May 2007. 11, 64

Bibliography

- [16] R. Dangel, R. Beyeler, F. Horst, N. Meier, B. J. Offrein, B. Sicard, M. Moynihan, P. Knudsen, and E. Anzures. Waveguide technology development based on temperature- and humidity-resistant low-loss silsesquioxane polymer for optical interconnects. In *Conference on Optical Fiber Communication and the National Fiber Optic Engineers Conference OFC/NFOEC*, page OThH2, Anaheim, U.S.A., 2007. 11, 12, 13
- [17] R. Dangel, F. Horst, T. Lamprecht, and B. J. Offrein. Coupling device for use in optical waveguides, US 7672560, 2010. 41
- [18] R. Dangel, F. Horst, T. Lamprecht, B. J. Offrein, and M. Gmür. Flexible polymer waveguides as cost-efficient, high-density capable, and versatile technology for board-to-board and on-board optical interconnects. In *Microoptics Conference MOC*, Brussels, Belgium, 2008. 47
- [19] R. Dangel and T. Lamprecht. Methods for passive micrometer-range alignment of components using removable reference structures, US 7382954, 2008. 31
- [20] C. Debaes, M. Vervaeke, V. Baukens, H. Ottevaere, P. Vynck, P. Tuteleers, B. Volckaerts, W. Meeus, M. Brunfaut, J. Van Campenhout, A. Hermanne, and H. Thienpont. Low-cost microoptical modules for MCM level optical interconnections. *IEEE Journal of Selected Topics in Quantum Electronics*, 9(2):518–530, 2003. 43
- [21] L. Dellmann, T. Lamprecht, S. Oggioni, M. Witzig, R. Dangel, R. Beyeler, C. Berger, F. Horst, and B. J. Offrein. Butt-coupled optoelectronic modules for high-speed optical interconnects. In *Conference on Lasers and Electro-Optics Europe, CLEO*, page 476, Munich, Germany, June 2005. 34, 38
- [22] F. E. Doany, C. L. Schow, C. Baks, R. Budd, Y.-J. Chang, P. Pepeljugoski, L. Schares, D. Kuchta, R. John, J. A. Kash, F. Libsch, R. Dangel, F. Horst, and B. J. Offrein. 160-Gb/s bidirectional parallel optical transceiver module for board-level interconnects using a Single-Chip CMOS IC. In *57th Electronic Components and Technology Conference, ECTC*, pages 1256–1261, Reno, U.S.A., 2007. xii, xiv, xvi, 47
- [23] F. E. Doany, C. L. Schow, R. Budd, C. Baks, D. M. Kuchta, P. Pepeljugoski, J. A. Kash, F. Libsch, R. Dangel, F. Horst, and B. J. Offrein. Chip-to-chip board-level optical data buses. In *Conference on Optical Fiber Communication and National Fiber Optic Engineers Conference, OFC/NFOEC 2008*, page OThS4, San Diego, U.S.A, Feb. 2008. 43
- [24] W. J. Dressick, C. S. Dulcey, J. Jacque H. Georger, G. S. Calabrese, and J. M. Calvert. Covalent binding of Pd catalysts to ligating self-assembled monolayer films for selective electroless metal deposition. *Journal of The Electrochemical Society*, 141(1):210–220, 1994. 55
- [25] L. A. Eldada. Polymer integrated optics: promise versus practicality. In *Proceedings of SPIE: Organic Photonic Materials and Devices IV*, volume 4642, pages 11–22, June 2002. 11
- [26] L. A. Eldada. Advances in polymer optical interconnects. In *The 18th Annual Meeting of the IEEE Lasers and Electro-Optics Society*, pages 361–362, Sydney, Australia, 2005. 6
- [27] Enthone. *Immersion Gold I - Stromloser Goldelektrolyt*. 56
- [28] D. Erni, D. Lenz, J.-M. Lehky, B. J. Offrein, and T. Lamprecht. Upgrading multimode channels for multi-tb/s/inch bandwidth densities in board-level optical interconnects. *European Microwave Association Proceedings (EuMA Proc.), Special Issue on Microwave Photonics*, 3(3):222–228, 2007. 103
- [29] R. Farrer, C. LaFratta, L. Li, J. Praino, M. Naughton, B. Saleh, M. Teich, and J. Fourkas. Selective functionalization of 3-d polymer microstructures. *Journal of the American Chemical Society*, 128(6):1796–1797, Jan. 2006. 53, 54, 72
- [30] S. B. Fuller. A fast flexible ink-jet printing method for patterning networks of neurons in culture. Master's thesis, Massachusetts Institute of Technology, Cambridge, U.S.A., 2003. 87
- [31] S. B. Fuller, E. J. Wilhelm, and J. M. Jacobson. Ink-jet printed nanoparticle microelectromechanical systems. *Journal of Microelectromechanical Systems*, 11(1):54–60, 2002. 87
- [32] A. L. Glebov, M. G. Lee, and K. Yokouchi. Integration technologies for pluggable backplane optical interconnect systems. *Optical Engineering*, 46(1):015403, 2007. 6
- [33] E. Hecht. *Optik*. Oldenbourg, München, 4. edition, 2001. 16, 97, 101
- [34] N. Hendrickx. *Multilayer Optical Interconnections Integrated on a Printed Circuit Board*. PhD thesis, Ghent University, 2009. 6

- [35] N. Hendrickx, H. Suyal, G. Van Steenberge, A. McCarthy, A. Walker, H. Ottevaere, H. Thienpont, M. Taghizadeh, P. Van Daele, T. Pustelny, P. V. Lambeck, and C. Gorecki. Laser ablation and laser direct writing as enabling technologies for the definition of micro-optical elements. In *SPIE Proceedings of Integrated Optics: Theory and Applications*, volume 5956, pages 59561B–10, Warsaw, Poland, 2005. 11, 43
- [36] N. Hendrickx, J. Van Erps, G. Van Steenberge, H. Thienpont, and P. Van Daele. Tolerance analysis for multilayer optical interconnections integrated on a printed circuit board. *Journal of Lightwave Technology*, 25(9):2395–2401, 2007. 6
- [37] N. Hendrickx, G. Van Steenberge, P. Geerinck, J. Van Erps, H. Thienpont, and P. Van Daele. Laser-ablated coupling structures for stacked optical interconnections on printed circuit boards. In *Proceedings of SPIE: Micro-Optics, VCSELs, and Photonic Interconnects II: Fabrication, Packaging, and Integration*, volume 6185, pages 618503–9, Strasbourg, France, Apr. 2006. 43
- [38] A. Henry, T. Tutt, M. Galloway, Y. Davidson, C. McWhorter, S. Soper, and R. McCarley. Surface modification of poly(methyl methacrylate) used in the fabrication of microanalytical devices. *Analytical Chemistry*, 72(21):5331–5337, Nov. 2000. 53
- [39] S. Hiramatsu and M. Kinoshita. Three-dimensional waveguide arrays for coupling between fiber-optic connectors and surface-mounted optoelectronic devices. *Journal of Lightwave Technology*, 23(9):2733–2738, 2005. 43
- [40] X. Hoa, M. Martin, A. Jimenez, J. Beauvais, P. Charette, A. Kirk, and M. Tabrizian. Fabrication and characterization of functionalized nano-gratings for enhanced spr biosensing. In *Nanobioeurope*, Barcelona, Spain, June 2008. 53
- [41] Holoeye. www.holoeye.com. 101
- [42] W. Huang and J. Mu. Complex coupled-mode theory for optical waveguides. *Optics Express*, 17(21):19134–19152, Oct. 2009. 95
- [43] K. Iizuka. *Elements of Photonics, Volume II: For Fiber and Integrated Optics*. John Wiley & Sons, Inc., New York, 1st edition, 2002. 16, 17, 19, 21
- [44] IPtronics. www.iptronics.com. 88
- [45] ITRS. Executive summary 2007 edition. www.itrs.net, 2007. International Technology Roadmap for Semiconductors. 3, 4, 5, 42
- [46] R. Jackson. Initiation of electroless copper plating using pd+2/poly(acrylic acid) films. *Journal of The Electrochemical Society*, 135(12):3172–3173, 1988. 55
- [47] R. Jackson. Pd+2/poly(acrylic acid) thin films as catalysts for electroless copper deposition: Mechanism of catalyst formation. *Journal of The Electrochemical Society*, 137(1):95–101, Jan. 1990. 55
- [48] K. Johal, H. Roberts, S. Lamprecht, and C. Wunderlich. Electroless nickel / immersion gold process technology for improved ductility of flex and rigid-flex applications. In *SMTA Pan-Pacific Microelectronics Symposium*, Kauai, Hawaii U.S.A., Jan. 2005. 50, 55
- [49] J. Jütz. Technische optik TOP. Lecture FH NTB Buchs, 2000. 21
- [50] D. Jubin, R. Dangel, N. Meier, F. Horst, T. Lamprecht, J. Weiss, R. Beyeler, B. J. Offrein, M. Halter, and F. Betschon. Multi-layer waveguide optical connector. In *Proceedings of Optics in Computing*, Vienna, Austria, 2009. 89
- [51] D. Jubin, R. Dangel, N. Meier, F. Horst, T. Lamprecht, J. Weiss, R. Beyeler, B. J. Offrein, M. Halter, R. Stieger, and F. Betschon. Polymer waveguide-based multilayer optical connector. In *Proceedings of SPIE Optoelectronic Interconnects and Component Integration IX*, volume 7607, pages 76070K–9, San Francisco, California, USA, Feb. 2010. 6, 39, 84, 88, 89
- [52] M. Karppinen, J. Makinen, K. Kataja, A. Tanskanen, T. Alajoki, P. Karioja, M. Immonen, and J. Kivilahti. Embedded optical interconnect on printed wiring board. In *Proceedings of the SPIE: Micro-Optics, VCSELs, and Photonic Interconnects*, volume 5453, pages 150–164, Sept. 2004. xii, xiv, xvi, 6
- [53] J. A. Kash, P. Pepeljugoski, F. E. Doany, C. L. Schow, D. M. Kuchta, L. Schares, R. Budd, F. Libsch, R. Dangel, F. Horst, B. J. Offrein, Y. Vlasov, W. Green, F. Xia, C. W. Baks, Y. H. Kwark, D. G. Kam, and M. B. Ritter. Communication technologies for exascale systems. In *Proceedings of SPIE: Photonics*

Bibliography

- Packaging, Integration, and Interconnects IX*, volume 7221, pages 72210F–12, San Jose, USA, Feb. 2009. 6
- [54] K. Kawano and T. Kitoh. *Introduction to Optical Waveguide Analysis: Solving Maxwell's Equations and the Schrödinger Equation*. John Wiley & Sons, New York, 2001. 22, 23, 24
- [55] J.-J. Kim and J.-S. Kim. Polymeric multimode waveguide arrays for one- and two-dimensional optical interconnects. In *Proceedings of SPIE: Linear and Nonlinear Optics of Organic Materials IV*, volume 5517, pages 141–151, Denver, USA, 2004. 43
- [56] J.-S. Kim and J.-J. Kim. Stacked polymeric multimode waveguide arrays for two-dimensional optical interconnects. *IEEE Journal of Lightwave Technology*, 22(3):840–844, Mar. 2004. 6, 43
- [57] M. Kondo, C. Esposito, M. Imanari, M. Nomura, K. Arao, T. Kanda, and S. Tsukagoshi. Photoimageable auto-catalytic resin metallization as an alternative to sputtering. In *29th International Electronics Manufacturing Technology Symposium, IEEE/CPMT/SEMI*, pages 238–241, San Jose, U.S.A., July 2004. 87
- [58] S. Kopetz, D. Cai, E. Rabe, and A. Neyer. PDMS-based optical waveguide layer for integration in electrical-optical circuit boards. *AEU - International Journal of Electronics and Communications*, 61(3):163–167, Mar. 2007. 6
- [59] T. Lamprecht, R. Beyeler, R. Dangel, F. Horst, D. Jubin, N. Meier, J. Weiss, and B. J. Offrein. Integrated micro-mirrors for compact routing of optical polymer waveguides. In *LEOS Annual Meeting Conference Proceedings*, pages 20–21, Belek-Antalya, Turkey, Oct. 2009. 49
- [60] T. Lamprecht and R. Dangel. Method to fabricate equipment for accuracy inspection of opto-mechanical connectors, Oct 2008. IPCOM 000175240D. 37
- [61] T. Lamprecht, R. Dangel, and F. Horst. Mechanically decoupled opto-mechanical connector for flexible optical waveguides embedded and/or attached to a printed circuit board, US 7389015, 2008. 89
- [62] T. Lamprecht, R. Dangel, and F. Horst. Mechanically decoupled opto-mechanical connector for flexible optical waveguides embedded and/or attached to a printed circuit board, US 7454098, 2008. 31
- [63] T. Lamprecht, R. Dangel, and F. Horst. Mechanically decoupled opto-mechanical connector for flexible optical waveguides embedded and attached to a printed circuit board, US 7794561, 2010. 31
- [64] T. Lamprecht, R. Dangel, F. Horst, and B. J. Offrein. Optical waveguide with embedded light reflecting feature and method for fabricating the same, WO/2010/116291, pending. 41
- [65] T. Lamprecht, F. Horst, R. Dangel, R. Beyeler, N. Meier, L. Dellmann, M. Gmür, C. Berger, and B. J. Offrein. Passive alignment of optical elements in a printed circuit board. In *In Proceedings of the Electronic Components and Technology Conference, 56th ECTC*, pages 761–767, San Diego, U.S.A., May 2006. 31, 37
- [66] G. Langer and M. Riester. Two-photon absorption for the realization of optical waveguides on printed circuit boards. In Y. Sidorin and C. A. Waechter, editors, *Proceedings of SPIE: Integrated optics: devices, materials, and technologies XI*, volume 6475, pages 64750X.1–64750X.9. SPIE, 2007. 11
- [67] K. Y. Lee, N. LaBianca, S. A. Rishton, S. Zolgharnain, J. D. Gelorme, J. Shaw, and T. H.-P. Chang. Micromachining applications of a high resolution ultrathick photoresist. In *The 38th International symposium on electron, ion, and photon beams*, volume 13, pages 3012–3016, Scottsdale, Arizona (USA), Nov. 1995. AVS. 52
- [68] J.-M. Lehky, D. Erni, F. Robin, L. Dellmann, G.-L. Bona, P. Straub, and W. Bächtold. Optical waveguides for backplane communication using metal film ion-exchange in glass. In ., editor, *European Conference on Integrated Optics*, pages 526–529, Grenoble, France, 2005. 11
- [69] D. Lenz. *Modeling of highly multimodal optical communication systems*. PhD thesis, ETHZ Swiss Federal Institute of Technology Zurich, 2006. 7, 94, 95, 96, 99, 106
- [70] D. Lenz, D. Erni, and W. Bächtold. Quasi-analytic formalism for mode characteristics in highly overmoded rectangular dielectric waveguide bends. *Journal of the Optical Society of America A*, 22(9):1968–1975, 2005. 103, 106

- [71] B. E. Little and W. P. Huang. Coupled-mode theory for optical waveguides. In *Progress in Electromagnetic Research, PIER*, volume 10, pages 217–270, 1995. 95
- [72] H. Lorenz, M. Despont, N. Fahrni, N. LaBianca, P. Renaud, and P. Vettiger. SU-8: a low-cost negative resist for MEMS. *Journal of Micromechanics and Microengineering*, 7(3):121–124, 1997. 52
- [73] H. Ma, A. K. Y. Jen, and L. R. Dalton. Polymer-based optical waveguides: Materials, processing, and devices. *Advanced Materials*, 14(19):1339–1365, 2002. 6, 11
- [74] G. O. Mallory and J. B. Hajdu. *Electroless plating: fundamentals and applications*. Noyes Publications, New York, 1990. ISBN 978-0-936569-07-9. 50, 55
- [75] E. A. Marcatili. Dielectric rectangular waveguide and directional coupler for integrated optics. *Bell System Technical Journal*, 48(21):2071–2102, 1969. 22, 23
- [76] D. Marcuse. *Light transmission optics*. Krieger Publishing, Florida, 1st edition, 1989. 95
- [77] D. Marcuse. *Theory of dielectric optical waveguides*. Academic Press, Inc., New York, 2nd edition, 1991. 95
- [78] R. J. Martin-Palma, M. Manso, J. Perez-Rigueiro, J. P. Garcia-Ruiz, and J. M. Martinez-Duart. Surface biofunctionalization of materials by amine groups. *Journal of Materials Research*, 19(8):2415–2420, 2004. 53
- [79] D. A. B. Miller. Physical reasons for optical interconnection. *International Journal of Optoelectronics*, 11(3):155–168, 1997. xii, xiv, xvi, 3
- [80] D. A. B. Miller. Fundamental limit for optical components. *Journal of the Optical Society of America B*, 24(10):A1–A18, Oct. 2007. xii, xiv, xvi
- [81] D. A. B. Miller. Device requirements for optical interconnects to silicon chips. *Proceedings of the IEEE*, 97(7):1166 – 1185, 2009. 4, 6
- [82] J. Moisel, J. Guttmann, H.-P. Huber, O. Krumpholz, M. Rode, R. Bogenberger, and K.-P. Kuhn. Optical backplanes with integrated polymer waveguides. *Optical Engineering*, 39(3):673–679, Mar. 2000. 6
- [83] G. E. Moore. Cramming more components onto integrated circuits. *Electronics*, 38(8), Apr. 1965. 2
- [84] S. Nakagawa, D. Kuchta, C. Schow, R. John, L. A. Coldren, and Y. C. Chang. 1.5mW/Gbps low power optical interconnect transmitter exploiting High-Efficiency VCSEL and CMOS driver. In *Optical Fiber Communication Conference and Exposition and The National Fiber Optic Engineers Conference*, OSA Technical Digest (CD), page OThS3, San Diego, U.S.A., Feb. 2008. 6
- [85] A. Neyer, E. Rabe, S. Kopetz, D. Zhu, and D. Cai. Large-area replication technology for the production of electrical-optical circuit boards (EOCB). In *2007 Digest of the IEEE/LEOS Summer Topical Meetings*, pages 127–128, Portland, OR, USA, July 2007. 6
- [86] L. H. Nguyen, M. Straub, and M. Gu. Acrylate-based photopolymer for two-photon microfabrication and photonic applications. *Advanced Functional Materials*, 15(2):209–216, 2005. 11
- [87] B. J. Offrein, C. Berger, R. Beyeler, R. Dangel, L. Dellmann, F. Horst, T. Lamprecht, N. Meier, R. Budd, F. Libsch, and J. Kash. Parallel optical interconnects in printed circuit boards. In *Proceedings of the SPIE: Optically Based Materials and Optically Based Biological and Chemical Sensing for Defence II*, volume 5990, pages 117–125, Oct. 2005. 6
- [88] E. Palik, editor. *Handbook of Optical Constants of Solids I*. Academic Press Inc., New York, June 1985. 56, 59, 61
- [89] I. Papakonstantinou, K. Wang, D. R. Selviah, and F. A. Fernández. Transition, radiation and propagation loss in polymer multimode waveguide bends. *Optics Express*, 15(2):669, Jan 2007. 97
- [90] I. Park, Z. Li, A. P. Pisano, and R. S. Williams. Selective surface functionalization of silicon nanowires via nanoscale joule heating. *Nano Letters*, 7(10):3106–3111, Oct. 2007. 53
- [91] P. K. Pepeljugoski and D. M. Kuchta. Design of optical communications data links. *IBM Journal of Research and Development*, 47(2):223–237, Mar. 2003. 11
- [92] E. Rabe, S. Kopetz, and A. Neyer. The generation of mould patterns for multimode optical waveguide components by direct laser writing of SU-8 at 364 nm. *Journal of Micromechanics and Microengineering*, 17(8):1664–1670, July 2007. 6, 11

Bibliography

- [93] W. Riedel. *Electroless Nickel Plating*. Finishing Publications Ltd & ASM International, Dec. 1991. ISBN 0904477126. 50, 55
- [94] B. E. A. Saleh and M. C. Teich. *Fundamentals of Photonics*. John Wiley & Sons, New York, 1st edition, 1991. 16, 25, 103
- [95] L. Schares, J. A. Kash, F. E. Doany, C. L. Schow, C. Schuster, D. M. Kuchta, P. K. Pepeljugoski, J. M. Trehwella, C. W. Baks, R. A. John, L. Shan, Y. H. Kwark, R. A. Budd, P. Chiniwalla, F. R. Libsch, J. Rosner, C. K. Tsang, C. S. Patel, J. D. Schaub, R. Dangel, F. Horst, B. J. Offrein, D. Kucharski, D. Guckenberger, S. Hegde, H. Nyikal, C.-K. Lin, A. Tandon, G. R. Trott, M. Nystrom, D. P. Bour, M. R. T. Tan, and D. W. Dolfi. Terabus: Terabit/second-class card-level optical interconnect technologies. *IEEE Journal of Selected Topics in Quantum Electronics*, 12(5):1032–1044, 2006. 4, 6, 43, 47
- [96] K. Schwetlick. *Organikum*. Wiley-VCH, 21. edition, Jan. 2001. ISBN 3527299858. 54
- [97] A. W. Snyder. Coupled-mode theory for optical fibers. *Journal of the Optical Society of America*, 62(11):1267–1277, Nov. 1972. 95
- [98] A. W. Snyder and J. D. Love. *Optical waveguide theory*. Chapman and Hall, London and New York, 1983. 95
- [99] O. Stübbe and G. Mrozynski. Analytic ray-tracing for fast computation of transient transfer functions of pcb level optical interconnects. In *14th Microoptical Conference MOC08*, Brussels, Belgium, Sept 2008. 94
- [100] R. Stine, C. L. Cole, K. M. Ainslie, S. P. Mulvaney, and L. J. Whitman. Formation of primary amines on silicon nitride surfaces: a direct, Plasma-Based pathway to functionalization. *Langmuir*, 23(8):4400–4404, Apr. 2007. 53
- [101] K. Studer, C. Decker, E. Beck, and R. Schwalm. Overcoming oxygen inhibition in uv-curing of acrylate coatings by carbon dioxide inerting. *Progress in Organic Coatings*, 48:92–100, 2003. 53
- [102] N. Takeyasu, T. Tanaka, and S. Kawata. Metal deposition deep into microstructure by electroless plating. *Japanese Journal of Applied Physics*, 44:L1134–L1137, 2005. 50
- [103] Top500. www.top500.org. 2
- [104] H. Tsushima, E. Watanabe, S. Yoshimatsu, S. Okamoto, T. Oka, and K. Imoto. Novel manufacturing process of waveguide using selective photobleaching of polysilane films by uv light irradiation. In *Proceedings of SPIE: Active and Passive Optical Components for WDM Communications III*, volume 5246, pages 119–130, Aug. 2003. 11
- [105] S. Uhlig and M. Robertsson. Limitations to and solutions for optical loss in optical backplanes. *IEEE Journal of Lightwave Technology*, 24(4):1710, Apr. 2006. 6
- [106] J. Van Erps, B. Volckaerts, P. Vynck, C. Debaes, and H. Thienpont. Fabrication of multimode polymer waveguides with integrated micr-mirrors using deep lithography with protons. In *Symposium IEEE/LEOS Benelux Chapter*, pages 87–90, 2004. 6
- [107] G. Van Steenberge. *Parallel Optical Interconnections Integrated on a Printed-Circuit Board*. PhD thesis, Universiteit Gent, 2006. 11
- [108] G. Van Steenberge, P. Geerinck, S. Van Put, J. Van Koetsem, H. Ottevaere, D. Morlion, H. Thienpont, and P. Van Daele. Mt-compatible laser-ablated interconnections for optical printed circuit boards. *IEEE Journal of Lightwave Technology*, 22(9):2083–2089, September 2004. 6, 43
- [109] G. Van Steenberge, N. Hendrickx, P. Geerinck, E. Bosman, S. Van Put, and P. Van Daele. Development of a technology for fabricating low-cost parallel optical interconnects. In H. Thienpont, M. R. Taghizadeh, P. V. Daele, and J. Mohr, editors, *Proceedings of SPIE: Micro-Optics, VCSELs, and Photonic Interconnects II: Fabrication, Packaging, and Integration*, volume 6185, page 618507, 2006. 11
- [110] K. Wada, J. F. Liu, S. Jongthammanurak, D. D. Cannon, D. T. Danielson, D. H. Ahn, M. P. S. Akiyama, D. R. Lim, K. K. Lee, H.-C. Luan, Y. Ishikawa, X. Duan, J. Michel, H. A. Haus, and L. C. Kimerling. Si microphotonics for optical interconnection. In L. Pavesi and G. Guillot, editors, *Optical Interconnects: The Silicon Approach*, volume 119 of *Series in Optical Sciences*, chapter 11, pages 292–310. Springer, 2006. 2
- [111] F. Wang, F. Liu, and A. Adibi. 45 degree polymer micromirror integration for Board-Level Three-

- Dimensional optical interconnects. *Optics Express*, 17(13):10514–10521, June 2009. 44
- [112] J. Weiss. *Nano-meter Scale CMOS Circuits and Packaging for Electro-Optical High Density Interconnects up to 40 Gb/s*. PhD thesis, ETH Zurich, Switzerland, 2008. 6, 11, 88, 110
- [113] J. Weiss, T. Lamprecht, N. Meier, R. Dangel, F. Horst, D. Jubin, R. Beyeler, and B. J. Offrein. Compact electro-optical module with polymer waveguides on a flexible electro-optical substrate for board-level communication. In *Proceedings of SPIE: Optoelectronic Interconnects and Component Integration IX, Photonics West*, volume 7607, page 76070L, Jan. 2010. 84, 85, 88
- [114] L. Xu, J. Liao, L. Huang, N. Gu, H. Zhang, and J. Liu. Pendant thiol groups-attached Pd(II) for initiating metal deposition. *Applied Surface Science*, 211(1-4):184–188, Apr. 2003. 55
- [115] C. Yeh and F. Shimabukuro. *The Essence of Dielectric Waveguides*. Springer, New York, 2008. 24
- [116] T. Yoshimura, M. Miyazaki, Y. Miyamoto, N. Shimoda, A. Hori, and K. Asama. Three-dimensional optical circuits consisting of waveguide films and optical z-connections. *IEEE Journal of Lightwave Technology*, 24(11):4345–4352, 2006. 6